

ABSTRACT

Title of Document: Ionics and Electrochemical Reactions in 1D and 3D Crosslinked Porous Electrodes

Eleanor Idonia Gillette, Doctor of Philosophy, 2015

Directed By: Dr. Sang Bok Lee, Department of Chemistry and Biochemistry

Lithium ion batteries are a critical component enabling many modern technologies, including portable electronics, hybrid electric vehicles and more. While interest in nanomaterials for lithium ion batteries has been growing in recent years, very few systematic studies have been carried out on controlled architectures to explore of the impact of nanoscale and mesoscale structure on the reaction mechanisms, kinetics and resulting rate performance in these electrodes. Here we utilize a combination of anodized aluminum oxide templates and atomic layer deposition to fabricate a variety of systematically variable electrode architectures. The structural control and electrode design are described in detail. Then, analysis of the rate performance, with a focus on distinguishing between diffusion and charge transfer limited reaction mechanisms, is carried out for two distinct electrode systems, focusing on different issues which face advanced electrode architectures. First, we analyze the impact of nanotube length in 1D structures to establish a quantitative understanding of the balance between the loss of capacity due to resistance increases and improvements due to surface area increases. Second, we analyze the impact of transitioning from arrays of 1D nanostructures to crosslinked electrode networks. While 1D alignment is often considered favorable for reducing defects that may lead to capacity loss and degradation, our results indicate that the 3D structures gain more from increased surface area and mass loading than they lose

from the introduction of defects. This observation opens up opportunities for rationally designed advanced electrode architectures to optimize the performance of electrochemical energy storage devices in novel ways that are unavailable to conventional, particle based electrode configurations.

IONICS AND ELECTROCHEMICAL REACTIONS IN 1D AND 3D CROSSLINKED
POROUS ELECTRODES

By:

Eleanor Idonia Gillette

Dissertation submitted to the Faculty of the Graduate School of the
University of Maryland, College Park in partial fulfillment
of the requirements for the degree of
Doctor of Philosophy
2015

Advisory Committee:

Prof. Sang Bok Lee, Chair

Prof. Neil Blough

Prof. Kyu Yong Choi

Prof. John Fourkas

Prof. Janice Reutt-Robey

© Copyright by
Eleanor Idonia Gillette
2015

Acknowledgements

I would first like to acknowledge the support of my adviser, Dr. Lee, who has had such incredible confidence in my abilities and has provided me with the opportunity to work with such an amazing group of students, post-docs and collaborators. I would also like to thank Dr. Rubloff and his group members, without whom none of the atomic layer deposition in this dissertation would have ever been possible. Dr. Rubloff has also served as an unofficial second advisor, and I'm deeply grateful for his advice and support over the years. I'd especially like to thank all the senior students in the Lee group, especially Stefanie Sherrill Wittenburg and Jonathon Duay for helping me learn the ropes of electrochemistry. I would also like to thank the Nanocenter staff for all of their training and assistance with equipment and I especially would like to acknowledge Tom Loughran, John Abrahams and Jon Hummel, for lending their expertise to numerous fabrication and equipment problems and lending their good humor and good nature to many long workdays in the Fablab. For their financial and moral support, I'd like to thank to wonderful women of the ARCS Foundation Metro Washington Chapter, who, with the help of Lockheed Martin, provided generous financial support for the last two years of my work.

I would also like acknowledge the two excellent mentors who inspired and motivated me to become a chemist. First, I'd like to thank Dr. Linda Shimizu, who made the brave decision to take me on as an intern in her research group when I was only in high school. From my time working in her group, I learned to pack a silica gel column and keep a lab notebook, but more importantly, I encountered lively and engaged researchers for the first time and learned that there was so much to discover and learn in

chemistry. Second, I'd like to thank Dr. Jones-Cooper, my high school organic chemistry teacher who helped me turn my summer project into an award winning talk at the SC Junior Academy of Science, and who never allowed me to think that, even as a high school student, that there were topics too difficult to master, with enough time and dedication. Without the support of Dr. Shimizu and Dr. Jones-Cooper, I would probably never have even considered research as a potential pathway. I cannot thank them enough for opening that doorway for me.

Finally, I'd like to thank my family and friends for their support and love over the years. I'd especially like to thank Giovanni Facco, who has been the core of my support network, my sounding board and has kept me well grounded, and well fed!

Contents

List of Figures	vii
List of Tables	ix
Chapter 1: Current Trends in Nano- and Meso-structures for Lithium Ion Batteries.....	1
1.1 Introduction:.....	1
1.2 Metrics and Measurement of Energy Storage.....	1
1.3 Introduction to Lithium Ion Batteries	2
1.4 Cathodes for Lithium Ion Batteries.....	5
1.4.1 General Material Requirements	5
1.4.2 V ₂ O ₅ Electrochemistry.....	6
1.4.3 Fabrication and Structure of Conventional Cathodes	6
1.4.4 Advanced Electrode Architectures	10
1.5 Overview of Dissertation	12
Chapter 2: Fabrication and Characterization of Template-Synthesized Nanomaterials for 1D and 3D Lithium Ion Battery Cathodes	13
2.1 Introduction:.....	13
2.2 Anodized Aluminum Oxide Templates	13
2.2.1 Modified pore shapes.....	16
2.2.2 Barrier layer thinning.....	17
2.2.3 Combined Methods.....	18
2.3 Deposition Strategies	19
2.3.1 Electrodeposition	19
2.3.2 Atomic Layer Deposition.....	20
2.4 Nanomaterial Characterization	22
2.4.1 Electron Microscopy	22
2.2.3 X-ray Powder Diffraction (XRD)	23
2.5 Electrochemical Characterization	23
2.5.1 The electrochemical double layer	23
2.5.2 Ion Intercalation.....	25
2.5.3 Surface redox reactions.....	26
2.6 Methods for Electrochemical Testing.....	27

2.6.1 Cyclic Voltammetry.....	27
2.6.2 Galvanostatic Cycling.....	29
2.7 Conclusions.....	30
Chapter 3: 1D and crosslinked anodized aluminum oxide for controllably modified electrodes	31
3.1 Introduction.....	31
3.2 Methods and Materials.....	32
3.2.1 Anodized Aluminum Oxide.....	32
3.2.2 Electrodeposition of Ni	33
3.2.3 Atomic Layer Deposition.....	33
3.3 Results and Discussion	34
3.3.1 Electrodeposition	34
3.3.2 Atomic Layer Deposition.....	41
3.4 Conclusion	45
Chapter 4: Finite Element Analysis and Nanostructured Electrodes.....	46
4.1 Introduction to Finite Element Analysis Modeling	46
4.2 Methods.....	47
4.3 Results and Discussion	51
4.3.1 Validation.....	52
4.4 Conclusion	60
Chapter 5: Nanotube length and rate performance	61
5.1 Introduction.....	61
5.2 Methods and Materials.....	63
5.3 Results and Discussion	65
5.4 Conclusion:	74
Chapter 6: 3D cross linked vanadium oxide cathodes as a testbed for understanding tortuosity and inhomogeneity.	75
6.1 Introduction.....	75
6.2 Methods and Materials.....	77
6.3 Results and Discussion	78
6.4 Conclusions.....	85

Chapter 7: Summary and Outlook	87
7.1 Summary	87
7.2 Outlook	88
Appendix A: Anodized Aluminum Oxide Methods	89
A-1: General guidelines for fabricating AAO templates:	89
A-2: Common defects and concerns related to homogeneity of the structures	90
A3: The limits of the pore modification structure:	92
Appendix B: Charge Deconvolution Methods.....	93
References.....	97

List of Figures

Figure 1-1: A schematic of a conventional lithium ion battery, in the fully charged state.	3
Figure 2-1: Current profile during pore growth on a clean aluminum sheet, starting from initial conditions (A), non-porous oxide growth (B), pore formation (C) and pore growth and ordering (D).....	14
Figure 2-2: Two step anodization process. First, a porous film is grown (A), etched away (B) and used as a template to begin oxide growth under ordered conditions (C).....	15
Figure 2-3: Schematic of the ALD process.....	20
Figure 2-4: Idealized capacitive response during (a) cyclic voltammetry and (b) galvanostatic voltammetry	25
Figure 3-1: (a) Ni nanowires within AAO template (b) Ni nanowire released from the AAO template (c) Bundle of released Ni nanowires (d) Large area covered with free standing Ni nanowires.....	35
Figure 3-2: SEM images taken from consecutive FIB slices of a two branched AAO template. Each slice is separated by ~2nm of depth.	37
Figure 3-3: HAADF TEM images of FIB thinned AAO templates. (a) the full template with two (b) branched regions and (c) a thinned barrier layer.....	38
Figure 3-4: Nickel deposition into branched AAO pores. (a) SEM image of the nanowires within the branched template (Inset: close up of the branched region) (b) SEM image of free standing wires after AAO removal (c) TEM image of a bundle of branched Ni wires released	39
Figure 3-5: Ru nanotubes released from an AAO template with a single branched region. (a) the full length of the Ru nanotubes (b) a close-up of the branched region	42
Figure 3-6: SEM images of branched templates coated with V ₂ O ₅ (a) three layers of a two-branched template (b) a close up of the branched region (c) region for EDS line scan (d) EDS line scan result	43
Figure 3-7: Cyclic Voltammogram at a scan rate of 0.5 mV/s showing the characteristic peaks corresponding to 1 Li insertion and deinsertion into V ₂ O ₅	44
Figure 4-1: Interpolation function of electrolyte conductivity vs. c/c_{ref}	52
Figure 4-2: Potential as a function of Li fraction, derived from the discharge curve of V ₂ O ₅ MWCNTs discharged at a C/10 rate	53
Figure 4-3: Model predictions and experimental results for the % capacity loss with increasing discharge rate.....	54
Figure 4-4: C/10 discharge curve for 30 nm of V ₂ O ₅ on stainless steel	55
Figure 4-5: Measured and predicted capacity for V ₂ O ₅ nanotube electrodes	56
Figure 4-6: Capacity for different rates for the two experimental systems with different current collector configurations	57
Figure 4-7: Schematic representations of the two current collector configurations, and their corresponding voltage profiles during 25C discharge as calculated by COMSOL..	58
Figure 4-8: Predicted and measured capacity for the conformal current collector case ...	59

Figure 5-1: Schematic of electrode preparation.....	64
Figure 5-2: SEM images of AAO templates grown for (a) 900s (b) 2250s and (c) 3600s. All scale bars are 100nm.....	66
Figure 5-3: Length (left) and mass (right) increase with increasing AAO growth time...	66
Figure 5-4: (a) capacity for four different lengths over increasing scan rates. Capacity as a function of nanotube length at (b) 5 mV/s and (c) 15 mV/s	68
Figure 5-5: Diffusion limited ($v^{1/2}$ dependent) charge calculated by Dunn and Trasatti's methods	70
Figure 5-6: Scan rate dependent charge calculated by Dunn and Trasatti's methods.....	71
Figure 5-7: Measured capacity and calculated capacity for two different rates	72
Figure 5-8: Calculated (a) voltage difference and (b) state of charge difference across the length of a nanotube.....	73
Figure 6-1: (a) 1D arrays of aligned nanowires (b) crosslinked nanowires with interconnections in the plane of the electrode.....	76
Figure 6-2: Electrodes fabricated from 4 different AAO sample structures (a) straight (b) one branch (c) two branch (d) three branch	79
Figure 6-3: Length, measured from SEM images and mass of V_2O_5 , measured by microbalance, for the four different configurations of electrode	80
Figure 6-4: XRD patterns for the four different structures of V_2O_5 AAO electrodes	81
Figure 6-5: CVs from 20mV/s to 2mV/s for (a) straight, (b) three branch electrodes	82
Figure 6-6: Capacity measured by galvanostatic voltammetry for the straight and 3 branched electrodes.....	83
Figure 6-7: Capacity calculated by galvanostatic voltammetry for 500 cycles at a 10 C rate.....	85
Figure A-1: Aluminum holders, front and back and the full cell set-up in a jacket beaker	90
Figure A-2: Top view of (a, c) normal pore structures and (b,d) defect regions after Au sputtering.....	91
Figure A-3: SEM image and current plot from a template modified with 7 branches	92

List of Tables

Table 4-1: Table of symbols used in the COMSOL Multiphysics models of lithium ion batteries.....	48
Table 4-2: Electrolyte parameters.....	51
Table 4-3: Anode parameters.....	51
Table 4-4: Cathode parameters.....	52
Table 6-1: Charge deconvolution for the straight and 3 branched electrodes.....	83

Chapter 1: Current Trends in Nano- and Meso-structures for Lithium Ion Batteries

1.1 Introduction:

Electrochemical energy storage devices are an essential technology needed to help meet the major energy demands of our growing economy for a wide range of applications, from supporting alternative energy sources to improving hybrid electric vehicles and personal electronics. Each of these applications benefits from smaller, lighter and faster devices which can store more energy, especially at higher power. High power is critically important in alternative energy and hybrid electric vehicle applications where energy that cannot be captured quickly will be lost.

1.2 Metrics and Measurement of Energy Storage

Energy and power are the two major parameters on which an energy storage device is evaluated. Energy, which is broadly defined in chemistry and physics as the ability to do work, is measured in joules, or watthours. For a battery, the energy is defined as the charge (q) times the voltage window (ΔV) of the battery (Eq. 1-1).

$$E = q\Delta V \quad \text{Eq 1-1}$$

The total charge that can be stored in a device is determined by the charge capacity of the anode and cathode materials, while the voltage window is determined by the difference in the potential between the anode and cathode materials. These two parameters generally determine the choice of electrode material for any given battery system.¹

Power is related to how quickly energy can be moved in and out of a storage device, and is directly related to the current density, as well as the voltage window (Eq. 1-2).

$$P = i\Delta V \quad \text{Eq. 1-2}$$

Again, the critical importance of voltage window to cell performance can be observed, but power is largely governed by the cell current. Reaction kinetics and ionic and electronic conductivity determine the maximum current which can be drawn from a cell.²

Lithium ion batteries stand out among other energy storage strategies for their generally good power and energy densities.³ As a result, they have been the focus of a wide variety of research, for applications as large as grid scale storage⁴ and as small as microbatteries for medical devices⁵ and ultra-thin, flexible batteries for wearable technology.⁶ While every application range has different power and energy requirements, essentially all next-generation technology can benefit from smaller, lighter batteries with higher power, higher energy and longer cycle lifetimes. In order to explore options for improving this technology, first it is important to understand the chemical reactions which facilitate the current Li ion technology.

1.3 Introduction to Lithium Ion Batteries

While batteries such as the lead acid and alkaline cells have been familiar to most consumers since at least the 1940s, lithium ion batteries have completely transformed the energy landscape in the few decades since they arrived on the market in 1991.⁷ As of April 2015, lithium ion batteries comprised nearly half of all secondary (rechargeable) battery sales in Japan.⁸ The basic structure of a lithium ion battery is illustrated schematically in Figure 1-1.

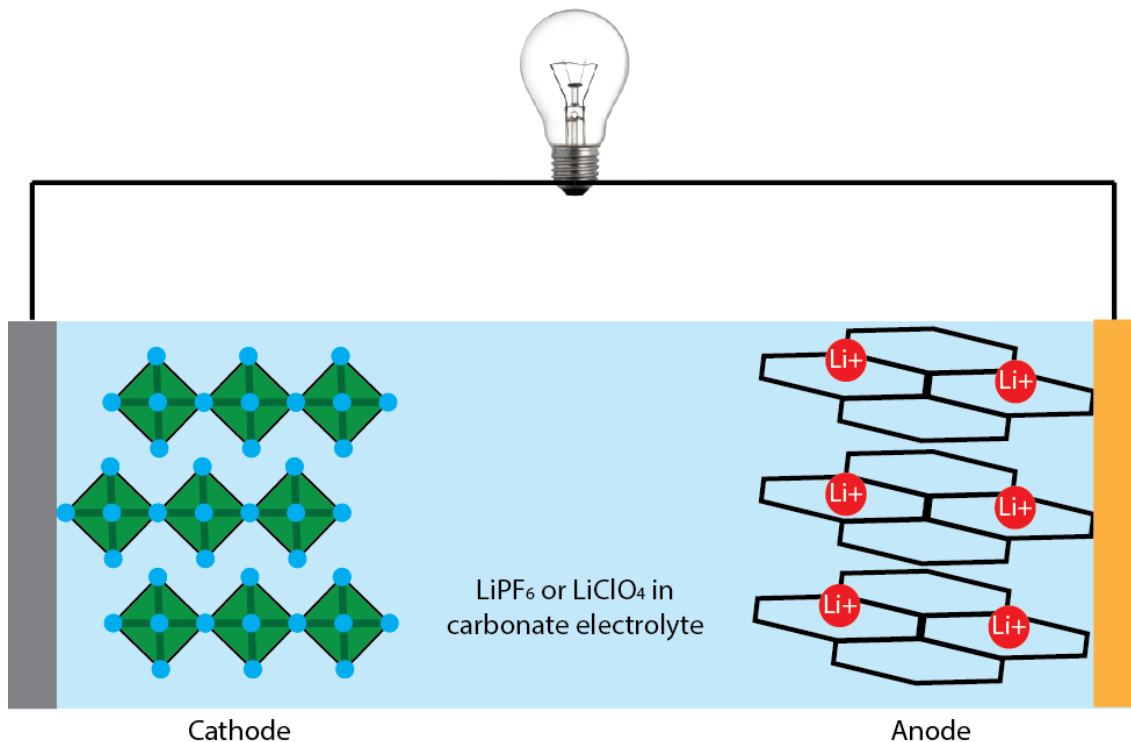


Figure 1-1: A schematic of a conventional lithium ion battery, in the fully charged state

During discharging, electrons flow from the anode to the cathode, through the external circuit, while lithium ions are removed from the anode and inserted into the cathode. These lithiation and delithiation reactions are accompanied by a reduction and oxidation reaction, respectively. The discharge process can continue until all lithium has been removed from the anode and inserted into the cathode. To recharge the battery, external current must be applied to provide the energy needed for the reverse reactions to take place. During charge the cathode will be delithiated, an oxidative reaction, and the anode will be reduced by the insertion of lithium. In an ideal system, the same quantity of lithium, and the same number of electrons will be used for charging as were produced during discharging, but of course some energy will always be lost. Reactions are described as being reversible when the charge difference between the oxidation and

reduction processes is relatively small. On the device scale, reversibility can be described as Coulomb efficiency, which is simply the ratio of charge passed by the cell during charging and discharging. Good full cell batteries should have Coulomb efficiencies approaching 99 %.

There are three critical components to any electrochemical cell; cathode, anode and electrolyte. In a lithium ion battery, charge is stored by the intercalation of lithium ions into the layers of either the carbon anode or a metal oxide cathode. This insertion of lithium is accompanied by a reduction reaction, while the de-insertion of lithium accompanies an oxidation, following the general half reactions below:



Commercial lithium ion batteries typically feature graphite anodes, which have a theoretical capacity of 372 mAh/g, and a low potential ($\sim 0.1\text{V}$ vs. Li/Li^+).⁹ While metallic lithium can theoretically provide a slightly larger voltage window and a much better gravimetric capacity, safety and reversibility issues prevent it from being used in rechargeable battery systems.¹⁰ Graphite also can have reversibility issues, generally resulting from the reduction of electrolyte on the graphite surface. This process consumes electrons and electrolyte molecules irreversibly, and coats the anode with a layer of so-called “solid-electrolyte interphase” (SEI). Transport through the SEI can be a kinetic bottleneck in some battery systems which limits rate performance.¹¹

In light of these issues at the anode surface, electrolyte choice is critical for battery performance. Organic electrolytes are typical, with ethylene carbonate, propylene carbonate and related structures being the most common.^{11,12} Ionic liquids, polymers and solid state electrolytes have all seen growing interest in the field, particularly focused on expanding the voltage window and eliminating flammable components.^{13,14}

While many open questions remain in the areas of anode and electrolyte performance, this dissertation will focus on cathode materials and their challenges. Conventional carbonate electrolytes and lithium anodes will be most commonly used in our studies, to allow us to focus on the reaction kinetics and structure of the cathode specifically. The chemistry and development of cathodes for lithium ion batteries will be discussed in more detail in the following section.

1.4 Cathodes for Lithium Ion Batteries

1.4.1 General Material Requirements

There are a wide variety of cathode materials which are suitable for lithium intercalation, which includes sulfides, oxides and phosphates. One of the first Li insertion materials which was extensively studied was layered TiS_2 , which was observed to have good reversibility for Li insertion, but which has a relatively low voltage, $\sim 2.5\text{V}$ vs. Li.¹⁵ Layered oxides were a logical choice for further investigation, and LiCoO_2 was reported soon after, with a much higher voltage and a higher Li-ion diffusivity than TiS_2 exhibited.^{16,17} LiCoO_2 is the cathode which was first commercialized in a rechargeable lithium ion battery, by Sony in 1991. However, it is expensive, and plagued by safety issues, and so LiMnO_2 and LiFePO_4 are gaining wider commercial adoption.¹⁸ A variety of other materials may also be appropriate and are the subject of continued research.

Layered oxides, like MoO_3 and V_2O_5 , have attracted attention particularly for their fast reaction kinetics, which may potentially lead to higher power battery systems. The pursuit of higher power systems is one major focus of current battery research, and the goal that we will focus on here.

1.4.2 V_2O_5 Electrochemistry

Reversible Li insertion into vanadium (V) oxide was reported as early as 1976.¹⁹ V_2O_5 has continued to be an appealing cathode because of its good capacity, good Li insertion kinetics, and it is safer, more abundant and less expensive than cobalt oxide.²⁰

The layered structure, $\alpha\text{-V}_2\text{O}_5$, undergoes two structural transitions during the insertion of 1 Li^+ into the lattice, first transitioning to $\epsilon\text{-Li}_x\text{V}_2\text{O}_5$, where $0.38 < x < 0.7$, where Li insertion takes place primarily between the layers of V_2O_5 , resulting in very little structural distortion from the bulk oxide.²¹ The remaining Li insertion $0.7 < x < 1.0$ involves a conversion to $\delta\text{-Li}_x\text{V}_2\text{O}_5$, which involves nearly doubling the c-parameter (the spacing between layers), but very little other structural distortion.²² The two transitions give rise to two distinct peaks in cyclic voltammetry or two distinct plateaus in galvanostatic voltammetry, approximately 3.4 and 3.2V vs Li/Li^+ , respectively. Because the insertion of 1 mol $\text{Li}/\text{V}_2\text{O}_5$ involves insertion completely between the layers of the oxide, the kinetics of both transformations is fairly fast and reversible, making V_2O_5 a good performing and useful model cathode material.

1.4.3 Fabrication and Structure of Conventional Cathodes

For any given cathode material, the structure and fabrication of the complete electrode may have dramatic influence on the material performance. Current conventional battery cathodes are typically composed of large ($>10\mu\text{m}$) particles of the

metal oxide active material, held together by polymer binders and mixed with activated carbon to provide improved electronic conductivity. Considerable attention has been given to understanding and describing these porous composites as a function of particle size, shape, additive ratios, etc. While higher mass loading is required for better energy density, void space is required for electrolyte infiltration, and a combination of conductive pathways provided by the carbon additives and the ion pathways provided by the void spaces will determine the maximum power an electrode can achieve. As a result, characterization of these structures is a critical part of conventional electrode design. Two primary metrics are used to describe these conventional porous electrodes, porosity and tortuosity.

Porosity (ϵ) is defined as the fraction of the total composite volume occupied by void space. For an electrochemical system, that void volume is critical space which must be infiltrated by electrolyte for any charge storage reaction to be carried out. However, obviously, increased void space is directly related to decreased active material loading for a given volume, leading generally to lower volumetric energy densities in high porosity electrodes.²³ Balancing the loading of active mass with electronic and ionic conductivity is critical for achieving the best possible combination of energy and power density.

Tortuosity (τ) can be more difficult to define, but most simply is the ratio of length of the diffusion path of an ion to the thickness of the electrode.²⁴ High tortuosity systems, where ions must travel long distances through convoluted pathways, result in higher solution resistance and slower ion diffusion, leading to sluggish rate performance. Reducing tortuosity within a porous electrode is generally considered a good strategy for improving the power performance.²⁵ However, defining and measuring tortuosity remains

one of the major challenges in the characterization of porous electrodes.^{26,27} The traditional Bruggeman equation (Eq. 1-3) which relates tortuosity(τ) to porosity(ϵ) is broadly used, but often incorrectly applied. The choice of Bruggeman coefficient (α), which differs for various geometries, determines the accuracy of the prediction.

$$\tau = \epsilon^{-\alpha} \quad \text{Eq 1-3}$$

This relationship holds well for regular, simple geometries, such as monodisperse packed spheres. However, inhomogeneity as simple as variation in the sphere size can introduce errors up to 15% in the estimate provided by the Bruggeman equation.²⁸ Additionally, the assumption made in most battery papers, that $\alpha=1.5$, has been demonstrated to be incorrect, even for standard electrode materials.²⁶ Empirical fitting can be used to determine alpha for more complex geometries, but the concept generally defines only isotropic systems which have homogenous porosity and tortuosity.²³ Direct computational simulations of complex geometries has revealed that tortuosity can vary widely even within different cross-sections of the same electrode. Measurements of commercial graphite electrodes measured up to 30% differences in the tortuosity calculated for different sections of the same electrode, and for that case the Bruggeman equation had almost no predictive value.²⁹ As electrode structures become more complex, it becomes difficult to effectively quantify tortuosity in a way which allows meaningful comparison of different electrodes.

There have been recent improvements in simulation strategies for quantifying tortuosity. A recent, open source software, has been released to estimate the Bruggeman coefficient (α) from SEM images tortuosity directly from geometric reconstructions of

electrodes rather than using traditional numerical methods like random walk simulations, which require full 3D characterization of a structure.³⁰ These efforts have provided some important observations for particle based systems which can inform the design of next generation electrodes.

First, it has been consistently observed that the uniformity in particle size distribution improves performance and reduces inhomogeneity which leads to degradation.³¹ However, the use of polymer binders and conductive additives prevents idealized structures from being created even with excellent, monodisperse active material particles.²³ Additionally, advanced modeling methods have been employed to investigate the potential for anisotropy in tortuosity. In particular, through 3D tomography and numerical modeling Wood *et Al* observed that in-plane (parallel to the current collector) tortuosity is generally lower than out-of-plane tortuosity.²³ Electrochemistry is generally expected to be most sensitive to out-of-plane tortuosity, potentially offering an opportunity for rationally designed electrodes to reverse this observed trend. Increasing in-plane tortuosity should allow an increase in mass loading (a decrease in porosity), but maintaining low out-of-plane tortuosity should limit the kinetic penalty. However, this hypothesis may not address the issues of degradation. Irregularities in the shape and size of particles and void spaces can lead to inhomogeneous charging and discharging behavior, which can result in local overcharging, over-heating or electrolyte consumption, all of which lead to irreversible charge consumption and can present safety issues related to flammability or gas generation.³² Degradation and rate performance are the two major performance metrics which advanced architectures can aim to improve.

1.4.4 Advanced Electrode Architectures

Nanostructures have been widely investigated for their higher surface areas and shorter ion diffusion lengths, which should provide improved power and energy density. However, many examples of nanostructured cathode materials are composed similarly to commercial batteries, with polymer binder and carbon additives, which fails to eliminate some of the problems related to tortuosity and porosity at the electrode scale. There has been increasing interest in fully nanostructured electrodes which can eliminate the use of binder and additives. 1D and 3D arrays of nanotubes or nanorods are a particularly appealing strategy, as these arrays can provide direct electrical contact to the current collector and high surface area interaction with electrolyte.³³ This strategy opens up a variety of options for structural control on both the single nanowire and the aggregate electrode scale. On the individual structural scale, core-shell or other composite nanowires have been widely investigated for improving on single material arrays.³⁴ However, on the electrode scale, the interaction between adjacent structures is also important, but current research has mainly focused on the stability of the structures.³⁵ This connection between individual nanostructures and macroscale composites is referred to as the mesoscale, and mesoscale architecture is a critical area of research if porous electrodes fabricated from arrays of nanotubes or nanowires are going to replace particle based structures in real energy storage devices.³⁶

One advantage of arrays or composites of 1D nanostructures is that they do not necessarily conform to the Bruggeman relationship, particularly where the individual structures have some order on the mesoscale.

In particular, a few different strategies have been demonstrated for fully nanostructured, high performance batteries with novel electrode architectures. One, demonstrated by the Braun group, features a regular, 3D porous Ni scaffold created using polystyrene beads as a template. The Ni acts as the current collector, on which active Li storage materials can be deposited.³⁷ The performance of full batteries fabricated with this structure is quite remarkable, retaining 25% of their 1C capacity at 1000C, a remarkable current density for any battery.³⁸ These batteries have very regular porous structures, and are still limited in their energy density directly by mass loading, as increased material deposition will eventually close electrolyte spaces and severely limit performance.

An alternative strategy has been proposed by our group in collaboration with the Rubloff group. We have demonstrated a variety of high aspect ratio nanotube and nanorod energy storage electrodes which can achieve remarkable power density.^{39,40} Moving towards full cells, we have demonstrated both a pseudocapacitor and a battery with a fully nanostructured anode and cathode.^{41,42} In particular, the battery demonstrated by Liu *et Al.* facilitates high power performance by utilizing a conformal ruthenium current collector underneath 6 μ m long V₂O₅ nanotubes. The structure directing agent in this device is anodized aluminum oxide, which provides perfect alignment for the anode and cathode, with a tortuosity of 1. The focus of this structure was demonstrating the value of the conformal current collector for achieving the best possible rate performance, but no other structural parameters were modulated. These results will be discussed in greater detail in Chapter 4.

Understanding and quantifying the potential impact of the various components of advanced architectures on electrochemical reactions, rate performance and degradation is a critical step towards rationally designed, high performance, nanostructured lithium ion batteries. In particular, systematic studies are needed to separate the impact of different aspects of electrode structure on electrochemical performance. Here in particular we will focus on two systems; vertically aligned nanotube arrays and nanotube arrays with three dimensional ion pathways introduced into the structure using a networked porous structure. These two test-bed structures will be used to investigate the impact of electronic conductivity in these high aspect ratio structures, as well as the effect of increased surface areas, mass loading, tortuosity, and defects in the crosslinked structures.

1.5 Overview of Dissertation

- Chapter 2 will introduce the methods and materials that will be used control, characterize and model mesostructured energy storage devices
- Chapter 3 will present designs for testbed electrodes to systematically examine the impact of aspect ratio, tortuosity and defects in our model V_2O_5 cathode system.
- Chapter 4 will present two extreme examples of electronic conductivity in the aligned nanotube array electrodes, and introduce a mathematical modeling protocol to assist in interpreting structural results.
- Chapters 5 and 6 will present results related to aspect ratio and tortuosity using these testbed devices

Chapter 2: Fabrication and Characterization of Template-Synthesized Nanomaterials for 1D and 3D Lithium Ion Battery Cathodes

2.1 Introduction:

Energy storage research has turned to nanostructured electrodes in pursuit of higher surface areas and shorter ion diffusion pathways, which are expected to improve the power and energy density of conventional materials. A wide variety of strategies are employed to synthesize nanostructures of metals, metal oxides and polymers for various energy storage applications. The template synthesis of nanomaterials is a common way to produce materials with similar size and shape distribution, and has been widely used to fabricate nanomaterials for lithium ion batteries.⁴³ Two types of template are generally used, soft templates or hard templates. Soft templates generally rely on surfactant molecules to provide structural direction, producing 0D nanoparticles⁴⁴, 1D tubes⁴⁵ or wires, and a variety of more complex porous networks⁴⁶, which mimic the shape of micelle structures formed by the surfactant in the solvent. Hard templates rely on solid structures to direct the shape of the nanomaterials, such as anodized aluminum oxide⁴⁷, zeolites⁴⁸ or mesoporous silica⁴⁹. In this work, anodized aluminum oxide hard templates are used to create high aspect ratio arrays of regular and modified nanotube and nanowire structures.

2.2 Anodized Aluminum Oxide Templates

Porous anodized aluminum oxide (AAO) membranes have been of interest to chemists and physicists since the 1970s.⁵⁰ AAO has been used widely as a template for producing nanomaterials, as well as for various filtration and optical applications.⁵¹⁻⁵³ The synthesis of AAO is relatively simple; a voltage is applied to a sheet of aluminum in

an acidic electrolyte (Figure 2-1A). Initially, a solid oxide layer will be formed on the

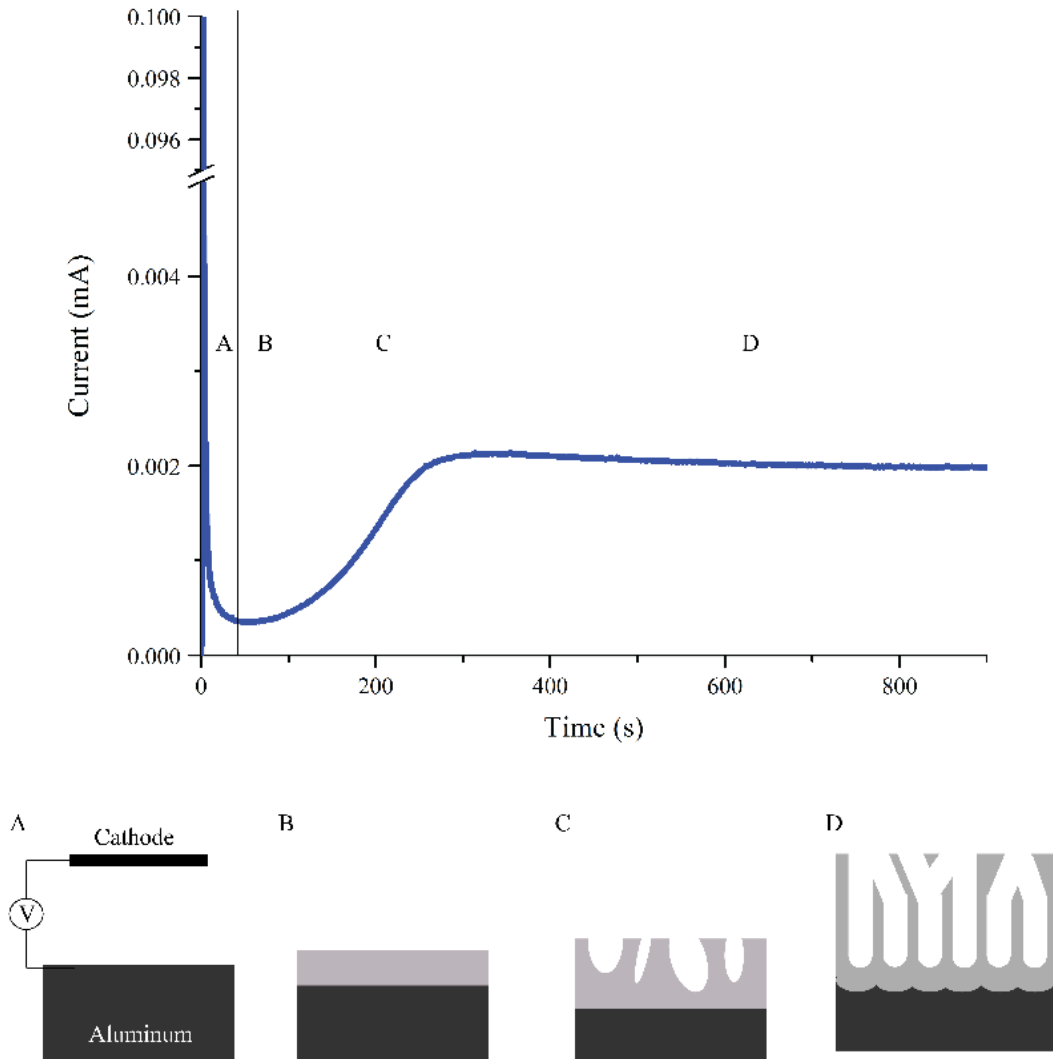


Figure 2-1 Current profile during pore growth on a clean aluminum sheet, starting from initial conditions (A), non-porous oxide growth (B), pore formation (C) and pore growth and ordering (D)

aluminum surface (Figure 2-1B), but defects on the surface will lead to localized areas of high electric field concentration. The high electric field facilitates field-assisted dissolution of oxide into the acidic electrolyte, forming pores, while the oxide continues to grow (Figure 2-1C). The expansion of the oxide at the aluminum/oxide interface forces

oxide to flow away from the interface. If adjacent pores are close to one another, this plastic flow is directed normal to the surface by the forces exerted by the expansion of the oxide around the neighboring pores. However, if the pores are farther apart than this critical equilibrium distance, they can grow in any direction, and will form branches or other voids as space allows.⁵⁴ Eventually, a steady state is reached where oxide dissolution and oxide growth are steady, leading to the growth of regular pores (Figure 2-1D).^{55,56}

In the late 1990s, Masuda and co-workers developed a method of 2-step anodization which took advantage of this process for the production of regular hexagonal arrays with tunable pore sizes, without the disordered, branched region at the top of the template.⁵⁷ The 2-step process flow and the resulting ordered cell structure are shown in Figure 2-2.

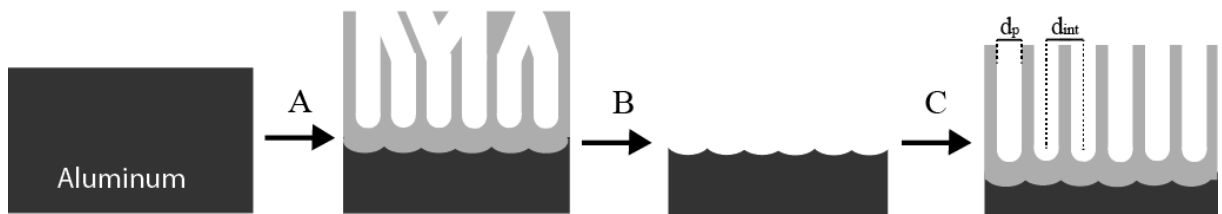


Figure 2-2: Two step anodization process. First, a porous film is grown (A), etched away (B) and used as a template to begin oxide growth under ordered conditions (C).

The two step anodization process allows regular, ordered porous films to be grown without a disordered, branched region at the top. A first anodization is carried out as described previously, but then the entire aluminum oxide is etched away, leaving a dimpled aluminum surface to direct the formation of the pores in their equilibrium positions at the start of the second anodization process.

Specific voltage and electrolyte combinations for which oxide growth and oxide dissolution rates favor pore ordered were identified to produce well ordered, regular hexagonal pore structures over a wide range of pore sizes.⁵⁸⁻⁶⁰ Interpore spacing can be predicted simply from the anodization voltage, using Eq 2-1:

$$d_{int} = -1.7 + 2.81U_A \quad \text{Eq 2-1}$$

This relationship remains linear up to nearly 500nm interpore distance, although different electrolytes are needed for anodization in different regimes of this ordered growth.^{60,61} Along with interpore spacing, the voltage determines the pore diameter, and the porosity is generally 10% of the total volume of the AAO film formed.⁶² Pore diameters can be increased by etching, but are limited by the upper boundary of the interpore spacing. Anodization voltage is also the primary determinant of the barrier layer thickness. A linear relationship between voltage and barrier layer thickness is consistently observed.⁶³

As interest in nanomaterials has expanded from simple 1D arrays towards more complex 3D structures, there has been a variety of work investigating more complex three dimensional structures that result from manipulating the rates of growth and dissolution of the oxide. Two major focuses of AAO modification have been the modulation of pore shape and thinning of the barrier layer.

2.2.1 Modified pore shapes

In 1999, Xu and coworkers⁶⁴ produced the first controllably branched AAO membrane, demonstrating that a potential drop during anodization could result in a y-shaped, bifurcated pore. Elaboration on voltage modulation during anodization has

resulted in a variety of techniques which can produce branched,⁶⁵ perforated,⁶⁶ and otherwise modified⁶⁷ pore structures that can be used for template synthesis of various 3D materials.³⁵

However, only a few methods allow for controllable branching in sections of the pores while maintaining straight, hexagonally arrayed regular structures throughout the rest of the alumina membrane. The most common of these methods is known as pulse anodization,⁶⁸ a combination of the so-called “mild anodization” techniques discovered by Masuda and others, and much faster, higher voltage techniques known as hard anodization, developed originally by Lee *et al.*⁶⁹

One major drawback to this strategy, however, is that it typically results in a thickened barrier layer that must be removed by selective etching after removal of the native aluminum. This phenomenon is a result of the competitive mechanisms of oxide formation, viscous flow, and dissolution which produce the ordered AAO geometry. It has been noted recently that at higher current density, viscous flow of the oxide is the dominant pore formation mechanism, while oxide dissolution is prevalent at lower current densities.⁷⁰⁻⁷² As a result, lower voltage methods with corresponding lower currents should produce films with thinner barrier layers. This prediction is supported by older empirical observations that the barrier layer thickness scales linearly to the anodization voltage⁵⁰.

2.2.2 Barrier layer thinning

The thickness of the barrier layer in particular is a concern, as it limits the usefulness of the aluminum on which AAO is grown, despite aluminum's well established application as a current collector in devices like lithium ion batteries.

Typically, the aluminum oxide membranes are removed from the native aluminum and the barrier layer is then removed with a wet etching process. Then, a new current collector is deposited using a vacuum deposition method like sputtering or thermal evaporation. However, this approach requires films to be quite thick, typically more than 20 μm , in order to avoid shattering during these processing steps. For thinner membranes, and for more efficient processing, the native aluminum itself would seem to be a promising current collector, but this approach requires modification of the normal AAO structure. A few techniques have been demonstrated for removing the barrier layer at the bottom of AAO pores in order to facilitate electrodeposition directly onto the Al.⁷³⁻⁷⁵ These techniques have not seen broad application, and until our recent demonstration, had never been combined with other AAO pore modification strategies.

2.2.3 Combined Methods

Stephanie Sherrill's dissertation work in our group demonstrated a combination of barrier layer thinning and 3-D structuring.⁷⁶ This work has been continued to demonstrate metal deposition directly on the aluminum substrate, using both 1D arrays as well as in more complex, interconnected pore networks.⁷⁷ These processes rely on the ordered and disordered growth regimes of AAO, and require no lithographic patterning or other defect introductions to achieve the desired structures. As a result, these techniques can be combined easily during the course of an anodization to produce a variety of different geometries without requiring any additional equipment, and utilizing relatively few additional processing steps.

In this dissertation, this branching and merging procedure is used extensively to explore the implications of porosity and disorder in vanadium oxide cathodes for lithium ion batteries.

2.3 Deposition Strategies

Filling templates with active material for battery or supercapacitor electrodes can be achieved by a variety of methods, including sol-gel⁷⁸, hydrothermal⁷⁹, electroless⁸⁰, electrochemical⁸¹, chemical vapor⁸² and atomic layer deposition⁸³. Electrodeposition and atomic layer deposition are the two used most frequently in our group, and were the two methods chosen to demonstrate 1D and 3D nanomaterial fabrication in our novel, modified AAO structures.

2.3.1 Electrodeposition

Traditionally, electrodeposition has been carried out in free-standing aluminum oxide membranes, with the barrier layers chemically etched away and a current collector added by sputtering or thermal evaporation. This process has been used widely to create nanowires and nanotubes of metals⁸⁴, metal oxides^{85,86} and conductive polymers.

Deposition may take place either under constant current, constant voltage, or with a variety of cycling, pulsing or alternating current or voltage schemes. The pulse or AC deposition schemes are often used for deposition into high aspect ratio structures, to prevent diffusion limitations for altering the structure of the resulting deposit.

There are a few examples in the literature of electrodeposition directly onto the native aluminum underlying AAO pores with deliberately thinned barrier layers.^{73–}

⁷⁵. Our demonstration of electrodeposition directly onto aluminum into modified 3D AAO networks, the first of its kind, will be discussed in more detail in Ch. 3.

2.3.2 Atomic Layer Deposition

Atomic layer deposition is a popular technique for depositing metals and metal oxides with precise control of the thickness and composition of the material.⁸⁷ The process is surface limited and requires gas-phase precursors in a carefully controlled vacuum system. The general process flow is seen in Figure 2-3, and follows the following steps 1. Precursor saturation 2. Purge 3. Oxidation 4. Purge. This process is repeated as necessary to achieve the desired thickness.

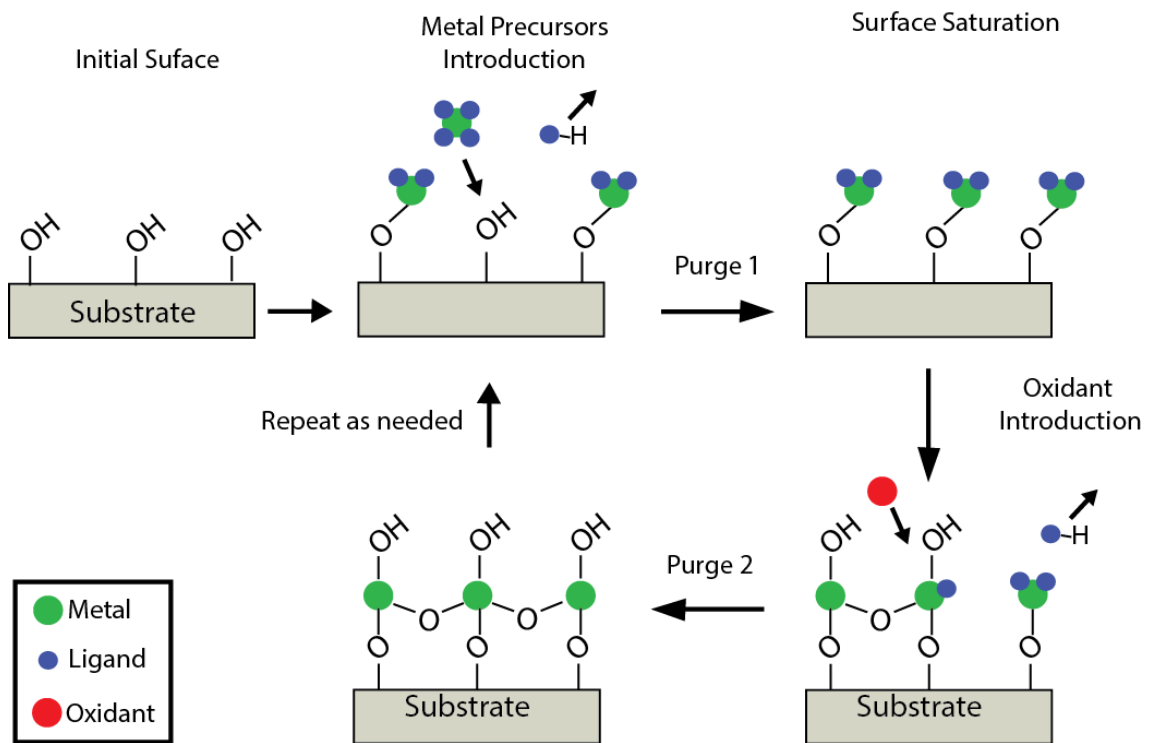


Figure 2-3: Schematic of the ALD process

Atomic layer deposition (ALD) has been demonstrated previously for coating various substrates for use as batteries⁸⁸, pseudocapacitors⁸⁹ or electrostatic capacitors³⁹.

However, while conformal coatings are one of the advantages of ALD, care must be taken to characterize deposition onto new substrates to identify any changes to the growth and conformality of the films⁹⁰, particularly on high-aspect-ratio structures.

Substrate dependent ALD growth limitations may be present if there are serious barriers to nucleation on a substrate surface. This phenomenon has led to a variety of challenges depositing good ALD films onto CNTs, graphene and other sp^2 hybridized structures. Some form of functionalization is generally required, which often lowers the conductivity of the carbon, limiting its usefulness as an electrode scaffold.⁹¹ While there are variety of strategies to avoid these issues, overall, choosing to deposit on surfaces with hydroxyl groups is most likely to be effective for forming uniform ALD coatings. Fortunately, aluminum oxide is an excellent surface for ALD deposition, and has been widely used as a substrate for deposition.⁹²

However, high-aspect-ratio anodized aluminum oxide can be a challenging substrate because the high surface area and longer diffusion pathways lead to poor coverage of the substrate surface. This phenomenon was first observed in AAO pores coated with Al_2O_3 . ALD reactant pulses were extended from 1s on planar substrates to nearly 30 s to achieve conformal coatings on AAO templates with pore diameters of ~65 nm and pore lengths of ~50 μm .⁹² In the same study, ZnO ALD deposition into AAO was observed for varying pulse times. The ZnO coverage into the pore correlated with the square root of the pulse time, a relationship that is indicative of a diffusion limited process. However, ALD of SiO_2 did not have the same correlation, highlighting the limitations of generalizing behavior from one substrate, structure, or ALD chemistry. For any new ALD process and substrate combination, care must be taken to ensure that the

process is working as expected and to characterize the limitations of the conformality of the coating.

2.4 Nanomaterial Characterization

In order to develop new understanding of the relationship between material, structure and electrochemical performance, a variety of characterization techniques must come into play. The techniques can be generally separated into physical techniques, which characterize the structure and composition of the materials and electrochemical techniques, which focus on the electrochemical reactions that take place within the electrodes.

2.4.1 Electron Microscopy

Scanning electron microscopy (SEM) is the primary tool for characterization of AAO templates and electrodes fabricated from them. An electron beam is used to scan the surface of a material, and the scattered electrons are collected to provide imaging with resolution as fine as 1 nm. Secondary electrons, or inelastically scattered electrons, are the most commonly used for imaging, although other modes are available.⁹³

Transmission electron microscopy (TEM) functions by sending an electron beam through a thin sample, providing much higher resolution images that probe the whole structure. However, for three dimensional structures, TEM is a limited technique, as samples need to be less than 100nm thick for detectable electron beam transmission through the sample.⁹⁴

Within either SEM or TEM, chemical composition can be determined using energy dispersive X-Ray spectroscopy (EDS). X-rays produced during electron exposure can be collected and analyzed to provide elemental composition of the sample. In SEM,

these X-rays may be produced as far as a micron into the sample, and so EDS should not be considered a highly surface-sensitive technique.⁹⁴

2.2.3 X-ray Powder Diffraction (XRD)

XRD is a powerful, rapid characterization technique for crystalline materials.

When a beam of collimated X-rays interacts with a crystalline sample, the X-rays will be diffracted by the crystal planes. This diffraction can be described as a relationship between the X-ray wavelength (λ) and the spacing between atomic planes (d) and the diffraction angle (θ). This relationship is known as Bragg's law, shown in Eq. 2-2.

$$\lambda = 2d \sin \theta \quad \text{Eq. 2-2}$$

Based on the diffraction over a range of 2θ , peaks will be observed at characteristic positions for a given crystalline material, and can be indexed to standard materials for identification.⁹⁵

2.5 Electrochemical Characterization

In order to measure electrochemical processes taking place within cathode materials, it is critical to understand the different types of charge storage, and how they can be measured. Three different charge storage mechanisms and three different measurement techniques are described here, along with analysis methods that allow mathematical deconvolution of critical kinetic data from these tests.

2.5.1 The electrochemical double layer

The simplest way to store charge in an electrochemical device is in the electrochemical double layer (EDL). In fact, since the EDL is a phenomenon present at any charged surface immersed in electrolyte, all electrochemical devices have some component of capacitance that can be attributed to the EDL. This capacitance is analogous to a parallel

plate capacitor, and the charge stored can be characterized similarly, using Equation 2-3.

96

$$C = \frac{\epsilon_0 \epsilon_r A}{l} \quad \text{Eq. 2-3}$$

Relative permittivity and l (distance between ion/wall) are determined purely by electrolyte choice, so surface area (A) is the critical parameter for increasing the charged stored in the EDL. Therefore, high surface area carbons are a popular and promising choices for devices known as electrochemical double layer capacitors, which store charge relying on the EDL alone.⁹⁷⁻¹⁰² These devices can achieve high power, because there are no reaction kinetics to impede charge storage. However, their energy density is limited to the charge of the material surface, which is generally quite small, and so often the double layer capacitance contribution to charge storage can be neglected in other storage devices. However, for nanostructures with high surface areas, the double layer capacitance may still be a significant contribution. Importantly, capacitance scales linearly to voltage, so during the charging or discharging of a battery, its contribution to the charge stored in any electrochemical energy device is regular and predictable. The charged stored by double layer capacitance at an electrode surface can be treated like a background signal, with constant current response during cyclic voltammetry (Figure 2-4a) and a linear potential contribution during galvanostatic charging (Figure 2-4b).

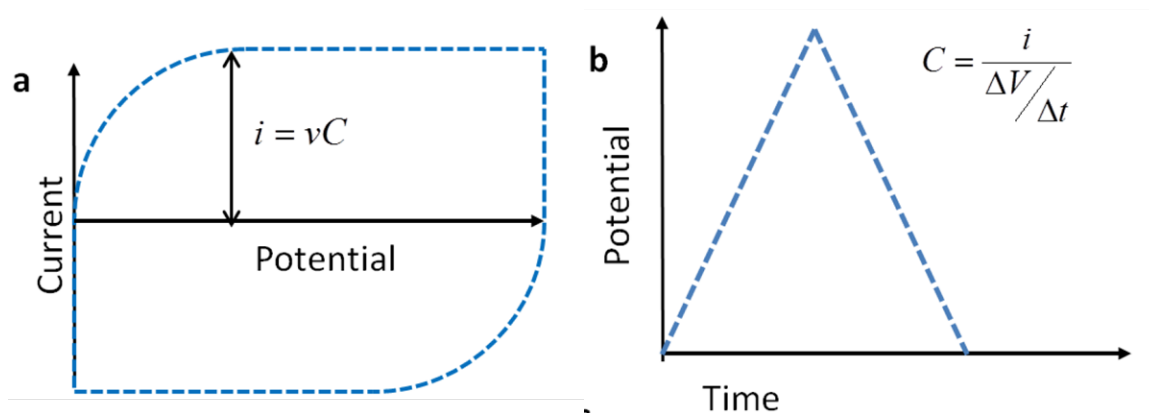


Figure 2-4: Idealized capacitive response during (a) cyclic voltammetry and (b) galvanostatic voltammetry

2.5.2 Ion Intercalation

Lithium ion batteries have changed the energy storage landscape, facilitating the mobile device revolution by providing high energy density with relatively low weight and volume.¹ Charge storage in a lithium ion battery relies on a process called intercalation, in which Li^+ ions are inserted into the crystal lattice of an electrode, coupled to a reduction of the electrode material. This reaction is known as Faradaic, because it involves the transfer of at least one electron. Because of the electron transfer process, this mechanism can store more charge than EDLCs, but the kinetics of the reaction limit the power of batteries. Slow reaction kinetics, hindered diffusion of Li ions through a porous electrode and slow diffusion of the intercalated lithium through the solid electrode are all potential kinetic bottlenecks in this process. Like any other redox reaction, lithium insertion is governed by the Nernst Equation (Eq. 2-4), in which E is the voltage at which a reduction reaction will be expected to take place for a given half-cell:

$$E = E^0 + \frac{RT}{zF} \ln\left(\frac{a_{ox}}{a_{red}}\right) \quad \text{Eq 2-4}$$

E^0 is the standard reduction potential, R is the universal gas constant, T is temperature, z is the number of moles of electrons transferred in the reaction step, F is Faraday constant and a_{ox} and a_{red} are the chemical activities of the oxidized and reduced species, respectively. In dilute solutions, these activities can often be replaced by concentrations, while in solid state reactions like Li insertion, they may need to be considered in more detail.

The kinetics of lithium insertion can be described by the Butler-Volmer equation (Eq. 2-5), which describes the current density for a given reaction.

$$j = j_0 \left(\exp \left[\frac{\alpha z F \eta}{RT} \right] - \exp \left[\frac{-(1-\alpha) z F \eta}{RT} \right] \right) \quad \text{Eq. 2-5}$$

j_0 is the exchange current density, α is the charge transfer coefficient and η is the overpotential, the difference between the electrode voltage and the reduction potential, as determined by the Nernst equation. The current response to electrochemical testing will be quite different from the capacitive case as a result of the current dependence on overpotential. In cyclic voltammetry, current peaks centered around E are indicative of Faradaic reactions. During galvanostatic voltammetry, voltage plateaus will be observed near E .

2.5.3 Surface redox reactions

A third type of electrochemical storage mechanism has been identified in the literature as “pseudocapacitance”. Strongly surface area dependent, but with higher charge storage than EDLCs, this mechanism is generally attributed to fast Faradaic reactions at the surface or near-surface of metal oxide electrodes. This mechanism has been widely studied as a way to achieve the higher power and cycle life characteristic of

EDLCs with higher energy density contributed by the Faradaic reaction. While it should be governed by the Nernst and Butler-Volmer equations, the kinetics of pseudocapacitance are often quite fast and difficult to distinguish from double layer charging.

Pseudocapacitance has specifically motivated electrochemists to pursue methods for distinguishing between the fast, surface charge and the slower bulk insertion mechanism. Understanding which mechanism dominates in different materials and different electrode structures aids in the design of electrodes suited for the desired application.

2.6 Methods for Electrochemical Testing

Most analytical testing was carried out in 3-electrode test cells, which utilize separate electrodes as counter and reference electrodes, to decouple current density at the counter electrode from the measured cell voltage. Beaker cells which are open to the atmosphere will utilize Ag/AgCl reference electrodes with platinum counter electrodes, while sealed Swagelok cells were used with Li foil as the counter and reference. All of the following testing can be carried out in either cell design.

2.6.1 Cyclic Voltammetry

Cyclic voltammetry (CV) is a technique that scans the working electrode through a range of potentials at a linear scan rate (v), while recording the current response. CV is a versatile electrochemical characterization technique, and the location and size of the current peaks in a CV can be used to identify the Nernst potential of a reaction and evaluate reversibility. The behavior of redox peaks over a range of different scan rates can be used to characterize the rate limitations of the reaction kinetics and to evaluate the

reversibility of the charge storage reactions. The differences in the kinetic responses can be established clearly from the two different transients, and their response to scan rate increases allows additional analysis of their kinetics.

Two main methods can be employed to deconvolute diffusion-limited and charge-transfer-limited charge from cyclic voltammetry. The first was developed by Trasatti to distinguish the “inner” and “outer” active surfaces of RuO₂, the first pseudocapacitive material observed.¹⁰³ This technique calculated the charge passed (q) during CVs at a variety of rates, and then extrapolates this charge performance to two extreme cases. First, the limit of the charge as the scan rate approaches zero can be calculated by the intercept of q vs $v^{1/2}$. This limit can be estimated to be the total possible charge stored in that particular electrode. At the other extreme, the charge as the scan rate approaches infinity can be calculated by the intercept of q^{-1} vs $v^{-1/2}$. This charge corresponds to only the very fastest surface charge, which will not be diffusion limited in any way. This surface charge may include only the EDL, or may include fast surface redox reactions as well. The difference between the total charge and surface charge then corresponds to the diffusion limited charge, which arises from any bulk reactions within the active material.

The second strategy for separating the fast surface charge from the slower, diffusion limited charge is Dunn’s method. Dunn’s method was introduced to distinguish the kinetics of charge storage in TiO₂ nanoparticles.¹⁰⁴ Dunn’s method starts with the assumption that the current at any given potential is the sum of the fast surface charging and the slower diffusion limited charge, which can be defined in terms of their scan rate dependence (Eq. 2-6).

$$i(V) = k_1 v + k_2 v^{1/2} \quad \text{Eq. 2-6}$$

The two scaling constants, k_1 and k_2 , represent the relative contribution of each component at a given potential, and can be calculated from the current response as a function of scan rate, shown in Eq. 2-7

$$\frac{i(V)}{v^{1/2}} = k_1 v^{1/2} + k_2 \quad \text{Eq. 2-7}$$

After k_1 and k_2 are calculated over the voltage range of interest, the two components of the current can be integrated separately to determine the surface charge, the bulk charge and their sum should be similar to the total charge measured. While this method provides a much more detailed look at the kinetics over the voltage window of testing, it can also be limited by peak shifting or broadening, which prevents the current and scan relationship from remaining linear.

2.6.2 Galvanostatic Cycling

Galvanostatic cycling is a potentiometric technique that mimics the simplest typical use of a battery or supercapacitor in normal applications. A constant current is applied and the response of the potential is recorded. This is the simplest technique for determining the specific capacitance of a working electrode, and power capabilities can be evaluated by increasing the applied current. The thermodynamics of the electrochemical reaction taking place determines the discharge profile, and the time to discharge through the established voltage window determines the total charge stored. To understand rate performance using galvanostatic cyclic, the current density is increased, yielding results that are often similar to the impact of increasing scan rate during cyclic voltammetry. Higher rates are often reported simply by the constant current which is

applied, or the current density (i.e. A/g or A/cm²). However, a notation referred to as C-rate is also often used to designate the applied current density during testing. The 1C rate is the current needed to discharge the battery in exactly 1hr. This is determined by the theoretical capacity of the material and its mass loading within the electrode. All other C-rates are multiples of the 1C current, as designated by the numeral. For example C/10 is one tenth of the 1C current, and the electrode will theoretically require 10 hours to discharge at the C/10 current. Conversely, 10C is 10 times the 1C current, and the electrode will theoretically fully discharge in 6 minutes. The simple conversion from C-rate to time-to-discharge provides some convenience when attempting to compare C-rates to cyclic voltammetry, and provides some useful time scale context to rate performance data. As a result, this current density designation is widely used in the literature, and is used when reporting galvanostatic results throughout this dissertation.

2.7 Conclusions

Anodized aluminum oxide templates, coupled with electrodeposition or atomic layer deposition provide a platform for creating both 1D and 3D structures with controlled structural parameters which will facilitate exploration of cathode structure on rate performance and degradation. A variety of structural and electrochemical analysis techniques can be combined to produce a broad understanding of nanostructure electrodes for energy storage devices.

Chapter 3: 1D and crosslinked anodized aluminum oxide for controllably modified electrodes

Portions of this chapter have been published in Phys. Chem. Chem. Phys 2015, 17 (5).

My contribution to the publication is the majority of the written analysis, as well as the development of the electrodeposition method and the characterization of the resulting Ni structures. I also prepared the samples that were submitted to FEI for FIB/tomography and TEM.

3.1 Introduction

Deposition of active materials into 3D anodized aluminum oxide structures is a critical step towards utilizing the 3D crosslinked structures as testbed electrodes in lithium ion battery studies. The transition from 1D to 3D deposition can be challenging, as it is critical to ensure that any deposition method is sufficiently conformal to the 3D morphology of the templates to retain the desired shape and size. Two different deposition methods are explored here, utilizing the modified anodized aluminum structures demonstrated by previously in our group by Dr. Sherrill, and discussed in Ch 2.⁷⁷ Electrodeposition and atomic layer deposition are both demonstrated as potential strategies for creating 3D electrodes within these modified AAO structures.

Electrodeposition into AAO templates has traditionally taken place in free-standing templates, after the removal of the aluminum and etching of the remaining barrier layer. A current collector is then sputtered onto the back of the template, and material is electrodeposited through the pores. Potential or current can be used to drive electrodeposition, and a wide variety of materials have been demonstrated by this technique, including metals,^{105,106} metal oxides¹⁰⁷ and polymers.^{108,109} It is also possible to electrodeposit directly onto the native aluminum substrate, if a barrier layer thinning

technique has been used to provide adequate contact between bare Al and the electrolyte, and the potential is controlled to avoid oxidation of the Al itself.⁷⁴ However, constant potential or constant current deposition methods are unreliable for this technique, because of the relatively high interface resistance at aluminum surfaces.¹¹⁰ Pulsed current or potential are generally used, and can be applied as a square pulse, or by taking advantage of alternating current techniques.^{73,111} Electrodeposition is appealing because of the broad range of materials and deposition strategies which can be employed as long as a conductive substrate is readily available.

Atomic layer deposition (ALD) does not require an electrical connection, and is popular for its surface limited, substrate conformal coating. This technique allows deposition into AAO which avoids issues with the barrier layer. However, ALD can suffer from conformality problems in high aspect ratio structures. As the tortuosity of the templates increases, and as their surface areas increase, ALD processes must be carefully calibrated to ensure good coatings.

Here we demonstrate the use of modified AAO templates as electrodes, using electrodeposition and ALD into high-aspect-ratio AAO templates. For both techniques there are advantages and disadvantages for fabricating template synthesized electrodes, which will be discussed in detail.

3.2 Methods and Materials

3.2.1 Anodized Aluminum Oxide

The AAO templates were prepared from Al foil (0.25 mm thick, 99.99%, Alfa Aesar) using a traditional 2-step anodization process. Briefly, the Al foil was degreased in acetone, and then electropolished for 5 min at 15 V in an 11 % perchloric acid in

ethanol at 3 °C. The first anodization was performed in aqueous 0.3 M oxalic acid solution at an anodization potential of 40 V, at 8 °C, for 7 hours. The Al₂O₃ was etched in phosphoric acid (6 wt. %) and chromic acid (1.5 wt. %) at 60 °C for 4 hours and 40 minutes. The second anodization was performed in 0.3 M oxalic acid held at 8 °C, but with varying potential profiles to introduce branching and merging of pores or barrier layer thinning. Branching and merging was introduced by stepping the voltage in 2 V/30 s steps down to 20 V and then back to 40 V. Barrier layer thinning was achieved by dropping the voltage at the end of an anodization sequence from 40 V to 15 V at a rate of 0.09 V s⁻¹. The two techniques are compatible, and can be combined as needed. Pore widening was carried out in 5% H₃PO₄ at 38 °C for 11.5 minutes, unless otherwise stated.

3.2.2 Electrodeposition of Ni

Electrodeposition was performed in a three electrode system using a Biologic VSP potentiostat. Nickel nanowires were deposited from a solution containing 1 M nickel sulfate and 0.4 M citric acid by AC deposition, at a frequency of 2 Hz, between 0 and -2 V vs. Ag/AgCl. For some SEM and all TEM imaging, the AAO template was removed by soaking for 10 min in 3 M NaOH.

3.2.3 Atomic Layer Deposition

Because no electrical connection is required for the deposition of the material, the barrier layer thinning process is not used in any of the templates used to demonstrate atomic layer deposition.

Ru ALD

All Ru films were deposited by Chanyuan Liu in Dr. Gary Rubloff's group

A custom built ALD reactor, described in detail previously,^{112,113} was used to deposit Ru films, using a process developed in Dr. Gary Rubloff's group and described in detail elsewhere.¹¹⁴ Briefly, bis(2,6,6-trimethyl-cyclohexadienyl)ruthenium ($\text{Ru}(\text{C}_9\text{H}_{13})_2$) was used as the Ru source, and O_2 was used as the oxidant, at a temperature of 300 °C.

V₂O₅ ALD

A commercial reactor, BENEQ TFS 500 was used for atomic layer deposition (ALD) of V_2O_5 , as described previously.¹¹⁵ Briefly, vanadyl triisopropoxide, $\text{VO}(\text{OC}_3\text{H}_7)_3$, was used as the vanadium source, designated VTOP, and ozone, O_3 , was the oxidant. 2 s pulses of VTOP were followed by a 4 s purge pulse. Oxidation took place in a 3 s pulse of O_3 , followed by 6 s of purge. The process was repeated 300 times at 170 C to achieve films roughly 20 nm in thickness.

3.3 Results and Discussion

3.3.1 Electrodeposition

In our laboratory, AC deposition was used to successfully demonstrate electrodeposition through the thinned barrier layer, resulting in free standing 1D and 3D nanostructure arrays directly deposited onto the native aluminum substrate.⁷⁷ The resulting 1D nanowire arrays can be seen in Figure 3-1.

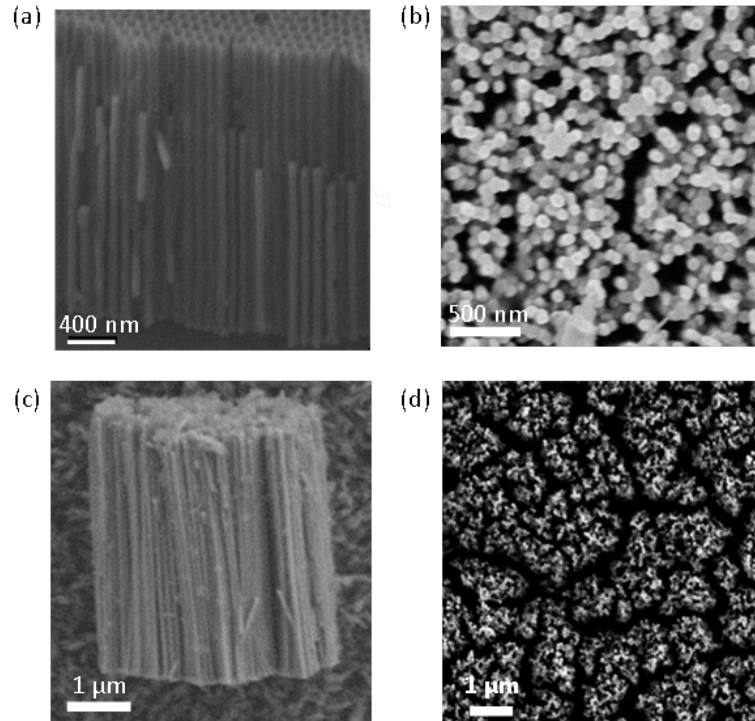


Figure 3-1: (a) Ni nanowires within AAO template (b) Ni nanowire released from the AAO template (c) Bundle of released Ni nanowires (d) Large area covered with free standing Ni nanowires

Figure 3-1a shows the nanowires as synthesized within the AAO template. The uneven lengths and a few empty pores may be the result of the cross-sectioning process, which requires bending the Al/AAO/Ni films until they crack. After the template is removed, Figure 3-1b and 3-1d show free-standing forests of Ni nanowires with fairly dense packing and uniform length. This observation suggests that there is good, even deposition across the whole template, which is indicative of good barrier layer removal across the whole template. Figure 3-1d shows a large area of nanowires, which show typical aggregation and clumping, which is expected for free standing forests of high aspect ratio nanowires after drying. Figure 3-1c shows a bundle of Ni nanowires released from the surface by scratching. Again, their length is quite uniform. The AC deposition method appears to be successful for depositing Ni into the barrier layer thinned pores.

Additionally, to demonstrate that the barrier layer thinning and the pore branching and merging were in fact compatible, Ni nanowires were deposited into the crosslinked templates as well. These templates were fabricated by a voltage stepping method described previously.⁷⁶ However, detailed characterization of the structure of the crosslinked pores was limited by the available microscopy methods. Further investigation was carried out with assistance from FEI, who generously demonstrated 3D tomography by SEM, and ion milling and TEM for the preparation of cross sections of the crosslinked AAO templates.

Tomography was carried out in a dual beam focused ion beam (FIB)/scanning electron microscope (SEM). SEM images were taken of the cross section surface, and after 2nm of ion beam etching, for 100 cycles of etching. Images taken during this process can be seen in Figure 3-2.

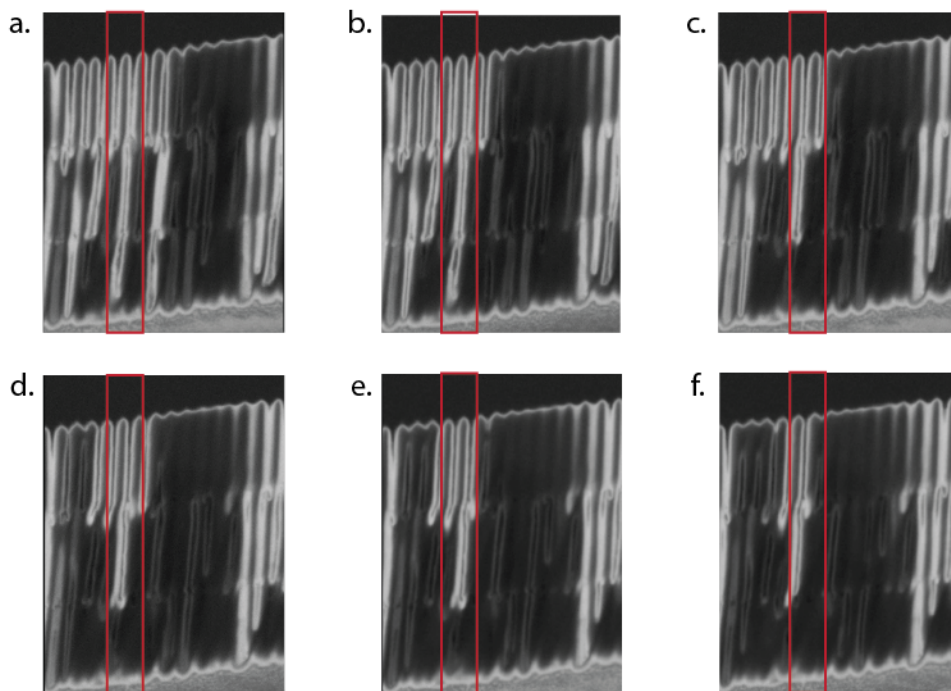


Figure 3-2: SEM images taken from consecutive FIB slices of a two branched AAO template. Each slice is separated by ~2nm of depth.

The very bright regions in these images are due to charging effects in the SEM on the non-conductive anodized aluminum oxide surface. However, despite this issue, the pores can be clearly seen, and in the progression of frames, the pores three dimensional nature of the pore interconnections is visible. One example of a region where interconnections are observed through the depth of the templates is highlighted in red in Figure 3-2. In the highlighted region, the progression of frames shows the disappearance of the bottom region of the pore, while the middle and top regions remain open. This suggests the branching interconnects two pores whose centers are offset. Interconnections between adjacent pores in the plane of the imaging are also clearly visible.

Transmission electron microscopy is not a technique which has been broadly applied to the analysis of anodized aluminum oxide pore structures, because of the technical challenges related to achieving stable cross sections which are thin enough to be

penetrated by the electron beam.⁵⁴ However, again thanks to the help of FEI Co., TEM images were obtained from the templates. The template was protected and mounted in a carbon matrix, which was sliced by microtome and then thinned by focused ion beam (FIB). High angle annular dark field (HAADF) images of the resulting cross sections can be seen in Figure 3-3.

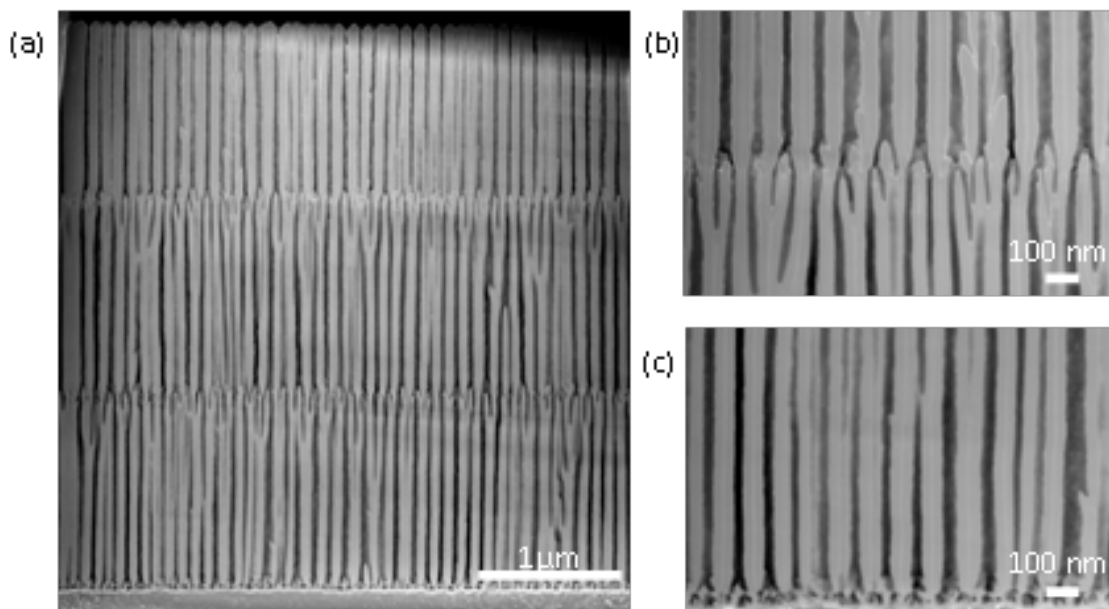


Figure 3-3: HAADF TEM images of FIB thinned AAO templates. (a) the full template with two (b) branched regions and (c) a thinned barrier layer

Figure 3-3a shows an overview of the whole template, while Figure 3-3b and 3-3c show close up images of a branched region and of the thinned barrier layer respectively. It should be noted that these images were obtained for a sample without any pore widening, to retain structural integrity during the FIB thinning process. The branches can be clearly seen forming from the main channel and growing without strong directional orientation. While they are somewhat thinner than the main pore channels, as would be expected by the drop in anodization voltage, they rarely drop below ~20 nm in width. However, the features of the barrier layer, seen in Figure 3-3c, are much smaller and are

quite disordered. These features should be more dramatically influenced by the pore widening process, which etches away aluminum oxide. However, these images also clearly shows how easily these structures can become over-etched and delaminate complete from the aluminum substrate.

Based on anodized aluminum oxide templates which utilized both the branching and barrier layer thinning techniques, electrodeposition of cross-linked Ni networks should be possible. Direct deposition onto the Al substrate was achieved by the same electrodeposition technique that was used for the straight pores. Figure 3-4 shows the results of the deposition.

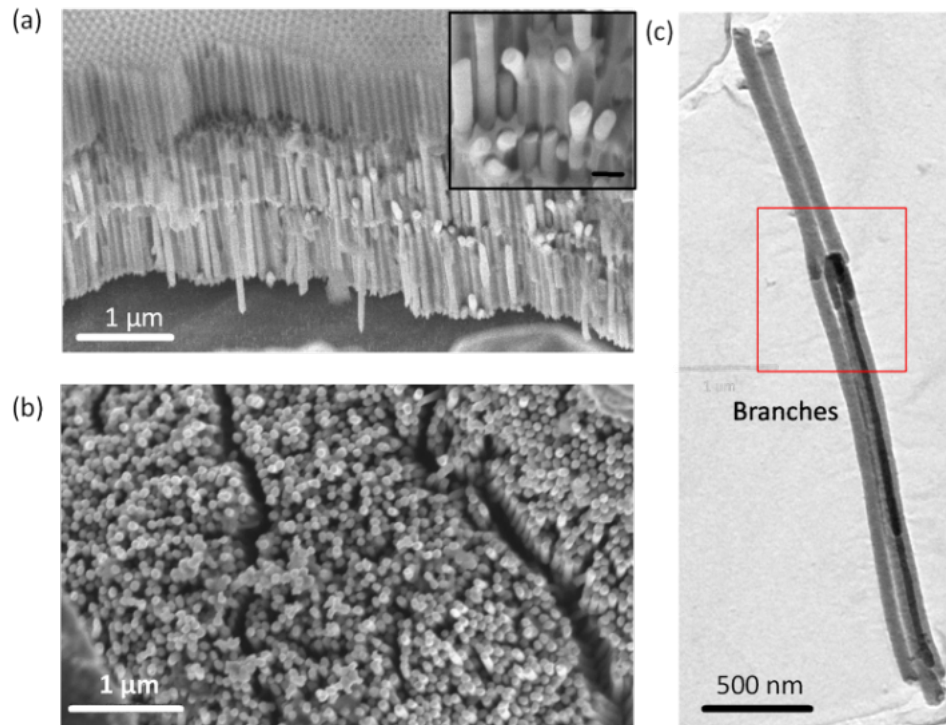


Figure 3-4: Nickel deposition into branched AAO pores. (a) SEM image of the nanowires within the branched template (Inset: close up of the branched region) (b) SEM image of free standing wires after AAO removal (c) TEM image of a bundle of branched Ni wires released

Figure 3-4a shows the Ni nanowires as grown in the AAO pores, with a closeup of the branched region in the inset to highlight the interconnections to pores outside of the plane of the cross section fracture. Figure 3-4b shows the Ni nanowires on the Al substrate after the AAO has been removed. The regular packing of the nanowires does not have the same aggregation seen in the straight nanotubes under the same conditions (Figure 3-1d). This observation suggests that the interconnections provided by the branched AAO results in a more structurally stable nanocomposite. Figure 3-4c shows a TEM image of several nanowires interconnected at a branched region, indicating again that there the Ni does fill the branched spaces and provide interconnections between adjacent nanowires.

However, delamination of these structures from the underlying Al is observed under extensive handling of the samples, which provides processing challenges. The structure of the thinned barrier layer, as shown in the TEM imaging previously, suggests that only relatively small regions of connection between the Al and the open pore above are truly available for Ni deposition, leading to relatively fragile connection to the current collector once the template is removed.

Additionally, no successful deposition was carried out for any non-metal material directly onto the Al substrate. The reduction overpotential required for Ni deposition was quite high (-2 V vs. Ag/AgCl versus Ni/Ni²⁺ standard reduction potential of -0.45 V vs Ag/AgCl) in order to overcome the interfacial resistance at the Al surface, where a native oxide forms nearly instantaneously in aqueous solutions. This issue makes generalizing electrodeposition techniques quite difficult, and deposition at oxidative potentials is especially problematic.

In conclusion, electrodeposition is an appealing approach generally, because of its wide material compatibility and stability. However, to work with structures that are less than 25 μm thick, the barrier layer thinning technique and deposition directly onto the Al are required. The aluminum substrate limits our material choices to those that can be deposited at highly reductive potentials, under pulse or alternating current conditions. Therefore, in order to work with a more conventional cathode material in these templates, a different approach to material deposition is required.

3.3.2 Atomic Layer Deposition

ALD is an appealing material deposition strategy because of its atomic precision and surface limited coating. However, it requires air and water sensitive precursors, handled in high vacuum systems, so the materials available to use are limited by the equipment available. Here we will discuss one metal and one metal oxide for which precursors and ALD reactors were readily available.

First, to show that the ALD process can conformally coat the branched surfaces of AAO, Ru metal was deposited into a 25 μm long, single branched, templates as shown in Figure 3-5. The Ru precursors penetrate well in the high-aspect-ratio structures, although certainly not the full length of the available 25 μm . However, the process does produce nearly 10 μm long nanotubes, which is excellent conformality for an ALD process. The full length of the nanotubes can be seen in Figure 3-5a, with the branched region clearly visible near the bottom of the image. The Ru structure was sonicated after AAO removal, which results in the separation and disorder observed far from the branch points in Figure 3-5a. The tightly retained order near the branched region indicates strong connections between adjacent pores resulting in a stable three dimensional network. Figure 3-5b

shows a close-up of the branched region, where the shape and size of the branches are clearly visible, demonstrating that good conformal coating is retained in these regions. This result confirms that ALD is an effective deposition method within our networked AAO templates.

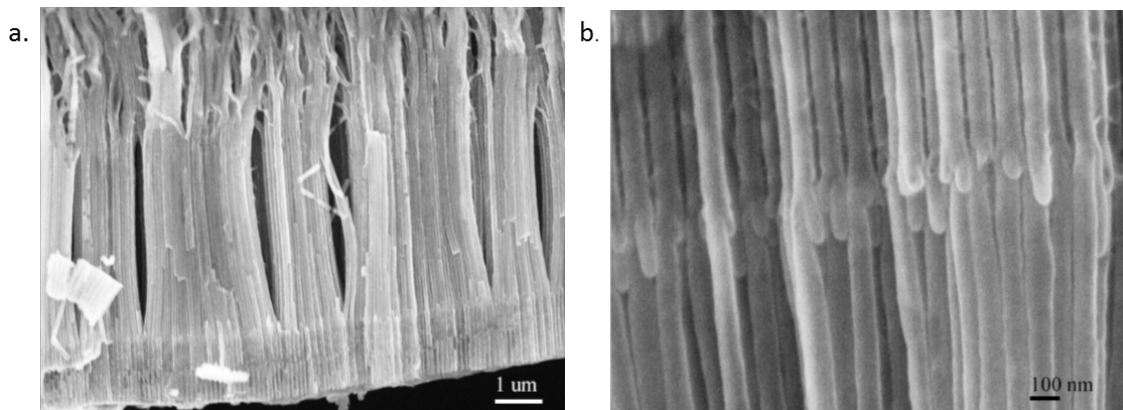


Figure 3-5: Ru nanotubes released from an AAO template with a single branched region. (a) the full length of the Ru nanotubes (b) a close-up of the branched region

Vanadium oxide was chosen as a cathode material for further investigation because extensive work developing the ALD process and characterizing the resulting material had already been carried out. The process for the deposition of crystalline vanadium oxide was developed by Xinyi Chen¹¹⁶ and this V_2O_5 process has been used to demonstrate several novel electrode geometries previously.^{88,117} However, the V_2O_5 process is generally less conformal than the Ru process and it had not been characterized in more complex porous networks. Therefore, we examined the potential for the V_2O_5 ALD process to adequately coat high-aspect ratio, 3D structured AAO templates.

First, SEM imaging was used to characterize the V_2O_5 deposition into branched AAO templates, shown in Figure 3-6. Figure 3-6a shows the top three layers of a multiply branched template, which 5b shows a close up of the second branched region.

The rough and bright edges of the structure are the V_2O_5 coating, which is estimated to be ~20 nm thick. The roughness appears to indicate a slightly less ideal ALD deposition, which is not as uniform and smooth as the Ru deposition. Figure 3-6c is the region of the template selected for energy dispersive spectroscopy (EDS), and the corresponding line scan can be seen in Figure 3-6d. The top three layers of the template are visible, with branched regions separated by 1125 s of ordered growth, corresponding to approximately 1.25 μm of straight pore between each branched region. The EDS line scan reveals relatively uniform distribution of vanadium throughout the structure. Conversely, gold deposited by sputtering on top of the template penetrates less than a 1 μm into the structure. This is a clear example of the advantage of ALD over other vacuum deposition techniques. Based on this result, we have confidence that the conformality of V_2O_5 in AAO is adequate up to at least 4 μm long structures.

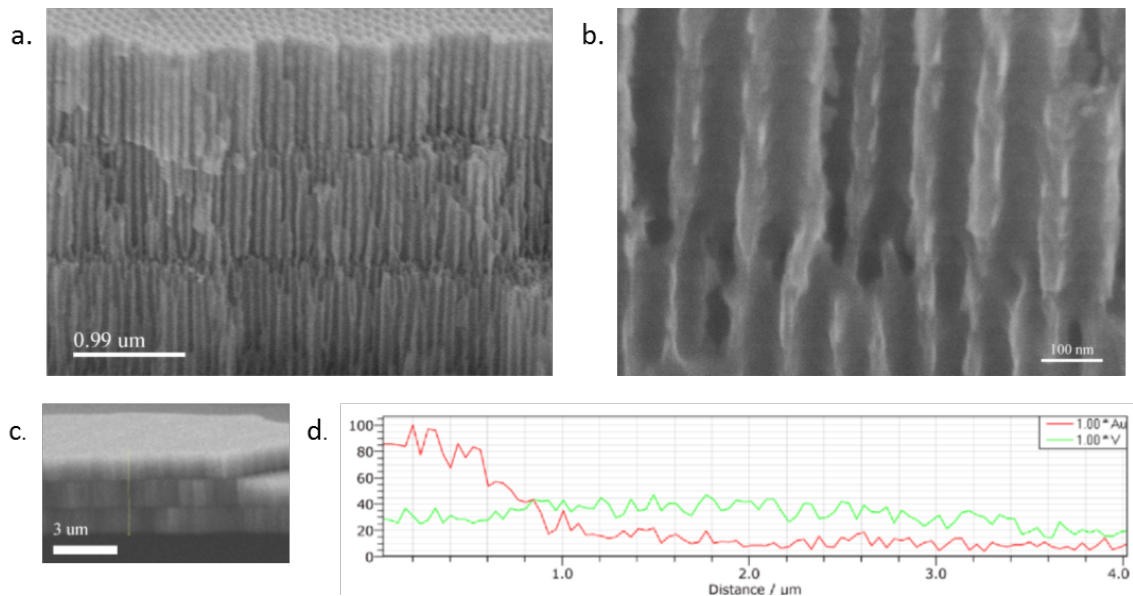


Figure 3-6: SEM images of branched templates coated with V_2O_5 (a) three layers of a two-branched template (b) a close up of the branched region (c) region for EDS line scan (d) EDS line scan result

There is no appropriate etching strategy that can remove the AAO without damaging the V_2O_5 , so more detailed microscopy was not possible on these structures. However, if they were going to be effective electrodes less than $4\mu\text{m}$ long, a current collector was still needed. The underlying Al retained a high interfacial resistance and was not useful as a current collector. Additionally, the V_2O_5 surface along the top of the AAO was rough, leading to high resistance which prevented direct connection to the top of the pores. However, a thin sputtered layer of gold, like the one seen in Figure 5, was sufficient to provide good electrical connection along the top of the template. To take advantage of this connection route, ring-shaped copper current collectors were placed on top of the Au/ V_2O_5 /AAO structures, and then masked with Parafilm to prevent electrolyte contact to the copper. In this way, the templates could successfully be connected to external circuits for electrochemical testing. A representative CV trace is shown in Figure 3-7.

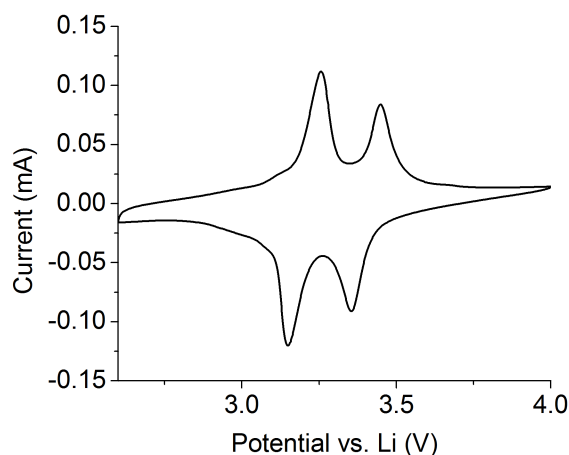


Figure 3-7: Cyclic Voltammogram at a scan rate of 0.5 mV/s showing the characteristic peaks corresponding to 1 Li insertion and deinsertion into V_2O_5

The two characteristic insertion peaks of V_2O_5 are clearly visible, with lithiation peaks at 3.36 V and 3.15 V, and delithiation peaks at 3.25 and 3.45 V vs Li/Li^+ . The difference between the anodic and cathodic peak positions is small, indicating a reversible reaction. There is also little slope to the CV trace, indicating relatively small resistance in this configuration. This electrode configuration is appropriate for further testing, and will be used throughout chapters 4 and 5.

3.4 Conclusion

Anodized aluminum oxide templates with both ordered 1D and more complex 3D structures can be used as templates various nanomaterials. Electrodeposition of Ni was successfully demonstrated directly onto the Al substrate underlying both 1D and 3D networked AAO structures. ALD was also demonstrated in the 1D and 3D structures. ALD facilitated the conformal deposition of an excellent cathode material which was successful integrated into electrodes which demonstrated reversible lithiation and delithiation responses. This technique was chose to move forward for further studies into the relationship of structure and electrochemistry in lithium ion battery cathodes.

Chapter 4: Finite Element Analysis and Nanostructured Electrodes

Portions of this chapter have been published in . Nat. Nanotechnol. 2014, 9, 1031–1039. Individual contributions will be noted in the text.

4.1 Introduction to Finite Element Analysis Modeling

Computational modeling is a critical component of modern research, and has been used to great effect in electrochemical systems for many years.¹¹⁸ Three main approaches are generally used; atomistic modeling, continuum modeling and circuit modeling.

Atomistic modeling, using techniques like molecular dynamics and density functional theory is excellent for understanding the thermodynamic properties of materials, but is unable to capture electron transfer dynamics.¹¹⁹ Additionally, atomistic simulations, which must calculate every atom in the system of interest, are generally unable to capture dynamics on micrometer scales.

Circuit based modeling treats an energy storage device a series of capacitors and resistors, and is often used to help understand how a well characterized full device will interact with different electric loads.¹²⁰ Equivalent circuit models can also assist in the interpretation of frequency response data from an electrochemical device, collected by electrochemical impedance spectroscopy.¹²¹ However, the more complex an electrochemical system is, the more variables are introduced in these types of models, and results can be quite difficult to validate.

Continuum modeling involves solving equations for the physical behavior of an electrochemical system, neglecting the locations of exact atoms by treating materials as continuums which have defined characteristics. Finite element analysis is a common strategy used to apply this type of modeling, which essentially breaks a physical system of differential equations into smaller domains, called elements, to approximate the

solution to the larger system. This is the most appropriate strategy for the micrometer scale of the nanotubes used in our experimental system. However, the very thin active material layers may approach the limit of continuum models, where nanoscale effects related to atomic scale phenomenon may begin to appear. While finite element analysis is well validated for conventional porous electrodes, care must be taken to ensure the validity of the models in any nanoscale system.^{122,123} We use Comsol Multiphysics, with a built in Li Ion Battery interface to model the nanotube systems. The basis of Comsol's system of equations is taken from earlier models by Newman and coworkers, which have been used extensively for conventional batteries.^{124,125}

4.2 Methods

Here we will introduce the general modeling method that COMSOL Multiphysics uses to model a lithium ion battery system. Details of how this general method is applied to our specific cathode system will be detailed in the results and discussion section.

Four dependent variables are solved over the various domains of a lithium ion battery model. Electrolyte potential (ϕ_l), electrode potential(ϕ_s), Li concentration in the electrolyte (c_l) and Li concentration in the electrode (c_s) are the four variables, with subscripts denoting whether they are solved in the solid phase (s) or in the liquid phase (l). The input information required is depicted in Table 4-1.

Symbol	Explanation	Unit
σ_s, σ_l	Conductivity in the electrode and electrolyte	$S m^{-1}$
D_s, D_l	Li Diffusion coefficients in the electrode and electrolyte	$cm^2 s^{-1}$
c_{smax}	maximum concentration of Li in the electrode	$mol m^{-3}$
A_v	Specific surface area of the electrode	m^{-1}
E_{eq}	Equilibrium Potential	V
α	Transfer Coefficient	[1]
ϵ_s, ϵ_l	Electrode and Electrolyte volume fractions	[1]
t_+	Cation transport number	[1]
f	Ionic activity coefficient	[1]

Table 4-1: Table of symbols used in the COMSOL Multiphysics models of lithium ion batteries

A series of differential equations are required in various parts of the battery geometry. In the electrolyte, current is defined by the electrolyte properties (Eq. 4-1) and linked to the flux in the electrode, Q (Eq. 4-2)

$$i_l = -\sigma_l \nabla \phi_l + \frac{2\sigma_l RT}{F} \left(1 + \frac{\delta \ln f}{\delta \ln c_l}\right) (1 - t_+) \nabla \ln c_l \quad \text{Eq: 4-1}$$

$$\nabla i_l = Q \quad \text{Eq 4-2}$$

Ohm's law is used to define ϕ_s (Eq. 4-3).

$$i_s = -\sigma_s \nabla \phi_s \quad \text{Eq. 4-3}$$

Charge balance is maintained in the electrode by Eq 4-4.

$$\nabla i_s = -i_{tot} + R_s \quad \text{Eq 4-4}$$

R_s is an arbitrary source term, which can be used to define the external current load.

The lithium mass balance in the electrode is controlled by diffusion (Eq. 4-5).

$$\frac{\partial c_s}{\partial t} = \nabla \cdot (-D_s \nabla c_s) \quad \text{Eq. 4-5}$$

The lithiation reaction flux is governed by the following boundary conditions (Eq. 4-5 and 4-6), which here assume a spherical particle with radius r_p . The Li flux is zero at the center of the particle, and is determined by the molar flux of lithium (R_{Li}) at the particle surface

$$\frac{\partial c_s}{\partial r} = 0 \text{ for } r = 0 \quad \text{Eq. 4-5}$$

$$-D_s \frac{\partial c_s}{\partial r} = -R_{Li} \text{ for } r = r_p \quad \text{Eq. 4-6}$$

The total current (Eq 4-7) and the molar flux (Eq. 4-8) are determined by the specific surface area (A) of the electrode, along with the other structural features.

$$i_{tot} = \sum A i_{loc} \quad \text{Eq 4-7}$$

$$R_{Li} = \sum \frac{v_{LiO} i_{loc} A}{nF (\varepsilon_s)/r_p} \quad \text{Eq. 4-8}$$

v_{LiO} and n are stoichiometric coefficients for the reaction being modeled, and ε_s denotes the electrode volume fraction. The local current is determined by the Butler-Volmer equation (Eq. 2-5), where the overpotential (η , Eq. 4-9) is defined by the input equilibrium function E_{eq} , which depends on the electrode state of charge (soc, Eq. 4-10) and the two potential variables.

$$\eta = \phi_s - \phi_l - E_{eq}(soc) \quad \text{Eq 4-9}$$

$$soc = \frac{c_s}{c_{smax}} \quad \text{Eq 4-10}$$

For current balance, $\phi_s = 0$ at the negative electrode, while current density is specified at the outside boundary of the positive electrode. The electrolyte concentration is defined as

the initial condition, and all boundaries except the electrode boundary are defined with no electrolyte flux.

Clearly, there is not a simple analytical solution to this extensive system of partial differential equations, but using the finite element method, approximate numerical solutions can be obtained.

Meshing, or determining the size and shape of the finite elements is a critical component to all finite element analysis. While smaller elements provide more detailed results, which may provide more accuracy, smaller elements also increase computational time. Care is taken during meshing to ensure that the element size is not affecting the results, and comparison to an experimental system can be critical for validating the models. Here, all models have been validated against experimental results for planar V_2O_5 coin cells to ensure reasonable, physical results were being obtained.

While finite element analysis can be quite helpful for understanding a complex system like a battery, it does have some shortcomings which are important to understand. It is a continuum modeling system, and is not sensitive to any nanoscale effects like electron scattering. The Newman models for battery systems in particular have a few underlying assumptions of homogeneity which limit their broad use for heterogeneous materials, and which tend to undermine their accuracy at very high rates or long cycle lives, where degradation mechanisms outside of the basic battery chemistry come into play. Nonetheless, even an idealized modeling system can be a useful reference point for understanding the dynamics of this complex system.

In particular, modeling can provide some insight to the voltage distribution and associated reaction rates locally in an electrode, while experimental measurement methods generally only collect data averaged over the whole structure. This can provide some insight into critical parameters related to structure which may influence rate performance or degradation.

Here we investigate the ability of COMSOL Multiphysics models to provide predictions about nanostructured electrodes, and the use the models to help illustrate the advantage of integrated current collectors for an optimized nanostructured battery.

4.3 Results and Discussion

Vanadium oxide cathode electrode structures are the experimental system of interest, and so the models were implemented to mimic the half-cell configuration in which experimental testing took place, which featured lithium anodes and a 1:1 ethylene carbonate (EC):diethylene carbonate (DEC) electrolyte with 1M LiPF₆. The relevant parameters for the anode and electrolyte are from Comsol's built in interfaces for Li and LiPF₆ in DEC/EC are in Table 4-2 and 4-3, respectively.

Table 4-2: Electrolyte parameters

D _{Li}	$3 \times 10^{-10} \text{ m}^2 \text{ s}^{-1}$
Transference number	0.22
c _{ref}	1000 mol m^{-3}
conductivity	See Fig 4-1

Table 4-3: Anode parameters

E _{eq}	0 V
α _a , α _c	0.5
k _a , k _c	$2 \times 10^{-11} \text{ m s}^{-1}$
ν _{Li}	1
ν _{An}	0

Cathode parameters are shown in Table 4-4, and are derived from the literature or physical properties of V₂O₅, except for the function for E_{eq}, which is derived from experimental data, discussed in more detail in section 4.3.1.²²

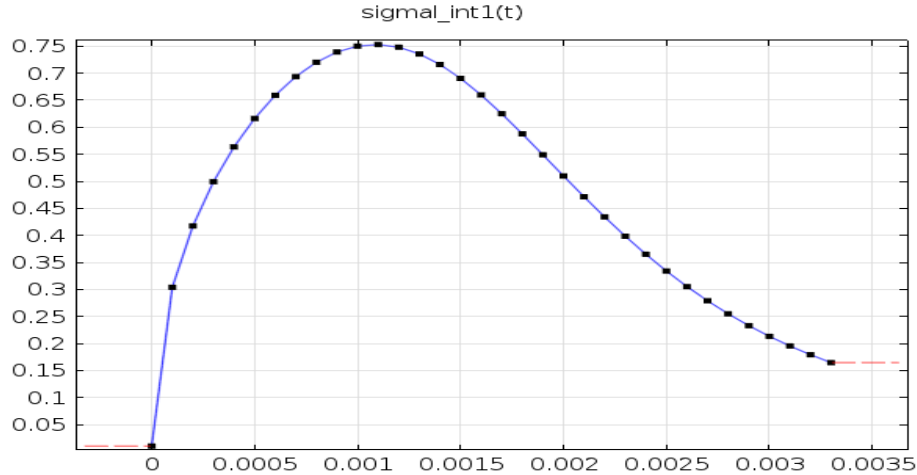


Figure 4-1: Interpolation function of electrolyte conductivity vs. c/c_{ref}

Table 4-4: Cathode parameters

E_{eq}	See section 4.3.1
α_a, α_c	0.5
k_a, k_c	$2 \times 10^{-11} \text{ m s}^{-1}$
ν_{Li}	1
$c_{s,int}$	15 mol m^{-3}
ϵ_s	1
c_{ref}	1 mol m^{-3}
conductivity	0.005 S m^{-1}
D_{Li}	$3 \times 10^{-17} \text{ m}^2 \text{ s}^{-1}$
c_{max}	18473 mol m^{-3}

4.3.1 Validation

Models were validated by comparison to experimental data collected by Xinyi Chen (all planar data) and Chanyuan Liu (all electrodes fabricated in commercial AAO)

First, models were built to compare to planar electrodes, and compared to data collected for various V_2O_5 thicknesses deposited by ALD on stainless steel discs. These tests were carried out in a voltage window from 4.0 to 2.1 V vs. Li/Li^+ , facilitating the insertion of 2 Li/V_2O_5 . The equilibrium function E_{eq} needed to be derived from experimental data, preferable at a very slow rate, where the maximum possible capacity of the material would be utilized. Initial validations, therefore, used Figure 4-2 as the

input function, which was derived from the discharge curve of a V_2O_5 coated multiwalled carbon nanotube electrode at a very slow rate ($C/10$, ie a 10 hour discharge time). At the time, the active experimental research being carried out by Xinyi Chen was focused on these types of heterogeneous electrodes, and so this was the only extremely low rate data available.

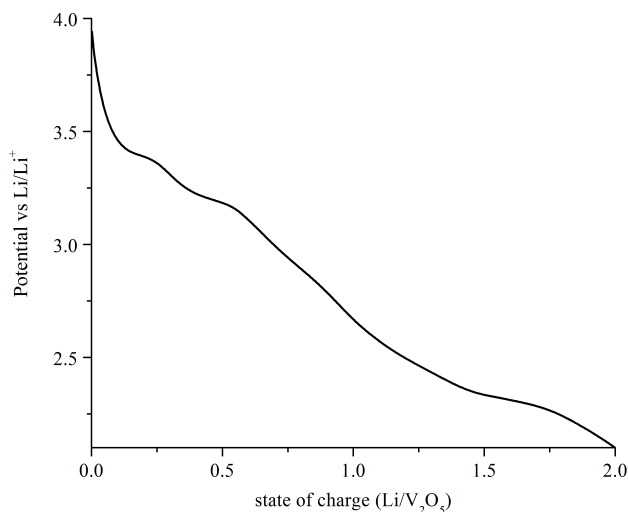


Figure 4-2: Potential as a function of Li fraction, derived from the discharge curve of V_2O_5 MWCNTs discharged at a $C/10$ rate

Using the V_2O_5 /MWCNT input function, a series of models were run while data was collected for a set of comparison electrodes, which were simply thin films of V_2O_5 deposited on stainless steel discs. Four different thickness of film were tested and modeled. The percent capacity retained for the model system and the experimental results can be seen in Figure 4-3.

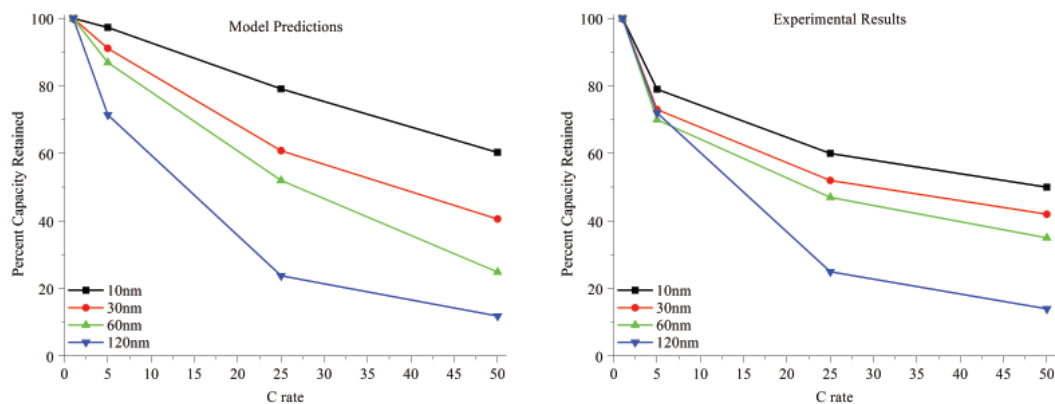


Figure 4-3: Model predictions and experimental results for the % capacity loss with increasing discharge rate

While the general trends are similar between the experimental and modeling results, particularly for the thickest electrode (120 nm, blue triangles in both graphs), the model predicts quite a more linear decrease in capacity than is observed in the experimental data. This deviation may have arisen from the input function derived from the composite electrode. Even at very low rate, the discharge data may have been sensitive to structural limitations related to tortuosity or inhomogeneity in those electrodes which were not present in the thin film tests. In order to move towards more focused studies of the V_2O_5 material and its particular structure, a more deliberate approach was needed.

New data was collected by Xinyi Chen at the C/10 rate for planar electrodes on stainless steel, to provide more accurate input functions for the modeling. Xinyi Chen and Chanyuan Liu, carrying out the experimental processes, had also decided to focus on the smaller, 1 Li⁺ voltage window, and so the models were adjusted to reflect that. Function 3 was measured at a C/10 rate using a 30 nm thick V_2O_5 film on a stainless steel disc. This discharge curve, shown in Figure 4-4 has a less pronounced slope to the voltage

plateaus than Figure 4-2, immediately suggesting that it is closer to ideal discharge behavior.

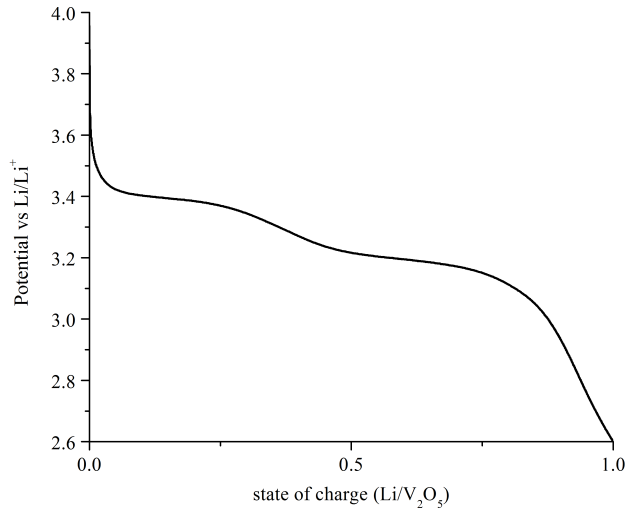


Figure 4-4: C/10 discharge curve for 30 nm of V₂O₅ on stainless steel

Using the improved input function, the model geometries were also updated for comparison to V₂O₅/anodized aluminum oxide electrodes, which provide an idealized porous structure which is much easier to directly model than the complex MWCNT sponges previously mentioned. The electrodes in the experimental work carried out by Chanyuan Liu and Xinyi Chen utilized commercial AAO templates with pore diameters of ~150nm and pore lengths of ~ 50µm. However, the ALD process was unable to effectively coat 50µm of the porous structures, and was generally characterized to be tapering and terminating between 5 and 10 µm into the structures. The V₂O₅ thickness was ~25 nm. COMSOL models were configured based on this geometry, but to keep computation times manageable, single pores were modeled in axisymmetric 1D geometries, limiting the model geometry to essentially a cross-section slice of a single

pore, These models were validated by comparison to the V₂O₅ AAO electrodes, and the COMSOL predictions are shown with the measured results in Figure 4-5.

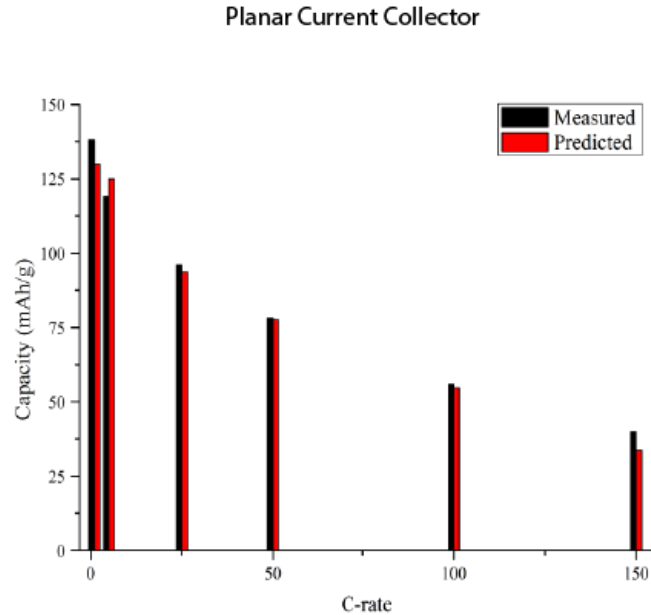


Figure 4-5: Measured and predicted capacity for V₂O₅ nanotube electrodes

The measured and predicted values no more than 10% different until the extremely high rate of 150 C. This suggests that the new input function is providing improved predictions and that the model geometry is appropriate for comparison to the V₂O₅/AAO electrodes. Therefore, these models can be expected to provide some insight into the performance of high-aspect ratio electrode structures.

The major limitation to rate performance in this electrode system is expected to be electronic conductivity, since the aligned AAO structures provide ideal ion access to the active material. Therefore, an optimized electrode structure was proposed with a fully conformal current collector, which would extend into the pores underneath the V₂O₅ coating. The rate performance of the two electrodes (fabricated and tested by Chanyuan

Liu) is shown in Figure 4-6. It is important to note that the V_2O_5/Ru data is presented with the capacity of a Ru-only electrode subtracted, to ensure that only the V_2O_5 electrode performance is shown.

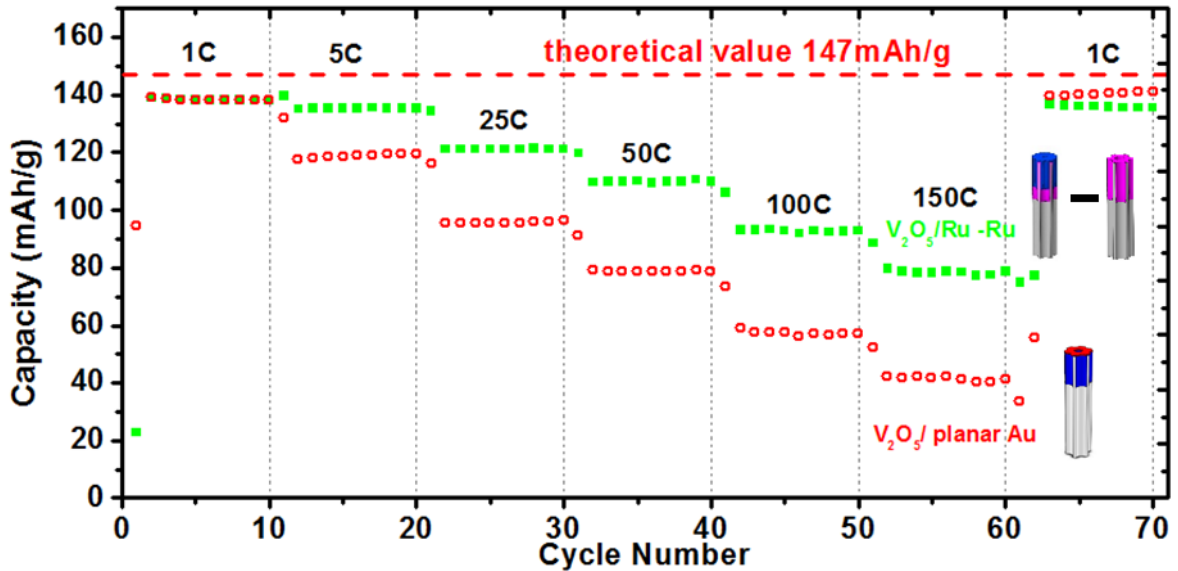


Figure 4-6: Capacity for different rates for the two experimental systems with different current collector configurations

When compared to the structure with the planar current collector alone, the electrodes with the conformal current collector perform significantly better, retaining two times the capacity of the planar current collector electrodes at 150C, despite a nearly identical low power performance (at 1C).

COMSOL models for the conformal current collector case are implemented simply by moving the boundary condition at which the current is applied from the bottom of the pore to the side wall. The simplicity of implementing structural changes in the modeling protocol is one of the advantages of the software. To confirm that the conformal current collector provides more uniform material utilization, the models were used to track the local potential along the length of the nanotube during discharge. Figure

4-7 shows these calculated discharge curves for the conformal and planar current collector cases at 25C. Three local potentials are plotted for each case, at the top of the nanopore (closest to the current collector, in the planar case), a midpoint 5um away from the pore top, and the bottom, a full 10um away from the current collector in the planar case.

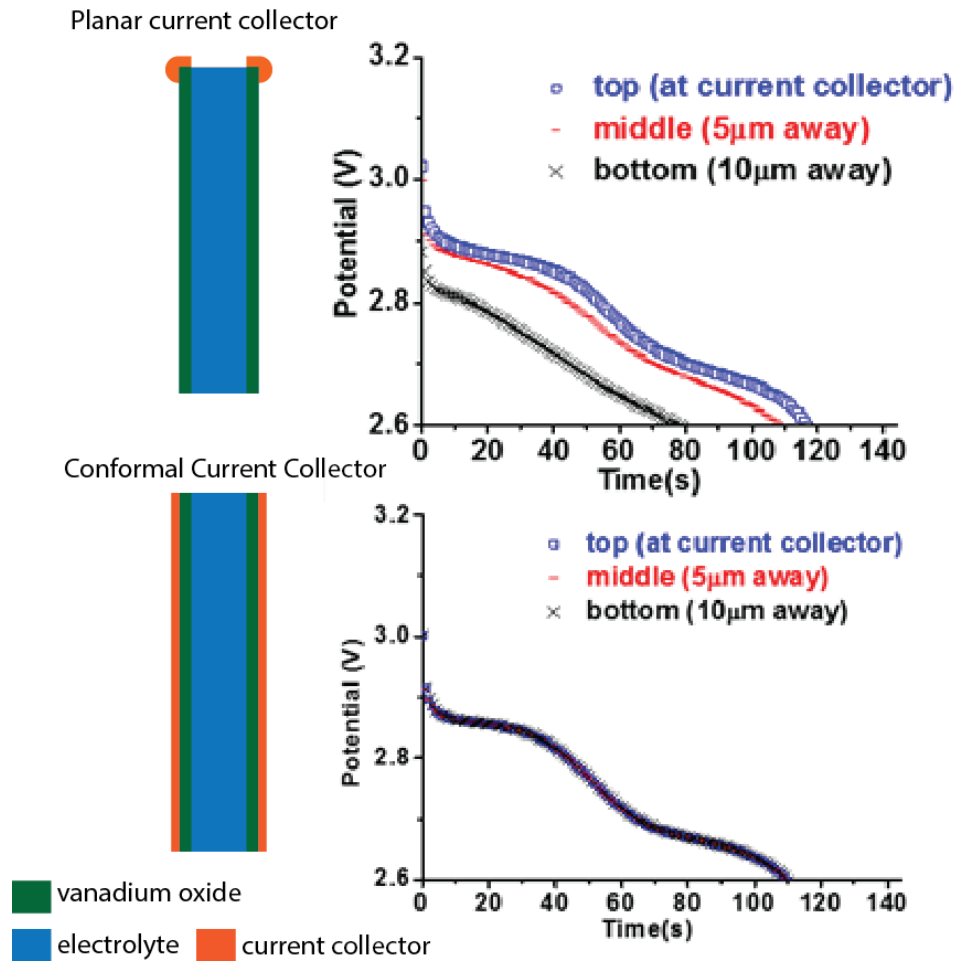


Figure 4-7: Schematic representations of the two current collector configurations, and their corresponding voltage profiles during 25C discharge as calculated by COMSOL

The differences between the two current collector configurations are immediately apparent. The nanotube with the planar current collector discharges at dramatically

different rates over the length of the nanotube, while the conformal current collector discharges uniformly. Interestingly, the capacity loss over the closest 5 μ m and furthest 5 μ m segments are different, suggesting that more than a simple Ohmic loss is causing capacity loss in the planar current collector case. The origin of capacity loss and reaction kinetics in these systems will be explored in greater detail in Chapter 5.

The conformal current collector case also serves to highlight the limitations of COMSOL for modeling nanostructures. While the planar current collector models are within 10% of the experimental results, up to 100C, the conformal current collector models significantly underestimate the rate performance of the experimental system, predicting only half of the retained capacity at 100C. The full predicted and measured data can be seen in Figure 4-8.

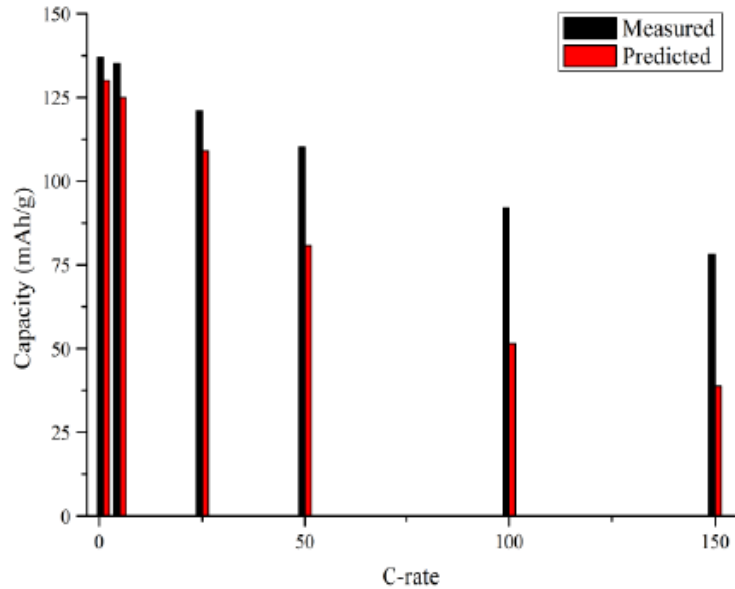


Figure 4-8: Predicted and measured capacity for the conformal current collector case

This consistent underestimation seems to indicate a systematic failure in the model system to capture a fast kinetics component to the charge storage mechanism. Given the high surface area interface between a very thin (<10nm) layer of Ru metal and the 23nm layer of V₂O₅, it seems possible that there are electronic effects which improve electron transport, or otherwise contribute charge storage. Where nanoscale effects begin to dominate device performance, finite element analysis is no longer effective. As a result, no further modeling was carried out on this particular electrode configuration.

4.4 Conclusion

COMSOL Multiphysics was validated using V₂O₅ electrodes as reference points. The software was able to predict the rate performance of the planar current collector electrode configuration up to very high rate, while its predictive value in the conformal current collector case was limited to the low rates. Additionally, the models are able to provide some insight into inhomogeneous charging in the planar current collector electrode configuration, indicating that the extreme end of the nanotube stored 1/3 less charge than the region nearest the current collector.

Chapter 5: Nanotube length and rate performance

5.1 Introduction

High aspect ratio nanostructures for battery electrodes have been of broad interest for improved energy and power density, because of the possibility of significant increases in mass loading and surface area without dramatic increase in device footprint.^{126,127}

Given the limited conductivity of most active intercalation materials, the most successful high aspect ratio nanostructures are hybrid structures which include some sort of integrated current collector.^{40,42,128} While these additional materials help to optimize performance, it can be an expensive solution which adds weight and volume to the electrode. There is no strong data to provide information about the limitations of extending nanotube length to increase charge storage, and how different charge storage mechanisms may be impacted differently.

Resistance and inhomogeneous reaction rates caused by voltage drops are very important to the power performance of an electrode. While Ohm's law gives an initial indication as to the magnitude of voltage or current density loss as a function of resistance, there are two additional mechanisms to consider which will impact power performance. These two mechanisms are called "polarizations" for their contribution to cell voltage drop, shown in Eq 5-1, where E is the thermodynamically predicted cell potential and V is the actual cell potential.¹²⁹

$$V = E - iR - \sum \eta_a - \sum \eta_c \quad \text{Eq. 5-1}$$

The Tafel polarization (η_a), also known as the activation polarization, is related to the dependence of reaction kinetics on over potential. The Tafel polarization is especially important, because unlike Ohm's law, an electrochemical reaction current does not scale

linearly with voltage.¹³⁰ Second is the concentration polarization (η_c), related to local electrolyte concentration depletion during electrochemical reactions.¹²⁹

These additional potential losses make it clear why understanding the impact of resistance in high aspect ratio nanostructures is not as simple as defining resistance in Ohm's law, and is at the heart of why predicting performance of an electrochemical system can be challenging. No clear characterization of the performance penalty for increasing aspect ratio in these high aspect ratio nanostructures has been developed to assist in the design and optimization of structures, especially given that the three different charge storage mechanisms; double layer capacitance, pseudocapacitance (Faradaic surface reactions) and insertion reactions may all respond differently to changes in overpotential.

The only previous report on the impact of aspect ratio on electrode performance utilizes a slurry packing method to fabricate the electrodes.¹³¹ Therefore there is no way to deconvolute the impact of the resistance related to the nanowire contact to the current collector, contact to adjacent nanowires or carbon particles, and resistance related to ionic conductivity. In order to isolate the electronic effects due to the structure of the material alone, a rational electrode design is required.

Here, we take advantage of the vertically aligned pores in anodized aluminum oxide templates to create electrodes with controllable geometry for examining the rate limitations in nanotube electrodes with variable aspect ratio. Very thin active material facilitates fast reaction kinetics, where no portion of the active material is more than ~20nm from the electrode/electrolyte interface. Therefore, the rate limiting step is

expected to be the electron conductivity rather than ion availability. This system will allow a systematic variation of the length of the electrode which should only alter the electron conductivity in the structure, allowing a systematic analysis of the impact of conductivity on electrode performance, decoupled from other factors. In particular, the impact of conductivity on the kinetics of the electrochemical reactions will be highlighted.

5.2 Methods and Materials

Anodized aluminum oxide templates were fabricated by a two-step anodization process which has been widely reported.⁵⁸ Briefly, Al sheets were electropolished for 5 min at 15V in a 1:5 mixture of perchloric acid and ethanol held at 3°C. The sheets were then anodized for 5 hr at 40 V in 0.3 M oxalic acid at 8°C. The anodized aluminum was removed in chromic/phosphoric at 38°C for 3 hr and 20 min. The Al was then anodized again, at 40 V in 0.3M oxalic acid at 8 °C. During the second anodization, the time was varied to produce various lengths of template. Pore widening took place in 5% H₃PO₄ at 38 °C for 11.5 min.

V₂O₅ was deposited by atomic layer deposition in a Beneq ALD reactor with VTOP and O₃ as the precursor and oxidant, respectively. A 2 s VTOP pulse followed by a 3 s O₃ pulse was repeated 300 times to achieve the active films of ~20 nm in thickness, measured by ellipsometry on planar substrates. Additional details regarding the ALD process have been detailed elsewhere.¹¹⁶

Cyclic voltammetry is carried out on a Biologic VSP Potentiostat. All electrodes are tested in 3 electrode cells with 1/2" diameter Li foil discs as the reference and counter electrodes. The electrolyte is 1M LiClO₄ in propylene carbonate, prepared from dry

materials inside an argon filled glove box. Electrodes are sputtered with a thin layer of gold, connected to stainless steel mounts by copper tape, then sealed in Parafilm windows with diameters of 5/8". Figure 5-1 shows a schematic of the electrodes mounted and sealed.

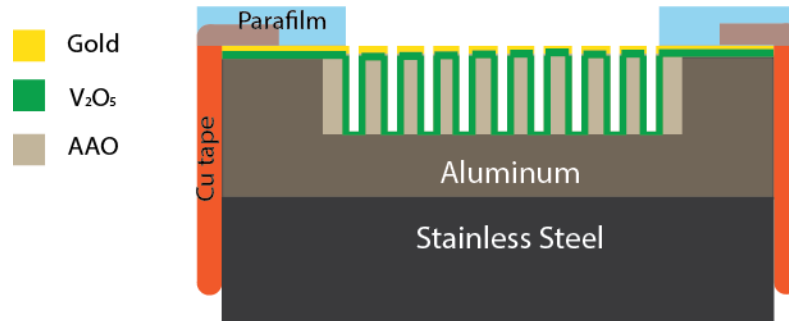


Figure 5-1: Schematic of electrode preparation

Material characterization was carried out on a Hitachi SU-70 SEM, and pore lengths were determined from the SEM images using the measurement tool in Adobe Photoshop.

Electrode masses before and after ALD are measured by microbalance, with an accuracy $\pm 1\mu\text{g}$.

To help understand the expected losses due to conductivity issues, a finite element model was developed to predict the behavior of nanostructured V₂O₅ half cells. The lithium ion battery module available in COMSOL Multiphysics™ was used to perform these simulations. Each simulation evaluated a single pore, with an electrolyte reservoir providing a surplus of available lithium. The models use a pore with a fixed radius of 50nm, and pore length is varied from 500 nm up to 4 μm in steps of 500 nm. The active material occupies the outer 20 nm of the pore length, and has a conductivity of 0.005 S m^{-1} and a lithium diffusion constant of $3 \times 10^{-17} \text{ m}^2\text{s}^{-1}$. Built in parameters for 1 M LiPF₆

EC/DEC electrolyte are used for the electrolyte conductivity, lithium transport number, and diffusion coefficient. The material potential is calculated as a function of the lithium concentration in the active material, as determined by the current-voltage relationship in a planar V_2O_5 film at a very slow rate. Only galvanostatic discharge is modeled for this study, so the initial conditions assume 4.0 V on the cathode, with only 1 mM Li present in the active material. As current is applied, the electrode potential changes as a function of inserted lithium concentration, based on a discharge curve measured at a $C/3$ rate for a planar V_2O_5 electrode fabricated by ALD on a stainless steel disc. Discharge time is defined as the time required for the average potential on the electrode to drop to 2.60 V. To simulate discharge, total current is calculated from the mass and the theoretical capacity, and is applied along the bottom boundary of the material.

5.3 Results and Discussion

First, the dimensions of the AAO electrodes need to be determined. The length of the pore is roughly linear with anodization time, as seen in the electrodes shown in Figure 5-2, which show growth times of 900s, 2250s and 3600s respectively. Each of these structures has V_2O_5 deposited by ALD and a small layer of Au coated on the surface. The diameters of the pores are quite similar, as expected from the combination of ordered AAO growth and controlled ALD material deposition. The SEM images show the V_2O_5 coating has some surface roughness, which can be attributed to non-ideal ALD growth during the V_2O_5 deposition process.

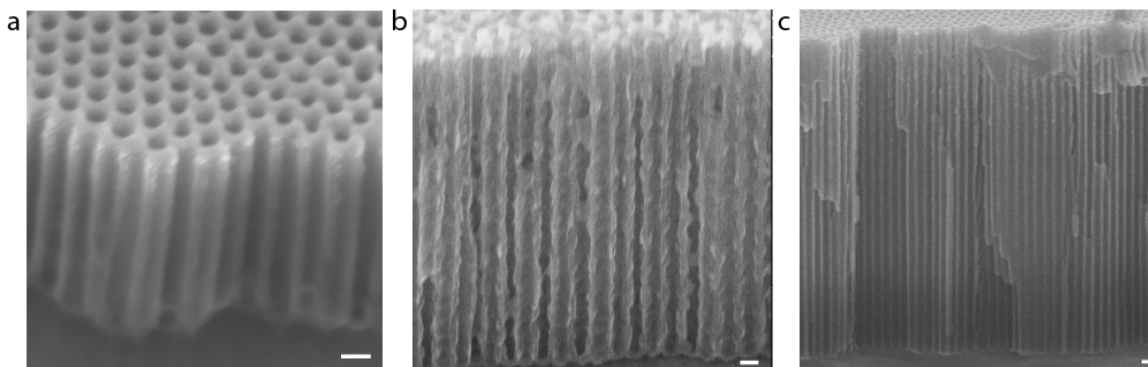


Figure 5-2: SEM images of AAO templates grown for (a) 900s (b) 2250s and (c) 3600s. All scale bars are 100nm

Length varies with growth time, and a complete calibration curve of length versus growth time is shown in Figure 5-3. The relationship between growth time and length is linear and predictable, which is critically important for fabricating electrodes with controlled structures. The mass loading of V_2O_5 as a function of growth time is also linear, suggesting that no significant tapering or thinning of the V_2O_5 coating is occurring in these high aspect ratio structures. Additionally, gold is sputtered on the tops of the electrodes, to improve conductivity, but the pores remain open despite this coating.

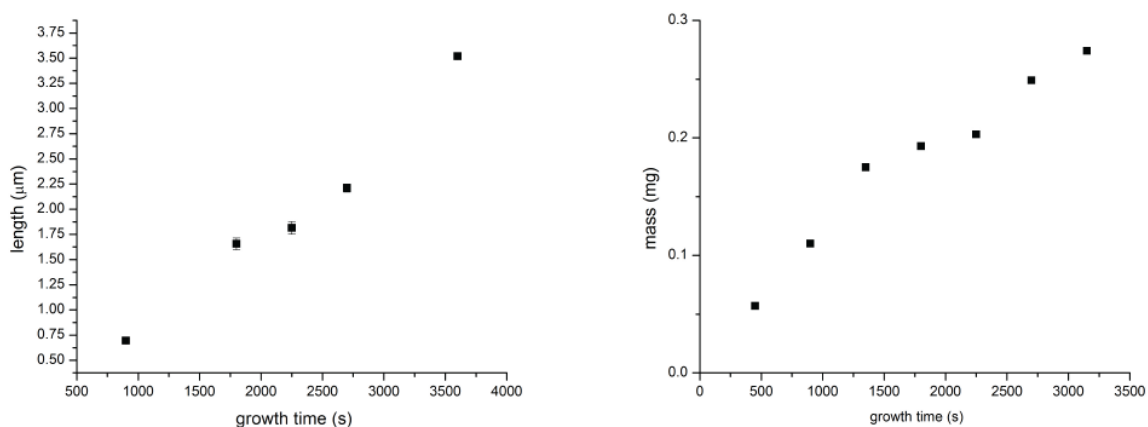


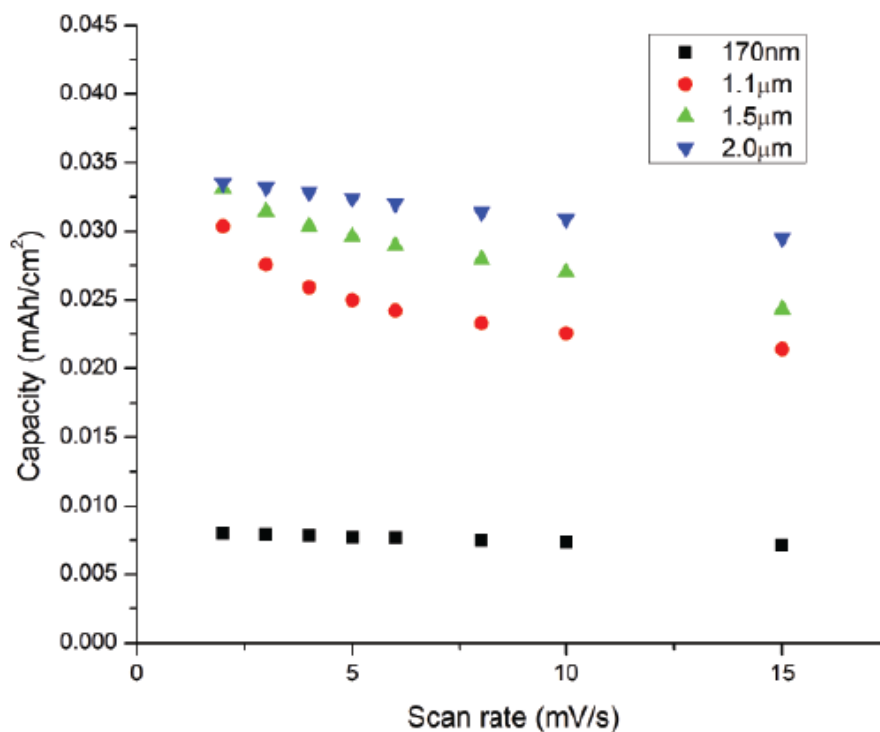
Figure 5-3: Length (left) and mass (right) increase with increasing AAO growth time

Electrochemical performance of these electrodes is tested by cyclic voltammetry in 3 electrode cells vs. Li. As expected, the areal capacitance increases as a function of pore length for all scan rates, as seen in Figure 5-4a. This increase is linear or close to linear at most scan rates, as can be seen in Figure 5-4b and 5-4c, for 5 mV/s and 15 mV/s respectively.

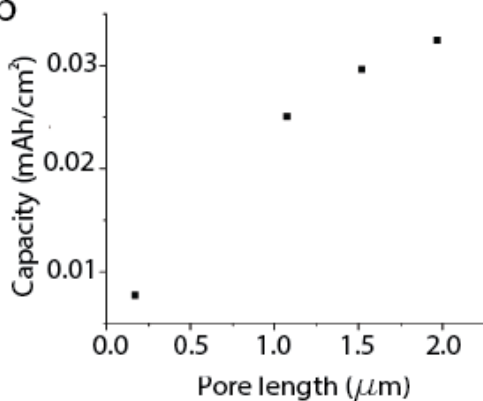
However, the increase in capacity is not 1:1 with the increase in length. While the surface area and the mass loading increase linearly with the length increase, resistance is also increasing resulting in an inhomogeneous utilization of the material. How this increasing resistance impacts the insertion of Li versus fast surface redox reaction and double layer charge storage may give some clues into why the trends are somewhat different at low, medium and fast scan rates.

Different trends at different rates suggest that there are different charge storage mechanisms which dominate at high and low rates and which respond to polarization differently. Two distinct kinetics, charge stored by fast surface kinetics and slower diffusion limited charge storage must be separated. The current contributed by fast surface reactions, whether double layer charging or surface redox reactions, generally scales linearly to the scan rate, while diffusion limited reactions will respond linearly to the square root of the scan rate. Two different methods are employed to separate the surface charge from the bulk charge using cyclic voltammetry (CV) data for a variety of scan rates (v).

a



b



c

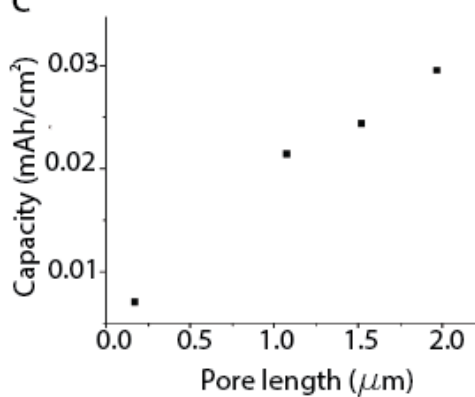


Figure 5-4: (a) capacity for four different lengths over increasing scan rates. Capacity as a function of nanotube length at (b) 5 mV/s and (c) 15 mV/s

The first method was developed by Trasatti.¹⁰³ This method extrapolates the charge passed during a series of CVs to the limit of $v=\infty$, where it can be assumed that only the fast surface charging is contributing to charge storage. Extrapolating the same charge data to $v=0$ provides the theoretical total charge, and the difference between the

total and the surface charge provides the bulk charge. Details regarding how this data is extracted from the CV results can be found in Appendix B.

The second method is known as Dunn's method.¹³² This method relies on the assumption that the current measured at any given potential during a CV is the sum of a surface and a bulk component (Eq. 5-2).

$$i(V)=k_1v+k_2v^{1/2} \quad \text{Eq. 5-2}$$

In order to separate the surface and bulk components, k_1 and k_2 are needed for any given potential V . These constants can be calculated easily from the current at a variety of scan rates by rearranging Eq5-2 to Eq 5-3.

$$i(V)/v^{1/2}=k_1v^{1/2}+k_2 \quad \text{Eq. 5-3}$$

This equation is in a linear form that so k_1 and k_2 can be determined from the slope and intercept, respectively, of a linear fit of the data. Details of this data processing are also available in Appendix B.

Figure 5-5 shows the $v^{1/2}$ -dependent, or diffusion limited charge calculated by the two methods discussed previously. Because Trasatti's method extrapolates to a limit, it is not unusual that it is somewhat higher than the Dunn's method estimates. Dunn's method predicts the same surface charge for each scan rate (because of the linear relationship) but does not predict the same bulk charge at each scan rate, so 5 mV/s and 15 mV/s are shown here, in green and blue respectively.

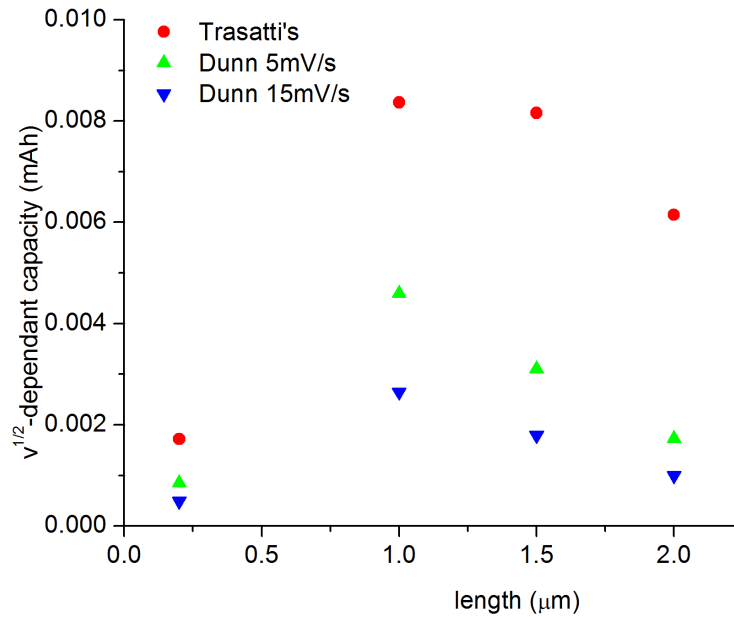


Figure 5-5: Diffusion limited ($v^{1/2}$ dependent) charge calculated by Dunn and Trasatti's methods

The trend is quite similar to that predicted by Trasatti's method, and indicates that diffusion limited charge increased with length initially, but then is stabilized, or decreased as the length of the nanotube increases. This trend makes sense for a Faradaic reaction mechanism, where current decreases logarithmically as the potential approaches the equilibrium potential, below which no reaction will take place. Based on these results, by the time the nanotube lengths are beyond $1\mu\text{m}$ the polarization is sufficient to be preventing full reaction of additional material.

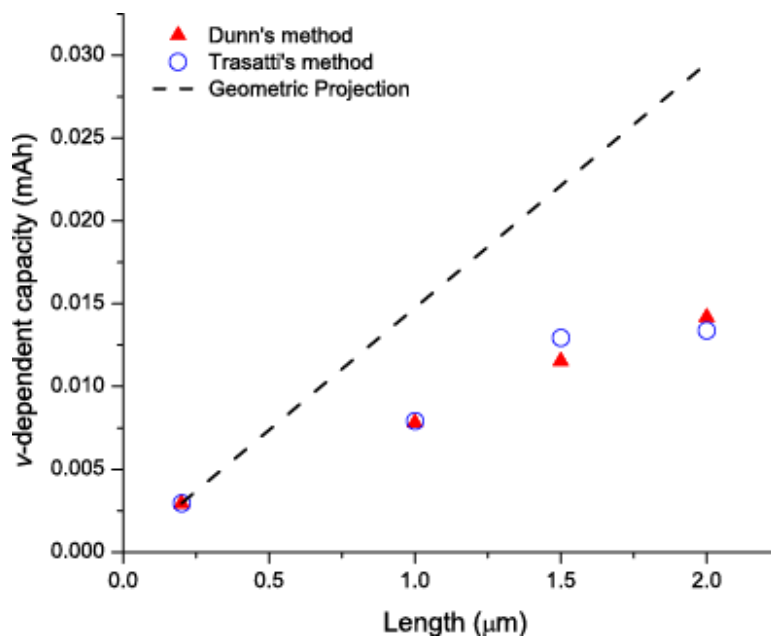


Figure 5-6: Scan rate dependent charge calculated by Dunn and Trasatti's methods

The v-dependent, fast surface charge calculated by Dunn's and Trasatti's methods is shown in Figure 5-6, along with a linear geometric estimate of the maximum possible capacity based on surface area increase. Both Dunn and Trasatti's methods extrapolate very similar surface charge values for each electrode length, and both show a fairly linear increase in surface charge with increasing length. However, the surface charge does not increase geometrically with the surface area of the nanotubes. This observation is consistent with inhomogeneous charging preventing full utilization the entire surface of these structures. The linear response suggests that the surface reactions are not governed by the Tafel or Butler-Volmer equations, with their exponential relationship between current and overpotential. Instead, this charge is mostly capacitive, where current scales linearly to voltage.

To explore the potential gradients and their influence on lithiation, a computational model was used to estimate the performance of nanotube electrodes with

variable lengths. The model geometry is a single nanowire, to keep computational demands low. Therefore, in order to compare the modeling data with the real electrode data, each point is normalized to the capacity of the shortest sample. In this way, a 1:1 increase of normalized capacity vs normalized length is the ideal case, denoted by the dotted line in Figure 5-7. The experimental and calculated values are also plotted in black and red, respectively. These models include only the redox reactions, and neglect any capacitive components, so the difference between measured and calculated capacity will include any capacitive components as well as any ohmic resistance enhanced by surface scattering. The fact that the calculated values are greater than the experimental values suggests that losses due to increases resistance outweigh any advantages from the capacitive charge storage. This observation suggests that minimizing defects and scattering sites may be a more important strategy for improving nanostructured electrode performance than simply increasing the surface area.

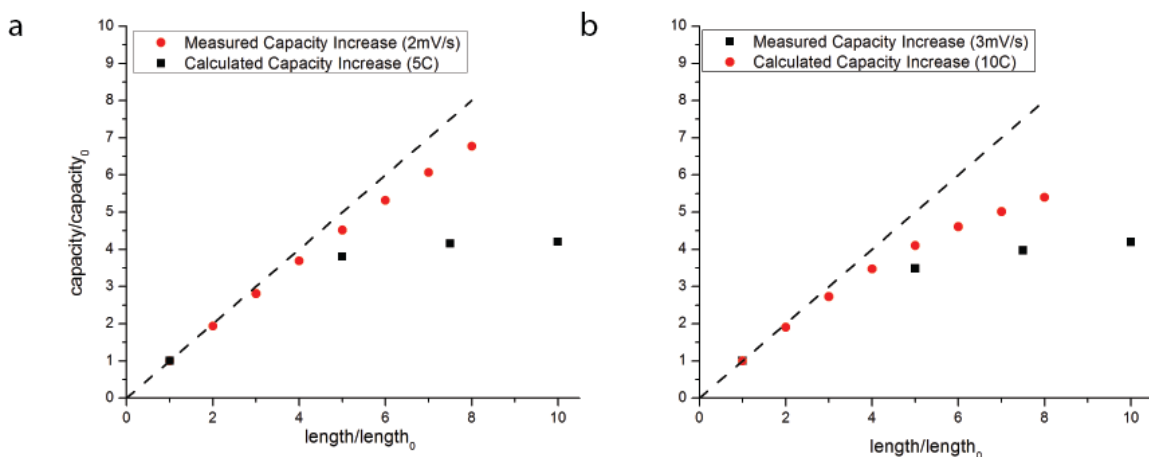


Figure 5-7: Measured capacity and calculated capacity for two different rates

The predicted voltage difference and state of charge (soc) difference between the top and the bottom of the electrode as a function of length are shown in Figures 5-8a and 5-8b, respectively. While the overall differences are small, averaged over the length of the entire nanotube, over billions of nanotubes per square centimeter, it becomes clear why the electrodes cannot maintain a steady performance improvement as their length increases.

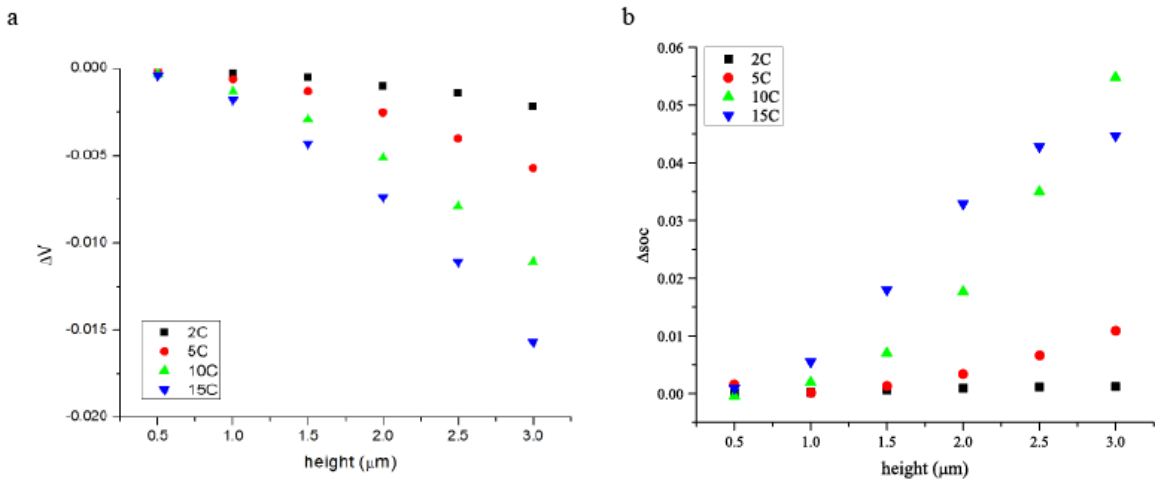


Figure 5-8: Calculated (a) voltage difference and (b) state of charge difference across the length of a nanotube

The modeling cannot capture scattering or other size effects, so these voltage drops are undoubtedly underestimating the real voltage drops. However, it is useful to see even the idealized impact of these relatively small voltage drops, which can be seen in the variation in state of charge across the length of the each nanotube. At the highest rates, the soc variation is as much as 5 %, indicating the material utilization at the nanotube tip lags behind the base by at least 5 %, even over only 3 μm. These modeling results provide a working estimate for how much capacity is being sacrificed by extending the length of the nanotube, or by increasing the rate.

5.4 Conclusion:

If nanostructured electrode arrays are going to solve energy and power density problems for lithium ion battery cathodes, careful attention should be paid to electrode geometry to maximize the utilization of active material while also maximizing electron access. Here we show the dramatic impact of increasing aspect ratio which is dependent on reaction mechanism, and which results in inhomogeneous state of charge even over a few microns in length. These data explain why integrated current collectors for lithium ion batteries have achieved such remarkable increases in performance, even for materials which do not have extreme aspect ratios.

Chapter 6: 3D cross linked vanadium oxide cathodes as a testbed for understanding tortuosity and inhomogeneity.

6.1 Introduction

Lithium ion batteries are a critical component of modern technology, from portable devices like laptops and cell phones to electric vehicles. Nanostructured electrodes have been of great interest for their potential to improve power performance of Li ion batteries, but characterization of individual nanostructures alone is insufficient to provide a complete understanding of the performance limitations within an electrode.³⁶ A variety of mesoscale issues, which bridge the scale between individual structures and whole electrodes, can impact reaction kinetics and rate performance. The relationship between individual particles and full electrodes has been fairly well investigated in conventional electrodes, but largely neglected in nanostructured electrodes, particular ones which feature high aspect ratio nanowires or nanotubes rather than particles.

Arrays of nanowires or nanotubes provide an excellent opportunity to exploit this anisotropic tortuosity to maintain excellent ion transport through the thickness of an electrode. However, as demonstrated in previous chapters, the length of the nanotubes or nanowires cannot be indefinitely extended to increase mass loading. Instead, structures are needed which can maintain the excellent ion pathways of aligned nanotube and nanowire arrays, while also increasing mass loading. Introducing crosslinking layers in the plane of the electrode, perpendicular to ion channels penetrating the electrode, may be able to provide an increase in mass loading without a significant penalty for increasing tortuosity. Aligned arrays and a proposed interlinked structure, showing the insertion of additional material in the plane of the electrode is shown in Figure 6-1. To the best of our knowledge, no electrodes have been demonstrated with this design.

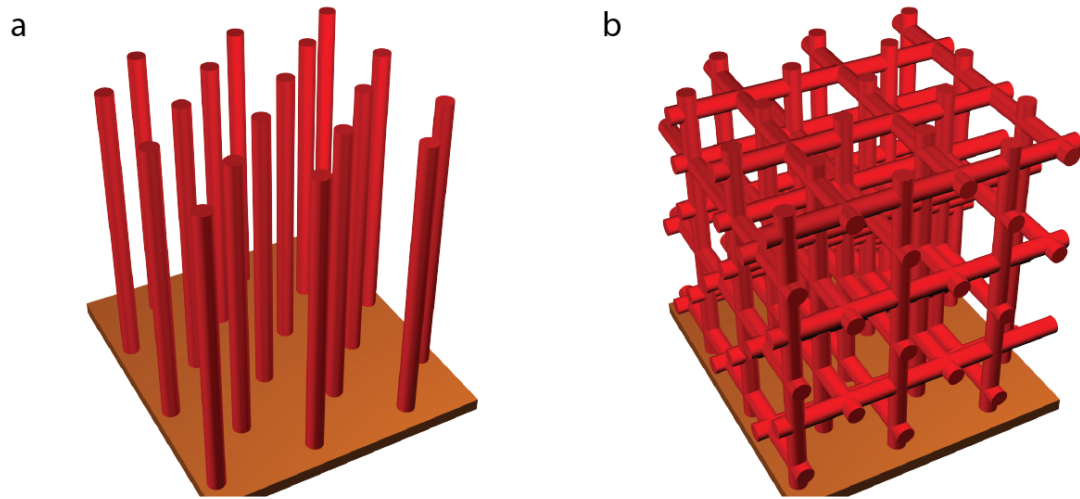


Figure 6-1: (a) 1D arrays of aligned nanowires (b) crosslinked nanowires with interconnections in the plane of the electrode

However, the introduction of defects to increase mass loading, structural stability or ion access leads to inhomogeneity within an electrode. Inhomogeneity in these structures which impacts electrical connections or Li transport has been identified as the cause of rate limitations as well as degradation and failure mechanisms in conventional Li ion battery systems.³¹ Understanding the tolerance for defects in advanced architectures is an important step to move forward with electrode designs which can exhibit good energy and power performance while retaining cyclability.

Anodized aluminum oxide provides opportunities to create a variety of 3D structures over a wide range of sizes, while retaining the same surface chemistry to facilitate active material deposition. Traditional AAO can be used to create electrodes with vertical alignment and a tortuosity of 1 through the plane of the electrode.^{59,133} These electrodes do not require polymer binder or conductive carbon additives, and so the local and mesoscale architectures are very well defined, and can be used to create very high performance batteries, with optimized structures.⁴² However, mass loading in

these structures is generally low, and strategies for improving the mass loading inevitably move towards disordered systems like CNT sponges.¹³⁴ While many disordered systems also have excellent electrochemical performance, there is not a clear understanding of the trade-offs between ordered and disordered systems, because of the challenges in directly comparing distinct systems. AAO is a template material which does allow for morphology modification, without changes in the surface chemistry that would impact the deposition of active materials. We have demonstrated a method for creating 3D anodized aluminum oxide structures which allows us to disrupt the ordered growth of the pores in distinct regions while retaining pore ordering in other sections of the structure, creating layers of connecting crosslinkers between aligned pores.⁷⁷ This pore modification technique can be repeated as often as desired, while the ordered growth time can be adjusted to maintain the overall thickness of the template. Here we use these templates to fabricate V_2O_5 cathodes with variable alignment, and examine their rate performance. This strategy allows direct comparison of the same material, under the same experimental conditions, with only alterations to the electrolyte pathways and the alignment of the electrode to account for performance differences.

6.2 Methods and Materials

The method for producing branches in anodized aluminum oxide is described in detail elsewhere.⁷⁷ Briefly, traditional two step anodizations are utilized. During the second anodization, pore branching is induced by modifying the anodization voltage from 40 V to 20 V to 40 V in 2 V/30 s steps. Total time at 40 V is modulated to result in AAO structures which are close to uniform in total thickness, (between 1.5 and 2.0 μm), with

the branches evenly spaced. Pore widening is carried out in 5% H₃PO₄ at 38° C for 11.5 min.

Atomic layer deposition is used to deposit V₂O₅ conformally onto the AAO templates. The ALD method is discussed in detail elsewhere.¹¹⁶ Briefly, 2 s of VTOP precursor and 3 s O₃ oxidant are alternately pulsed in a commercial Beneq ALD reactor for 300 cycles at 170 °C. The resulting films are ~20 nm thick.

A Hitachi SU-70 scanning electron microscope (SEM) was used to characterize the structure of the AAO/V₂O₅ templates, while a Bruker D8 Advance system with LynxEye PSD detector and Ni β-filter using CuKα radiation (step size 0.02° in the range of 14° <2θ <55°) was used to characterize the material by X-ray diffraction (XRD).

Electrochemical testing was carried out in custom built three electrode cells which were loaded and sealed in an Ar filled glovebox, and removed for testing. Each cell had a ½ inch diameter disc of Li foil for the counter and reference electrodes, while the electrodes were masked to ¼ inch diameter. The electrolyte was 1M LiClO₄ in propylene carbonate, and testing was carried out on a Biologic VSP potentiostat.

6.3 Results and Discussion

Four different electrodes were tested, varying from conventional, straight pores to pores with three branches. SEM images of these four different anodized aluminum oxide templates can be seen in Figure 6-2, with ~20 nm of V₂O₅ deposited by ALD. The V₂O₅ coating is what gives the pores their roughened surfaces, while the branched regions can be seen as a discontinuity in the AAO template. However, the main channels

remain largely aligned before and after each branched region, and overall, the tortuosity of these structures does not appear to be significantly different.

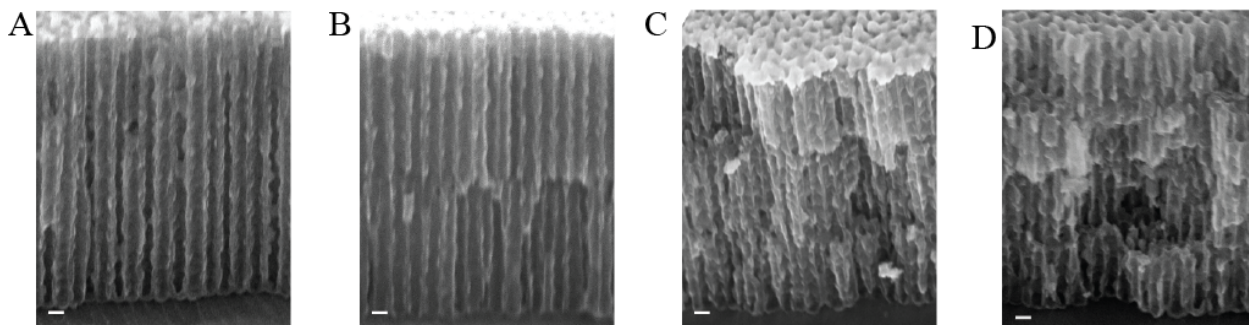


Figure 6-2: Electrodes fabricated from 4 different AAO sample structures (a) straight (b) one branch (c) two branch (d) three branch

The branched regions are roughly evenly spaced, and occupy ~ 100 nm of thickness within ~ 1750 nm total length of the structure. The average length of each of these structures, along with each structure's average V_2O_5 mass loading, is shown in Figure 6-3. While the length of the electrodes is held mostly consistent, the mass loading increases slightly with each additional branch. This suggests that additional surface area is available for V_2O_5 deposition, without a dramatic increase in total electrode volume. In this way, the mass loading and surface area are increased without a dramatic increase in the tortuosity of the electrode.

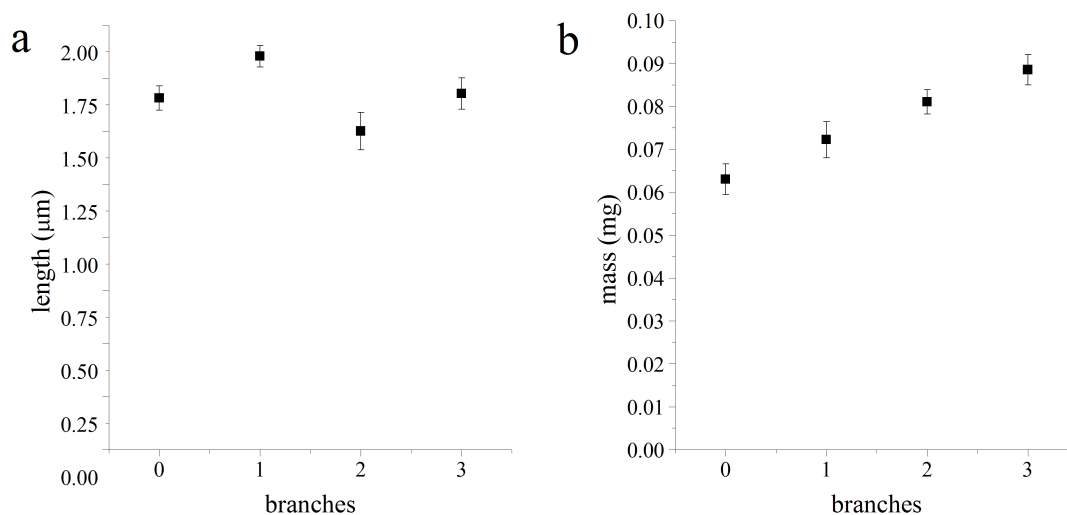


Figure 6-3: Length, measured from SEM images and mass of V_2O_5 , measured by microbalance, for the four different configurations of electrode

Error bars in each portion of Figure 6-3 denote standard deviations in the respective measurements repeated over at least three samples. The surprisingly large standard deviations for the length measurements in particular suggest that the branching of the pores modifies the growth rate of the AAO more extensively than originally suspected. With each additional branched region added, 900s of ordered growth time is removed from the protocol to account for the additional growth. Regardless, the linear mass increase as a function of inserted branches suggests that the surface area is increased consistently, even as the total template length is not increased. Overall, the length and mass loading changes are relatively minor as well, which suggest that the electrodes are mostly similar in dimensions, and only vary in shape.

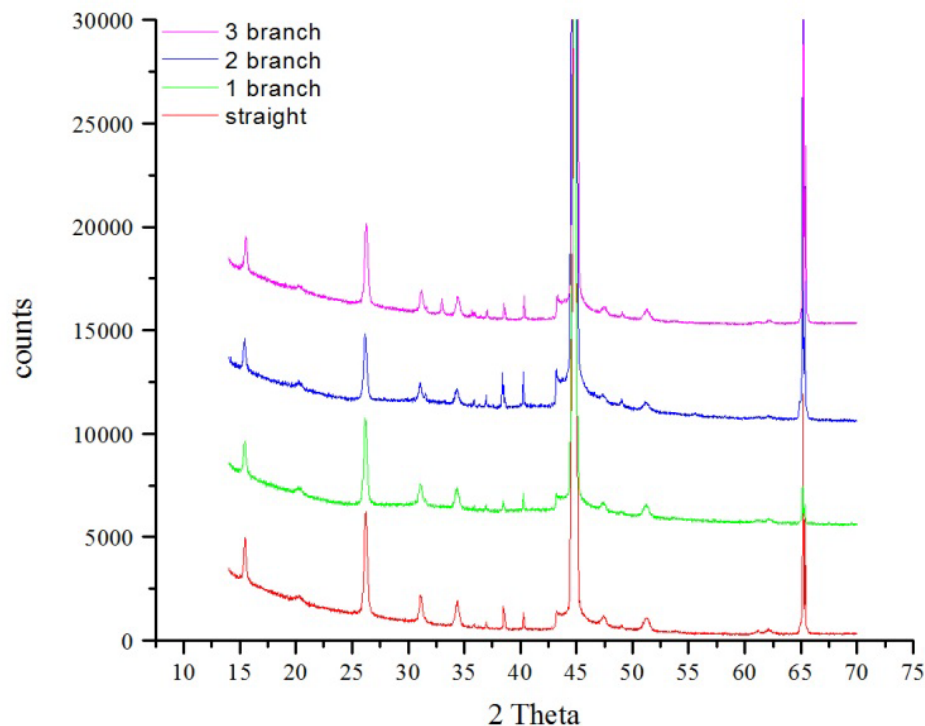


Figure 6-4: XRD patterns for the four different structures of V₂O₅ AAO electrodes

XRD was carried out to confirm that there were no significant differences in the V₂O₅ structure as deposited within the various templates. The patterns for the four different structures can be seen in Figure 6-4. The underlying Al produces the very intense peak at 2 θ of 45°, along with additional features between 35° and 45° attributable to the Al. No peaks corresponding to Al₂O₃ are observed. This is consistent with numerous literature observations that most anodized aluminum oxides are amorphous.¹³⁵ V₂O₅ deposited by this ALD technique had been previously identified as α-V₂O₅, as can be seen here.¹¹⁵ Most importantly, the V₂O₅ retains its crystallinity in each different structure. Any differences observed in the electrochemistry should not be attributable to differences in crystal structure or crystalline alignment within these structures.

Structurally, the only major differences between these 4 electrodes should be the ion pathways available, interconnecting adjacent pores and disrupting the ideal alignment of the unbranched AAO. If improved ion access is the critical determinant of power performance in these structures, rate performance improvement should be observed as the branching increases. However, if the inhomogeneity in the structure causes incomplete charging and discharging or causes other degradation, the straight pores should outperform the branched structures at higher rates.

: Cyclic voltammetry was carried out for all four electrode structures in 3 electrode cells, vs. Li foil. CVs from 20mV/s to 2mV/s are shown in Figure 6-5. Two clear insertion/deinsertion peaks are clearly visible in all samples, even at the highest scan rate, indicating that lithium insertion is still taking place even at the highest scan rates.

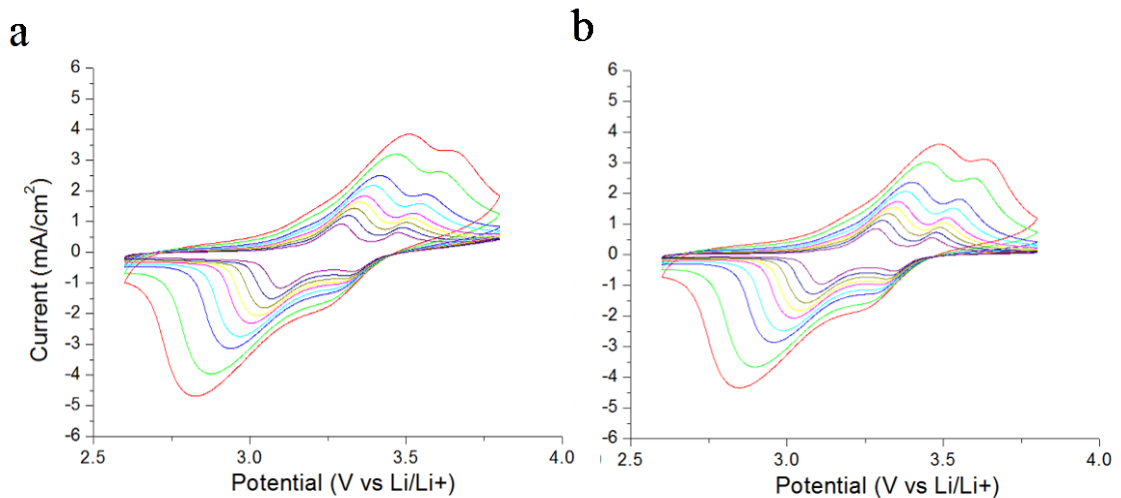


Figure 6-5: CVs from 20mV/s to 2mV/s for (a) straight, (b) three branch electrodes

Galvanostatic charging and discharging were measured for the two extreme cases; the straight pores and the 3 branched structures. The results are shown in Figure 6-6. While at lower rates the capacities are fairly similar, the capacity is retained better at high rates for the highly branched structure. While 2C is actually quite high for many battery materials, given the very thin active material and relatively good conductivity of V_2O_5 , it is not surprising that the electrodes are nearly indistinguishable at that rate. As the rate increases to 50C, the straight electrode retains 48% of its 2C capacity, while the branched electrode retains 76% percent of its 2C capacity. This excellent capacity retention for any insertion electrode, suggests that the structural differences between the straight pore and the branched pore result in significant differences in reaction kinetics.

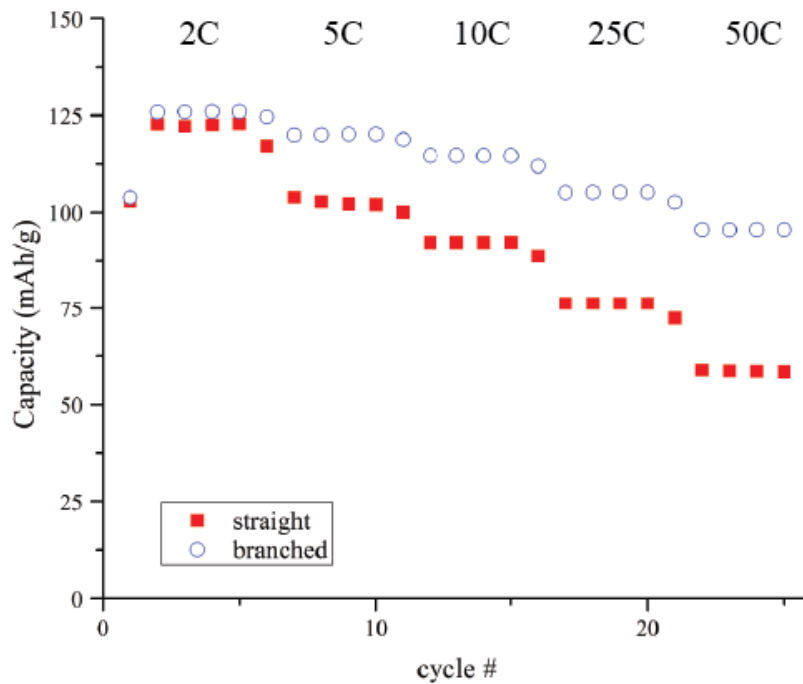


Figure 6-6: Capacity measured by galvanostatic voltammetry for the straight and 3 branched electrodes

To examine the relationship between structure and kinetics, Trasatti's method was used to deconvolute fast surface charging from slower, diffusion limited charge storage, as discussed in previous sections. The difference between the calculated surface charge for the straight and 3 branched electrodes is shown in Table 6-1.

	Surface (mAh/g)	Bulk (mAh/g)	Surface %
Straight	56.35	37.17	60%
3 branches	89.73	51.03	64%

Table 6-1: Charge deconvolution for the straight and 3 branched electrodes

The increase in surface area normalized by mass loading suggests an explanation for the dramatic improvement facilitated by the introduction of the branches. Additional mass is loaded without an increase in active material thickness, resulting in additional surface area available for fast charging and discharging, which may account for the improved rate performance. Additionally, since the branched regions open up additional space within the AAO template that had previously been occupied by inert Al_2O_3 , there is no loss of electrolyte volume or ionic access to limit the utilization of the added material. The additional local electrolyte volume may also provide improved rate performance by providing additional local Li^+ which are available for reaction without needing to be transported through the thickness of the electrode. Additionally, despite the introduction of defects and tortuosity, the direct pathways through the thickness of the electrode are maintained in the cross-linked structures. The controlled introduction of defects into the plane of the electrode, which provide additional mass, surface area and electrolyte volume while maintaining low through-plane tortuosity, demonstrates the utility of

controllable, anisotropic tortuosity in battery electrodes for maximizing mass loading and rate performance.

In order to investigate the consequences of the pore crosslinking on defects and degradation, long term cycling was carried out for straight and 3 branched structures at 10C. The discharge capacity for each structure is shown over 500 cycles in Figure 6-7. Despite the high rate of cycling, both structures retain more than 90% of their initial capacity. Additionally, the two structures do not have significantly different losses in capacity during cycling, suggesting that the introduction of defects through branching is not rapidly accelerating degradation mechanisms with the V_2O_5 .

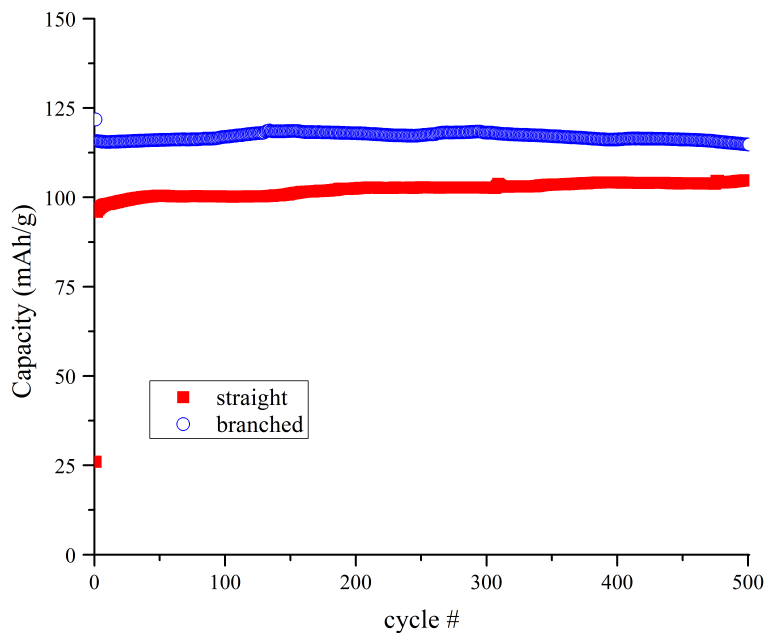


Figure 6-7: Capacity calculated by galvanostatic voltammetry for 500 cycles at a 10 C rate

6.4 Conclusions

Here, we have systematically compared vertically aligned nanotube electrodes with increasingly complex networks of interconnected nanotube passages. The branched structures show more reversible electrochemistry with better capacity retention at high rates. Additionally, the introduction of branches does not appear to limit the long term cycling performance of the electrodes, despite the introduction of defect sites to achieve the interconnected pore network which facilitates the fast ion access in the structures. Critically, here we demonstrate a strategy for improved mass loading which corresponds to improved rate performance, suggesting that increased tortuosity can be tolerated within electrodes as long as straight channels are maintained through the thickness of the electrode. These electrodes may provide a model for designing other types of structures with maximized capacity and rate capability.

Chapter 7: Summary and Outlook

7.1 Summary

In this dissertation, traditional 1D and modified crosslinked anodized aluminum oxide structures were used as templates to create controlled arrays of nanotubes as well as interconnected 3D mesostructures of V_2O_5 . These structures were used as model lithium ion battery cathodes to test the impact of structure on reaction kinetics and rate performance. First, the impact of aspect ratio on charge storage kinetics was explored. Diffusion limited Li-insertion was dramatically limited by aspect ratio, while fast surface charging continues to increase with increasing nanotube length. However, the surface charging also suffers from resistive losses, but at a different rate. Computational results showed the magnitude of the voltage drops across the nanotube lengths, and the corresponding state of charge changes, which can be as large as 5% over $3\mu\text{m}$ in length. Second, the impact of 3D structure on electrode performance was explored. The insertion of branched regions into the aligned AAO pores resulting in increased mass loading during ALD deposition, implying an increased surface area. This increased active material mass loading leads to an increase in capacity which is retained at higher rates than in the straight pores. The fast surface mechanism contributes an additional 33.38 mAh/g in the branched structure compared to the straight pores, as calculated by Trasatti's method. This result suggests that controlled architectures can maintain good ionic pathways with increased mass loading to improve electrode performance. Long term cycling also suggests that the introduction of defects does not limit the cycling stability of these electrodes, making this an appealing strategy for improving on 1D electrode arrays.

7.2 Outlook

This work highlights the value of carefully controlled electrodes which can be used to systematically explore the effect of structure on various energy storage mechanisms. Based on the results observed in these testbed electrodes, improved V_2O_5 electrodes can be designed based on rational expectations for the impact of surface area, active material length and disorder. These techniques should be portable to any other electrochemically active material which can be deposited and tested within AAO templates. For any material, optimized structures for the dominant mechanisms in the electrode can be designed.

Appendix A: Anodized Aluminum Oxide Methods

A-1: General guidelines for fabricating AAO templates:

Polycarbonate holders like the one shown below are used to mask a fixed area for anodizations. When sealing these types of holders, it is important that no electrolyte is leaking into the holder, but also that the aluminum is not being bent or distorted in any way. These holders are not used during electropolishing, and should generally be kept away from organic solvents, which will weaken and degrade the polymer over time. Large holders, like the one shown in the figure, are best for first anodizations. These large pieces can be cut into smaller pieces for the second anodization process.

Electrolyte temperature during the polishing or anodization process is maintained using a jacket beaker and vigorous stirring. Excessive condensation on the jacket beaker should be considered a red flag for heat and humidity conditions which are not ideal for anodization. In these cases especially, it is important to check the actual temperature of the electrolyte before turning on the voltage source, regardless of the temperature reading on the water recirculator.

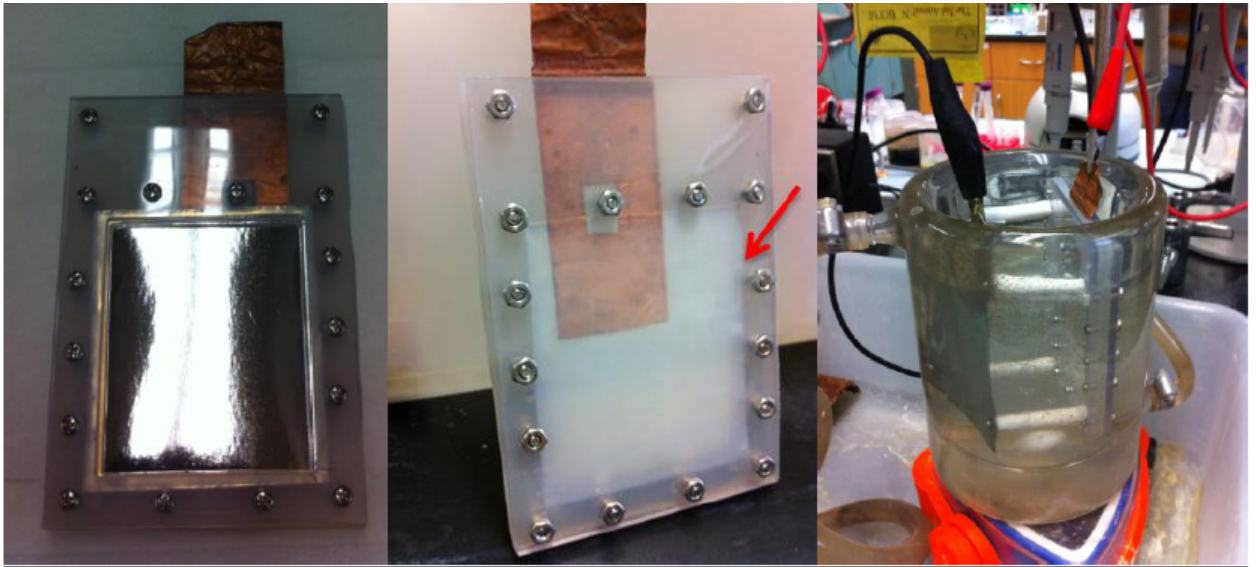


Figure A-1: Aluminum holders, front and back and the full cell set-up in a jacket beaker

A-2: Common defects and concerns related to homogeneity of the structures
Analysis of anodized aluminum oxide fabricated by the two step method has generally agreed that pore diameters and interpore distances are uniform within a tolerance of ~10%. However, large regions of defects can be observed where the aluminum was bent or scratched prior to anodization. Figure A2 depicts two regions of the same AAO template, where defects due to bends in the aluminum are visible. Despite

electropolishing removing any visible evidence of the damage to the aluminum, the grain structure of the aluminum was undoubtedly impacted, resulting in the effects visible on the right. Given the high surface area of the templates, and the small sampling areas of SEM, it is very important to keep samples clean and flat throughout the process, and to do extensive SEM imaging periodically to ensure that defects are not going unnoticed.

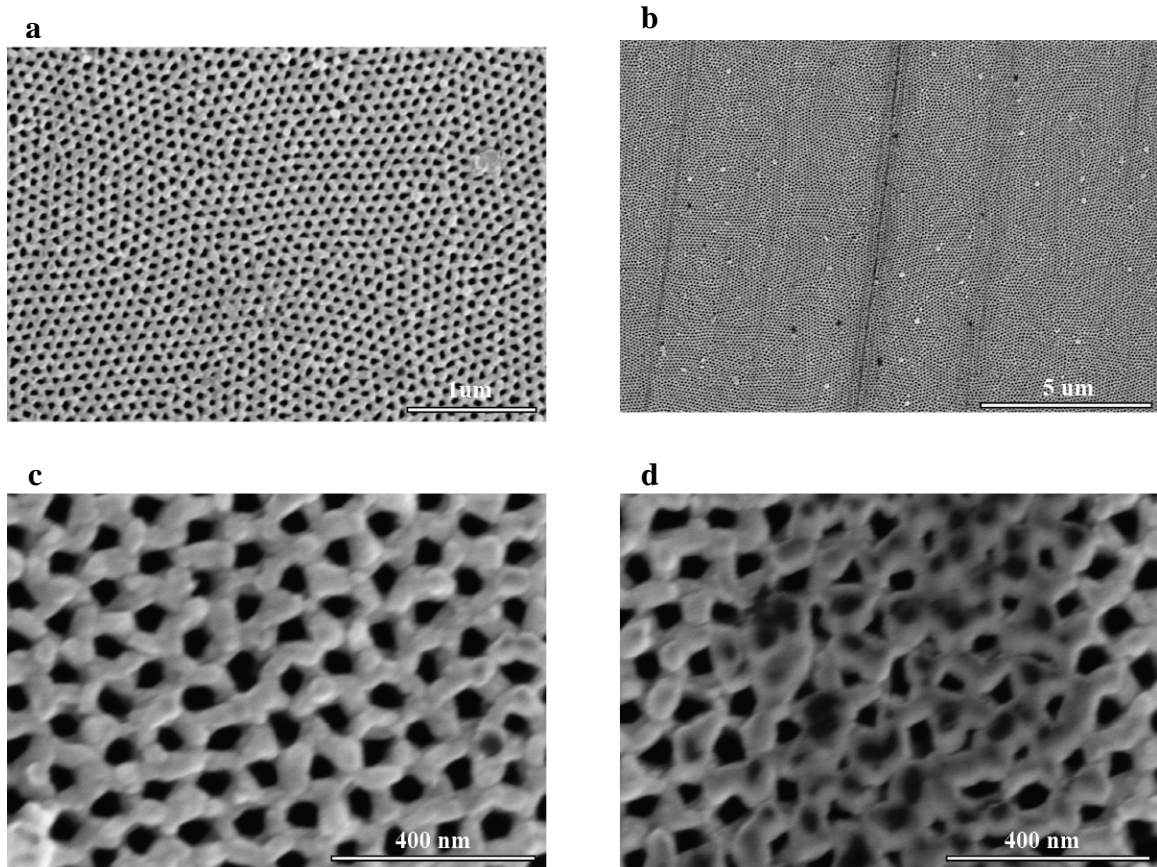


Figure A-2: Top view of (a, c) normal pore structures and (b,d) defect regions after Au sputtering

A3: The limits of the pore modification structure:

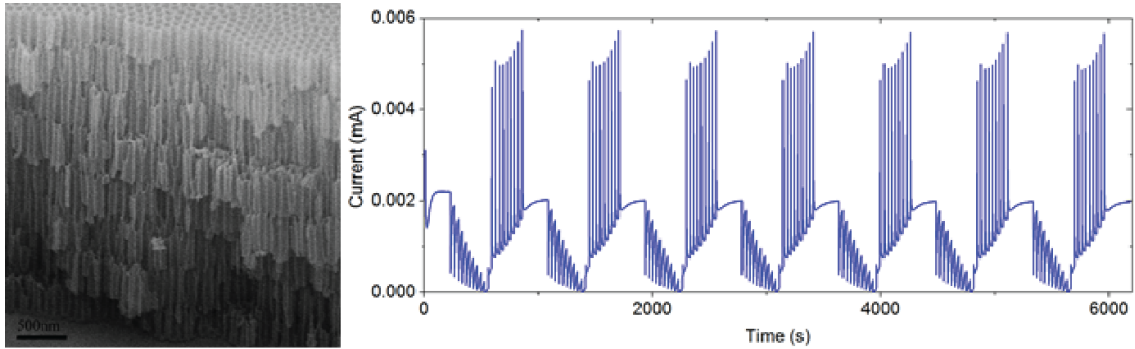


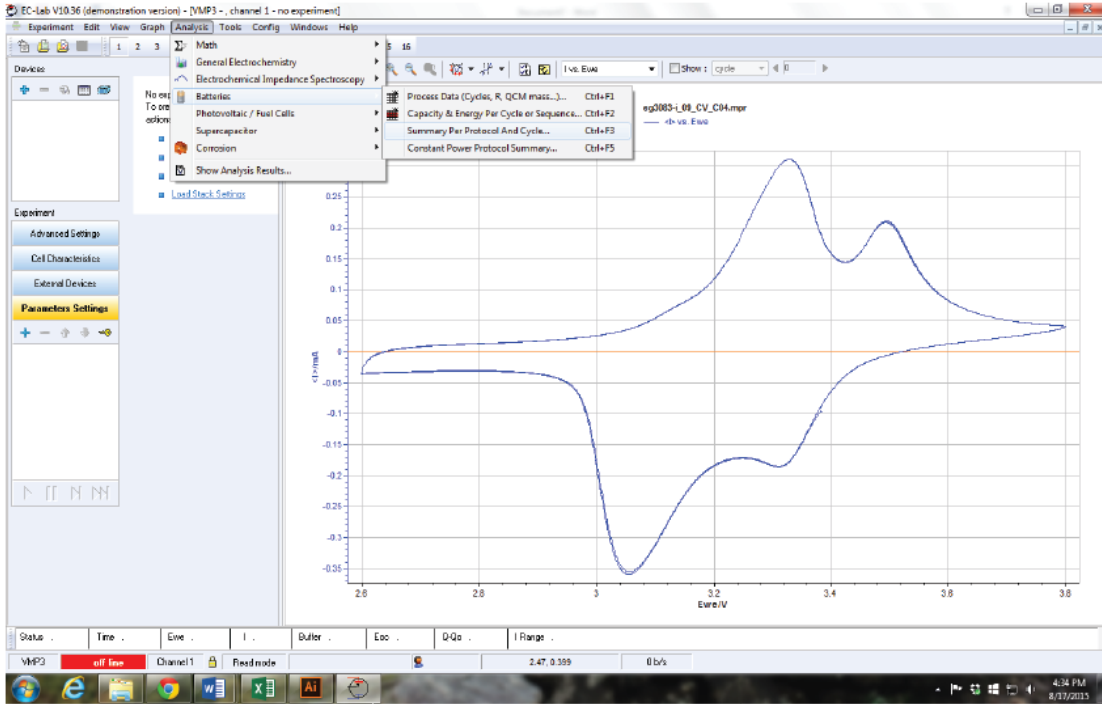
Figure A-3: SEM image and current plot from a template modified with 7 branches

Seven branches was the most inserted into a $\sim 2\mu\text{m}$ template. The ordered growth time at 40V is only 225s between each branch. This is not sufficient for the pores to be consistently returning to steady-state growth, which is indicated by a steady reaction current. The slope in the current between voltage step sequences suggests that the barrier layer is never returning to it's 40V steady state thickness. The additional current contributed by thickening of the barrier layer becomes more pronounced after each branch step. This suggests that 225s is too little ordered growth to retain predictable growth of the AAO templates.

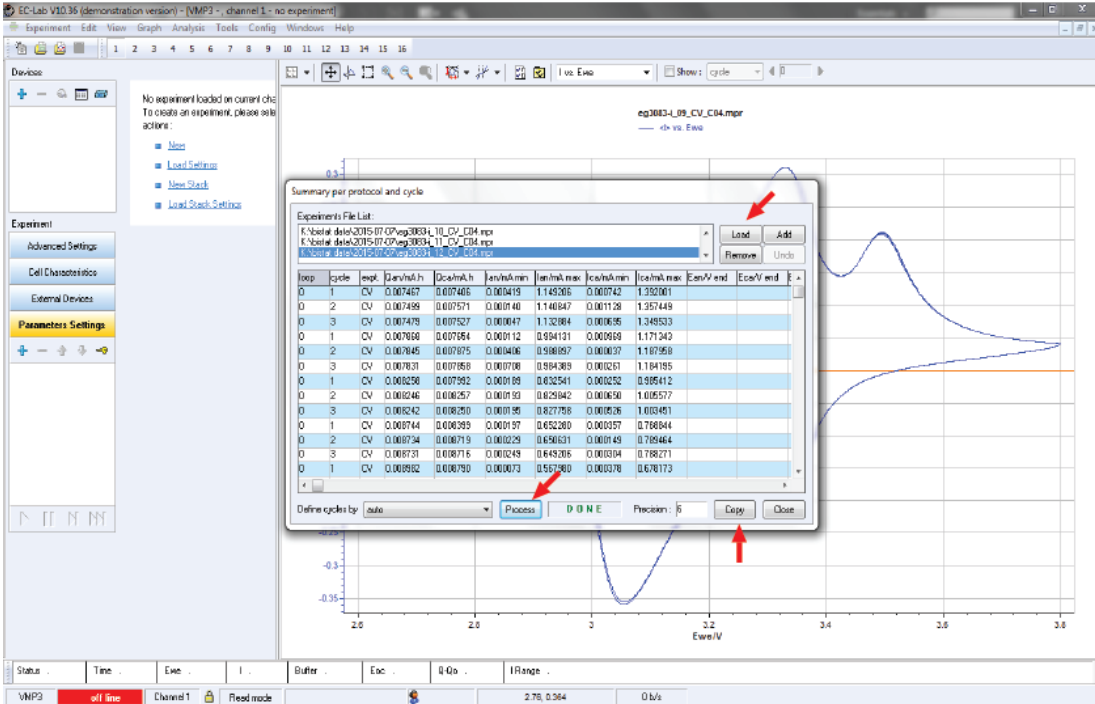
Appendix B: Charge Deconvolution Methods

Trasatti's Method using ECLab and Excel

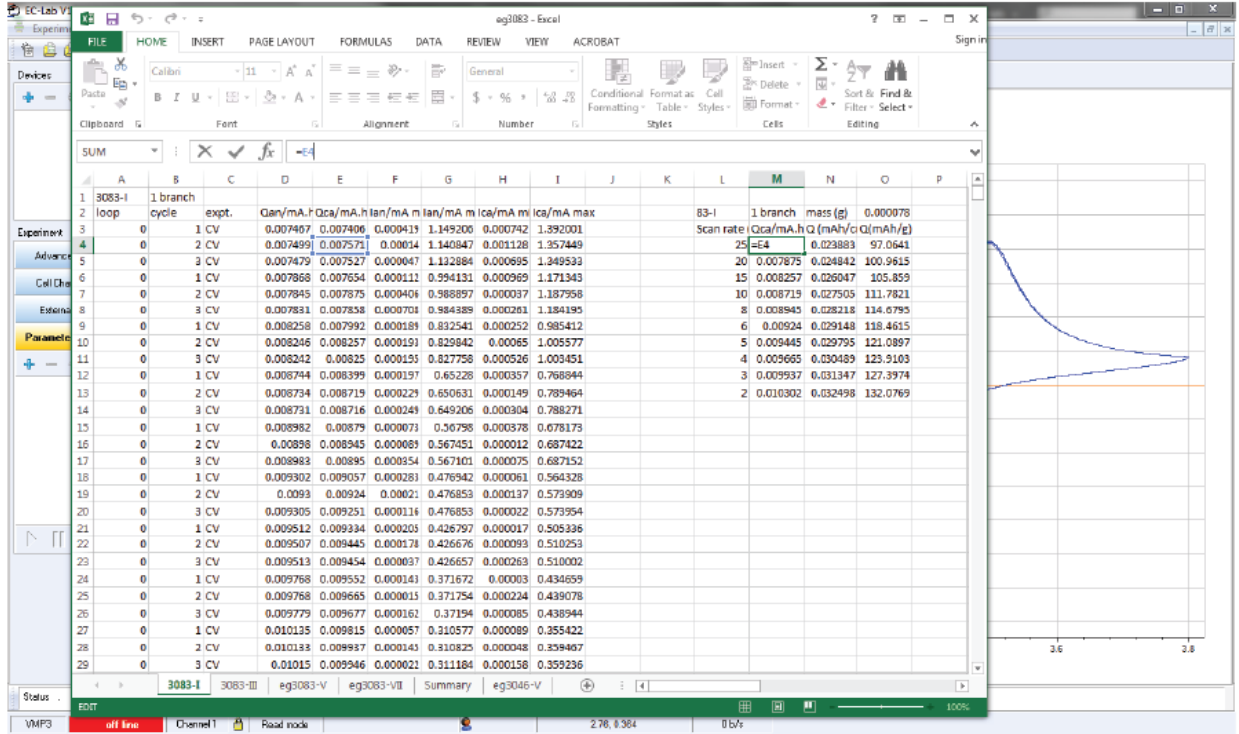
Step 1: Open the Analysis --> Batteries --> Summary Per Protocol and Cycle menu to process CV data



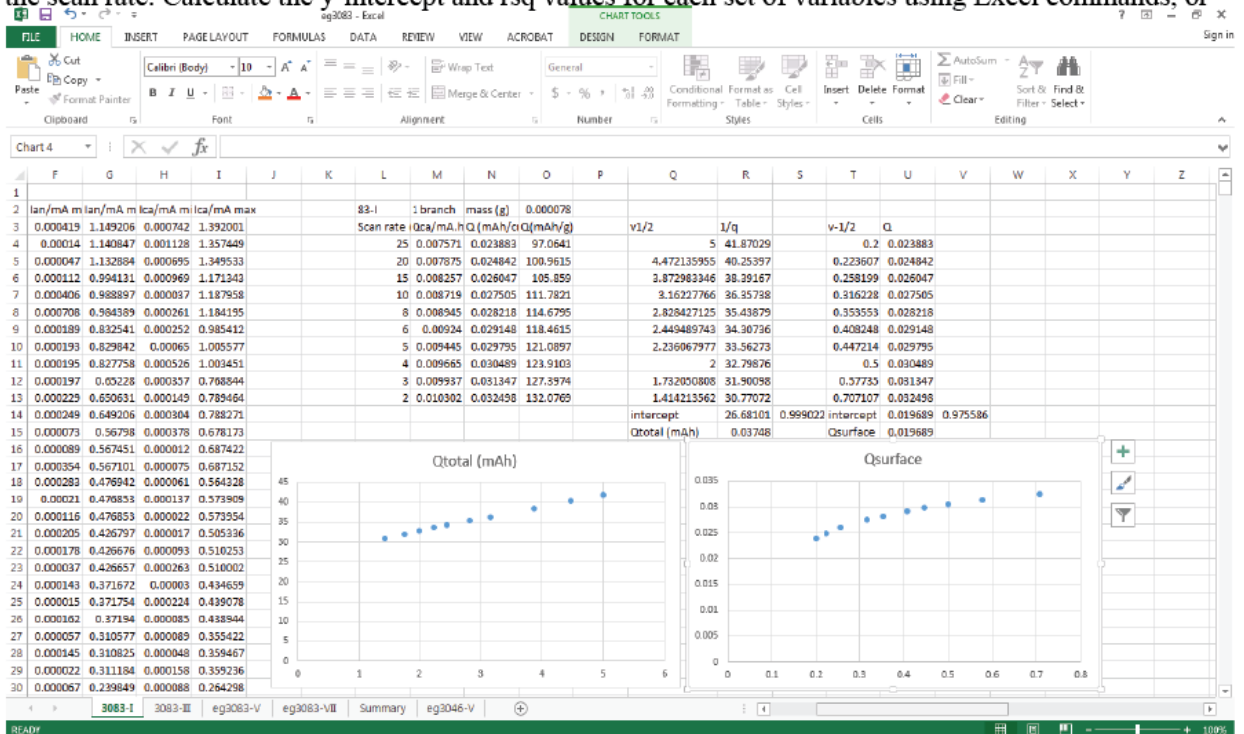
Step 2: Load files corresponding to CV experiments, set precision to 6 and click Process. ECLab will automatically integrate charge passed on the anodic (Q_{an}) and cathodic (Q_{ca}) CV sweeps for each scan, along with the maximum current. Copy the data to the clipboard



Step 3: Paste data into an Excel spreadsheet. Select the desired data (here, always Qca calculated for the 2nd cycle) and tabulate it with the scan rate. Normalize capacity (Qca) by mass or surface area if desired.

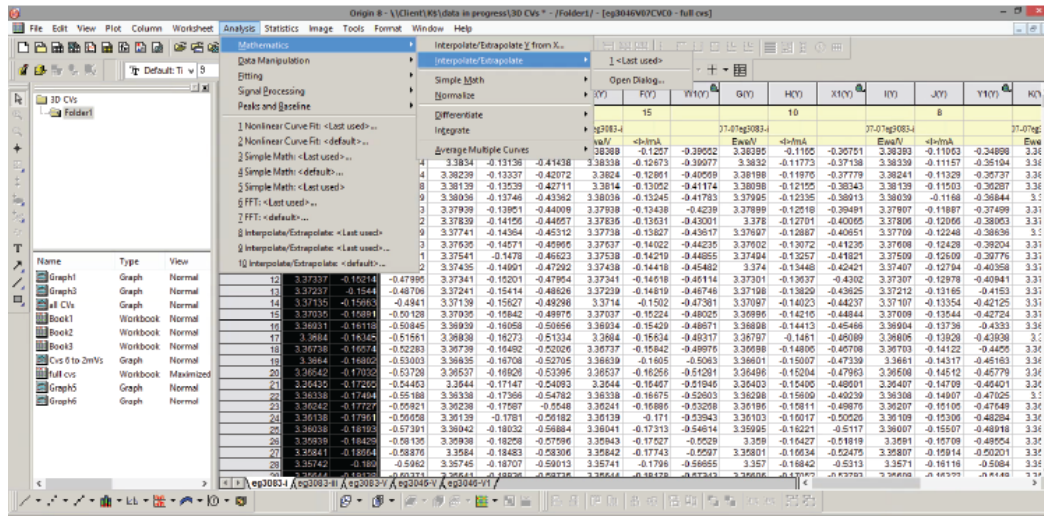


Step 4: Calculate the square root of the scan rate, the inverse of the charge and the inverse square root of the scan rate. Calculate the y-intercept and rsq values for each set of variables using Excel commands, or

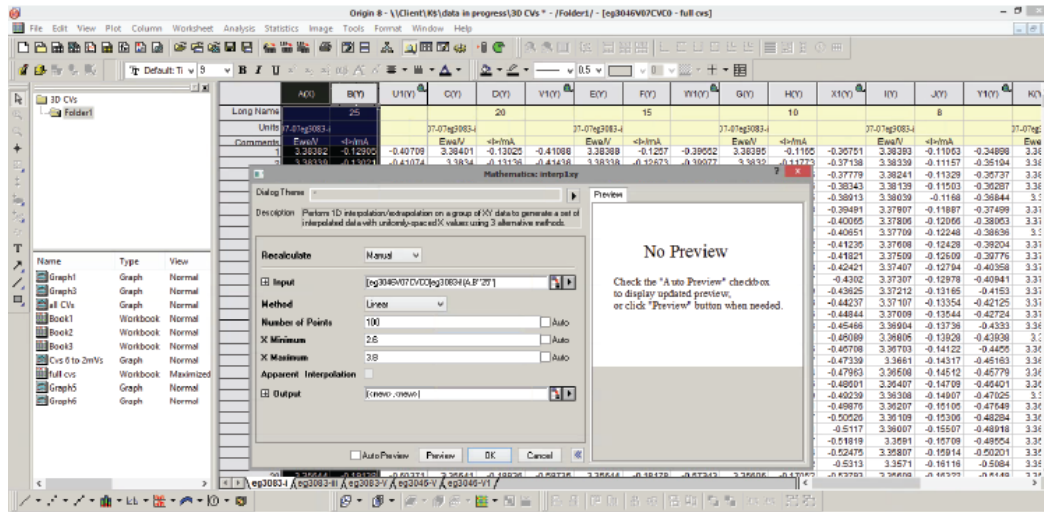


Dunn's Method using Origin and Excel

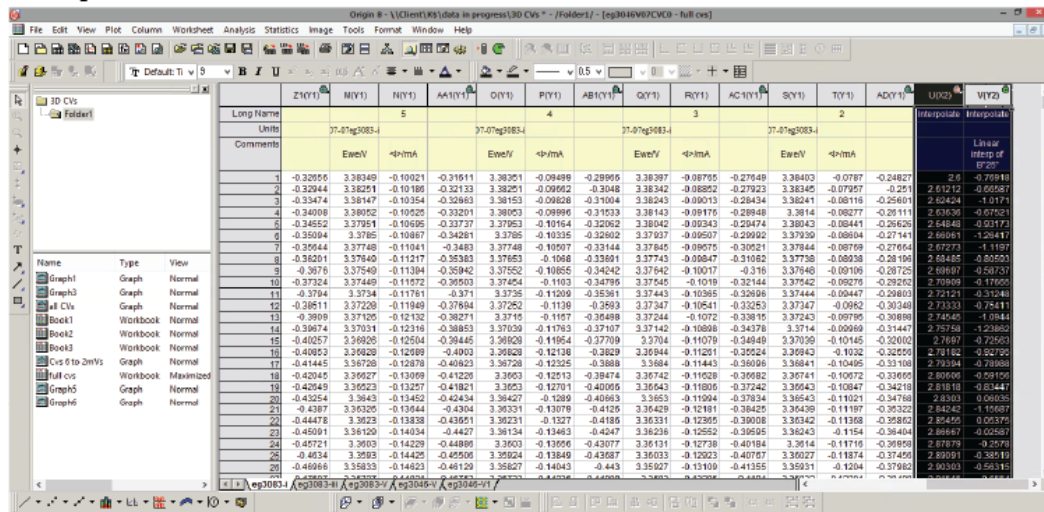
Step 1: Import CV data from EClab or other data collection software. For each scan rate, select Potential and Current, and open the Interpolate/Extrapolate dialog box



Step 2: Enter the number of points desired (here, 100) and the minimum and maximum values (2.6 and 3.8 here). Click OK.



Step 3: Interpolated data will appear at the end of the active sheet; highlight and copy to the clipboard



References

- (1) Goodenough, J. B.; Kim, Y. Challenges for Rechargeable Li Batteries †. *Chem. Mater.* **2010**, *22* (3), 587–603.
- (2) *Lithium Batteries Advanced Technologies and Applications.*, 1st ed.; Scrosati, B., Abraham, K. M., van Schalkwijk, W. A., Hassoun, J., Eds.; Wiley: Hoboken, 2013.
- (3) Luo, X.; Wang, J.; Dooner, M.; Clarke, J. Overview of Current Development in Electrical Energy Storage Technologies and the Application Potential in Power System Operation. *Appl. Energy* **2014**, *137*, 511–536.
- (4) *EPRI-DOE Handbook of Energy Storage for Transmission and Distribution Applications*; EPRI Palo Alto, CA and the U.S. Department of Energy, Washington, DC, 2003.
- (5) Nathan, M. Microbattery Technologies for Miniaturized Implantable Medical Devices. *Curr. Pharm. Biotechnol.* **2010**, *11* (4), 404–410.
- (6) Peckerar, M.; Dilli, Z.; Dornajafi, M.; Goldsman, N.; Ngu, Y.; Proctor, R. B.; Krupsaw, B. J.; Lowy, D. A. A Novel High Energy Density Flexible Galvanic Cell. *Energy Environ. Sci.* **2011**, *4* (5), 1807.
- (7) *Advances in Lithium-Ion Batteries*; van Schalkwijk, W., Scrosati, B., Eds.; Springer US, 2002.
- (8) Monthly battery sales statistics www.bar.or.jp/e/statistics/02.php (accessed Jan 1, 2015).
- (9) Fauteux, D.; Koksang, R. Rechargeable Lithium Battery Anodes: Alternatives to Metallic Lithium. *J. Appl. Electrochem.* **1993**, *23* (1), 1–10.
- (10) Crowther, O.; West, A. C. Effect of Electrolyte Composition on Lithium Dendrite Growth. *J. Electrochem. Soc.* **2008**, *155* (11), A806–A811.
- (11) Xu, K.; von Cresce, A. Interfacing Electrolytes with Electrodes in Li Ion Batteries. *J. Mater. Chem.* **2011**, *21* (27), 9849–9864.
- (12) Smart, M. C. Irreversible Capacities of Graphite in Low-Temperature Electrolytes for Lithium-Ion Batteries. *J. Electrochem. Soc.* **1999**, *146* (11), 3963.
- (13) Fergus, J. W. Ceramic and Polymeric Solid Electrolytes for Lithium-Ion Batteries. *J. Power Sources* **2010**, *195* (15), 4554–4569.

- (14) Lewandowski, A.; Świdarska-Mocek, A. Ionic Liquids as Electrolytes for Li-Ion batteries—An Overview of Electrochemical Studies. *J. Power Sources* **2009**, *194* (2), 601–609.
- (15) Whittingham, M. S. Electrical Energy Storage and Intercalation Chemistry. *Science* **1976**, *192* (4244), 1126–1127.
- (16) Mizushima, K.; Jones, P. C.; Wiseman, P. J.; Goodenough, J. B. Li_xCoO_2 ($0 < x < 1$): A New Cathode Material for Batteries of High Energy Density. *Mater. Res. Bull.* **1980**, *15* (6), 783–789.
- (17) Thomas, M.; Bruce, P.; Goodenough, J. Lithium Mobility in the Layered Oxide $\text{Li}_{1-x}\text{CoO}_2$. *Solid State Ionics* **1985**, *17* (1), 13–19.
- (18) *Electrochemical Energy Storage for Renewable Sources and Grid Balancing*; Moseley, P. T., Garche, J., Eds.; Elsevier: Amsterdam, 2014.
- (19) Whittingham, M. S. The Role of Ternary Phases in Cathode Reactions. *J. Electrochem. Soc.* **1976**, *123* (3), 315–320.
- (20) Wang, Y.; Cao, G. Developments in Nanostructured Cathode Materials for High-Performance Lithium-Ion Batteries. *Adv. Mater.* **2008**, *20* (12), 2251–2269.
- (21) Braithwaite, J. S.; Catlow, C. R. A.; Gale, J. D.; Harding, J. H. Lithium Intercalation into Vanadium Pentoxide: A Theoretical Study. *Chem. Mater.* **1999**, *11* (8), 1990–1998.
- (22) Galy, J. Vanadium Pentoxide and Vanadium Oxide bronzes—Structural Chemistry of Single (S) and Double (D) Layer $\text{M}_x\text{V}_2\text{O}_5$ Phases. *J. Solid State Chem.* **1992**, *100* (2), 229–245.
- (23) Ebner, M.; Chung, D.-W.; García, R. E.; Wood, V. Tortuosity Anisotropy in Lithium-Ion Battery Electrodes. *Adv. Energy Mater.* **2014**, *4* (5), 1301278–1301278.
- (24) Thorat, I. V.; Stephenson, D. E.; Zacharias, N. A.; Zaghbi, K.; Harb, J. N.; Wheeler, D. R. Quantifying Tortuosity in Porous Li-Ion Battery Materials. *J. Power Sources* **2009**, *188* (2), 592–600.
- (25) Bae, C. J.; Erdonmez, C. K.; Halloran, J. W.; Chiang, Y. M. Design of Battery Electrodes with Dual-Scale Porosity to Minimize Tortuosity and Maximize Performance. *Adv. Mater.* **2013**, *25* (9), 1254–1258.
- (26) DuBeshter, T.; Sinha, P. K.; Sakars, A.; Fly, G. W.; Jorne, J. Measurement of Tortuosity and Porosity of Porous Battery Electrodes. *J. Electrochem. Soc.* **2014**, *161* (4), A599–A605.

- (27) Ebner, M.; Wood, V. Tool for Tortuosity Estimation in Lithium Ion Battery Porous Electrodes. *J. Electrochem. Soc.* **2014**, *162* (2), A3064–A3070.
- (28) Chung, D.-W.; Ebner, M.; Ely, D. R.; Wood, V.; Edwin García, R. Validity of the Bruggeman Relation for Porous Electrodes. *Model. Simul. Mater. Sci. Eng.* **2013**, *21* (7), 074009.
- (29) Kehrwald, D.; Shearing, P. R.; Brandon, N. P.; Sinha, P. K.; Harris, S. J. Local Tortuosity Inhomogeneities in a Lithium Battery Composite Electrode. *J. Electrochem. Soc.* **2011**, *158* (12), A1393–A1399.
- (30) Ebner, M.; Wood, V. Tool for Tortuosity Estimation in Lithium Ion Battery Porous Electrodes. *J. Electrochem. Soc.* **2014**, *162* (2), A3064–A3070.
- (31) Harris, S. J.; Lu, P. Effects of Inhomogeneities—Nanoscale to Mesoscale—on the Durability of Li-Ion Batteries. *J. Phys. Chem. C* **2013**, *117* (13), 6481–6492.
- (32) Kehrwald, D.; Shearing, P.; Brandon, N.; Sinha, P.; Harris, S. Local Tortuosity Inhomogeneities in a Lithium Battery Composite Electrode. *J. Electrochem. Soc.* **2011**, *158* (12), A1393–A1399.
- (33) Jiang, J.; Li, Y.; Liu, J.; Huang, X.; Yuan, C.; Lou, X. W. D. Recent Advances in Metal Oxide-Based Electrode Architecture Design for Electrochemical Energy Storage. *Adv. Mater.* **2012**, *24* (38), 5166–5180.
- (34) Liu, R.; Duay, J.; Lee, S. B. Heterogeneous Nanostructured Electrode Materials for Electrochemical Energy Storage. *Chem. Commun.* **2011**, *47* (5), 1384–1404.
- (35) Wang, W.; Tian, M.; Abdulagatov, A.; George, S.; Lee, Y.-C.; Yang, R. Three-Dimensional Ni/TiO₂ Nanowire Network for High Areal Capacity Lithium Ion Microbattery Applications. *Nano Lett.* **2012**, *12* (2), 655–660.
- (36) From Quanta to the Continuum: Opportunities for Mesoscale Science. Department of Energy, Office of Science 2012.
- (37) Zhang, H.; Yu, X.; Braun, P. V. Three-Dimensional Bicontinuous Ultrafast-Charge and -Discharge Bulk Battery Electrodes. *Nat. Nanotechnol.* **2011**, *6* (5), 277–281.
- (38) Pikul, J. H.; Zhang, H. G.; Cho, J.; Braun, P. V.; King, W. P. High-Power Lithium Ion Microbatteries from Interdigitated Three-Dimensional Bicontinuous Nanoporous Electrodes. *Nat. Commun.* **2013**, *4*.
- (39) Banerjee, P.; Perez, I.; Henn-Lecordier, L.; Lee, S. B.; Rubloff, G. W. Nanotubular Metal-Insulator-Metal Capacitor Arrays for Energy Storage. *Nat. Nanotechnol.* **2009**, *4* (5), 292–296.

- (40) Liu, R.; Sang, B. L. MnO₂/poly(3,4-Ethylenedioxythiophene) Coaxial Nanowires by One-Step Coelectrodeposition for Electrochemical Energy Storage. *J. Am. Chem. Soc.* **2008**, *130* (10), 2942–2943.
- (41) Duay, J.; Gillette, E.; Liu, R.; Lee, S. B. Highly Flexible Pseudocapacitor Based on Freestanding Heterogeneous MnO₂/conductive Polymer Nanowire Arrays. *Phys. Chem. Chem. Phys.* **2012**, *14* (10), 3329–3337.
- (42) Liu, C.; Gillette, E. I.; Chen, X.; Pearse, A. J.; Kozen, A. C.; Schroeder, M. A.; Gregorczyk, K. E.; Lee, S. B.; Rubloff, G. W. An All-in-One Nanopore Battery Array. *Nat. Nanotechnol.* **2014**, *9* (12), 1031–1039.
- (43) Cheng, F.; Tao, Z.; Liang, J.; Chen, J. Template-Directed Materials for Rechargeable Lithium-Ion Batteries †. *Chem. Mater.* **2008**, *20* (3), 667–681.
- (44) Wu, Q.; Li, W.; Cheng, Y.; Jiang, Z. Homogenous LiCoO₂ Nanoparticles Prepared Using Surfactant P123 as Template and Its Application to Manufacturing Ultra-Thin-Film Electrode. *Mater. Chem. Phys.* **2005**, *91* (2-3), 463–467.
- (45) Spahr, M. E. Vanadium Oxide Nanotubes. A New Nanostructured Redox-Active Material for the Electrochemical Insertion of Lithium. *J. Electrochem. Soc.* **1999**, *146* (8), 2780–2783.
- (46) Zúkalová, M.; Kalbáč, M.; Kavan, L.; Exnar, I.; Graetzel, M. Pseudocapacitive Lithium Storage in TiO₂ (B). *Chem. Mater.* **2005**, *17* (5), 1248–1255.
- (47) Li, X.; Cheng, F.; Guo, B.; Chen, J. Template-Synthesized LiCoO₂, LiMn₂O₄, and LiNi_{0.8}Co_{0.2}O₂ Nanotubes as the Cathode Materials of Lithium Ion Batteries. *J. Phys. Chem. B* **2005**, *109* (29), 14017–14024.
- (48) Meyers, C. J.; Shah, S. D.; Patel, S. C.; Sneeringer, R. M.; Bessel, C. A.; Dollahon, N. R.; Leising, R. A.; Takeuchi, E. S. Templated Synthesis of Carbon Materials from Zeolites (Y, Beta, and ZSM-5) and a Montmorillonite Clay (K10): Physical and Electrochemical Characterization. *J. Phys. Chem. B* **2001**, *105* (11), 2143–2152.
- (49) Jiao, F.; Shaju, K. M.; Bruce, P. G. Synthesis of Nanowire and Mesoporous Low-Temperature LiCoO₂ by a Post-Templating Reaction. *Angew. Chem. Int. Ed. Engl.* **2005**, *44* (40), 6550–6553.
- (50) O’Sullivan, J. P.; Wood, G. C. The Morphology and Mechanism of Formation of Porous Anodic Films on Aluminium. *Proc. R. Soc. London. A. Math. Phys. Sci.* **1970**, *317* (1531), 511–543.
- (51) Martin, C. R. Membrane-Based Synthesis of Nanomaterials. *Chem. Mater.* **1996**, *8* (8), 1739–1746.

- (52) Santos, A.; Kumeria, T.; Losic, D. Nanoporous Anodic Aluminum Oxide for Chemical Sensing and Biosensors. *TrAC - Trends Anal. Chem.* **2013**, *44*, 25–38.
- (53) Alvarez, S. D.; Li, C.-P.; Chiang, C. E.; Schuller, I. K.; Sailor, M. J. A Label-Free Porous Alumina Interferometric Immunosensor. *ACS Nano* **2009**, *3* (10), 3301–3307.
- (54) Lee, S.; Kim, D.; Gillette, E.; Oh, J.; Han, S. W.; Lee, S. B. Anodized Pore Structural Evolution of Focused Ion Beam Patterned Al: Direct Analysis of Branched Nanopores and Nanosacks. *Phys. Chem. Chem. Phys.* **2013**, *15* (26), 10659–10665.
- (55) Abdul Mutalib Md, J.; Dusan, L.; Nicolas, H. V. Nanoporous Anodic Aluminium Oxide: Advances in Surface Engineering and Emerging Applications. *Prog. Mater. Sci.* **2013**, *58* (5), 636–704.
- (56) Thompson, G. Porous Anodic Alumina: Fabrication, Characterization and Applications. *Thin Solid Films* **1997**, *297* (1-2), 192–201.
- (57) Masuda, H.; Satoh, M. Fabrication of Gold Nanodot Array Using Anodic Porous Alumina as an Evaporation Mask. *Jpn. J. Appl. Phys.* **1996**, *35* (Part 2, No. 1B), L126–L129.
- (58) Masuda, H.; Fukuda, K. Ordered Metal Nanohole Arrays Made by a Two-Step Replication of Honeycomb Structures of Anodic Alumina. *Science* **1995**, *268* (5216), 1466–1468.
- (59) Masuda, H.; Hasegawa, F.; Ono, S. Self-Ordering of Cell Arrangement of Anodic Porous Alumina Formed in Sulfuric Acid Solution. *J. Electrochem. Soc.* **1997**, *144* (5), L127–L129.
- (60) Li, a. P.; Müller, F.; Birner, A.; Nielsch, K.; Gösele, U. Hexagonal Pore Arrays with a 50–420 Nm Interpore Distance Formed by Self-Organization in Anodic Alumina. *J. Appl. Phys.* **1998**, *84* (11), 6023–6026.
- (61) Lee, W.; Ji, R.; Gösele, U.; Nielsch, K. Fast Fabrication of Long-Range Ordered Porous Alumina Membranes by Hard Anodization. *Nat. Mater.* **2006**, *5* (9), 741–747.
- (62) Nielsch, K.; Choi, J.; Schwirn, K.; Wehrspohn, R. B.; Gösele, U. Self-Ordering Regimes of Porous Alumina: The 10% Porosity Rule. *Nano Lett.* **2002**, *2* (7), 677–680.
- (63) Thompson, G. E.; Wood, G. C. Porous Anodic Film Formation on Aluminium. *Nature* **1981**, *290* (5803), 230–232.

- (64) Xu, J.; Li, J.; Papadopoulos, C. No Title. *Nature* **1999**, *402* (6759), 253–254.
- (65) Ho, A. Y. Y.; Gao, H.; Lam, Y. C.; Rodríguez, I. Controlled Fabrication of Multitiered Three Dimensional Nanostructures
Mater. **2008**, *18* (14), 2057–2063.
- (66) Losic, D. Preparation of Porous Anodic Alumina with Periodically Perforated Pores. *Langmuir* **2009**, *25* (10), 5426–5431.
- (67) Meng, G.; Jung, Y. J.; Cao, A.; Vajtai, R.; Ajayan, P. M. Controlled Fabrication of Hierarchically Branched Nanopores, Nanotubes, and Nanowires. *Proc. Natl. Acad. Sci. U. S. A.* **2005**, *102* (20), 7074–7078.
- (68) Lee, W.; Schwirn, K.; Steinhart, M.; Pippel, E.; Scholz, R.; Gösele, U. Structural Engineering of Nanoporous Anodic Aluminium Oxide by Pulse Anodization of Aluminium. *Nat. Nanotechnol.* **2008**, *3* (4), 234–239.
- (69) Scholes, G. D.; Rumbles, G. Excitons in Nanoscale Systems. *Nat. Mater.* **2006**, *5* (9), 683–696.
- (70) Zhou, F.; Baron-Wiecheć, A.; Garcia-Vergara, S. J.; Curioni, M.; Habazaki, H.; Skeldon, P.; Thompson, G. E. Effects of Current Density and Electrolyte Temperature on the Volume Expansion Factor of Anodic Alumina Formed in Oxalic Acid. *Electrochim. Acta* **2012**, *59*, 186–195.
- (71) Houser, J. E.; Hebert, K. R. The Role of Viscous Flow of Oxide in the Growth of Self-Ordered Porous Anodic Alumina Films. *Nat. Mater.* **2009**, *8* (5), 415–420.
- (72) Banerjee, S.; Myung, Y.; Banerjee, P. Confined Anodic Aluminum Oxide Nanopores on Aluminum Wires. *RSC Adv.* **2014**, *4* (16), 7919–7926.
- (73) Sharma, G.; Pishko, M. V.; Grimes, C. a.; Gaurav, S.; Michael, V. P.; Craig, A. G. Fabrication of Metallic Nanowire Arrays by Electrodeposition into Nanoporous Alumina Membranes: Effect of Barrier Layer. *J. Mater. Sci.* **2007**, *42* (13), 4738–4744.
- (74) Nielsch, K.; Müller, F.; Li, A.-P.; Gösele, U. Uniform Nickel Deposition into Ordered Alumina Pores by Pulsed Electrodeposition. *Adv. Mater.* **2000**, *12* (8), 582–586.
- (75) Najafi, M.; Soltanian, S.; Danyali, H.; Hallaj, R.; Salimi, A.; Elahi, S. M.; Servati, P. Preparation of Cobalt Nanowires in Porous Aluminum Oxide: Study of the Effect of Barrier Layer. *J. Mater. Res.* **2012**, *27* (18), 2382–2390.

- (76) Sherrill, S. SINGLE AND MULTI-DIMENSIONAL AAO TEMPLATE SYNTHESIZED HETEROGENEOUS NANOSTRUCTURES FOR ELECTROCHEMICAL ENERGY STORAGE, University of Maryland, 2012.
- (77) Gillette, E.; Wittenberg, S.; Graham, L.; Lee, K.; Rubloff, G.; Banerjee, P.; Lee, S. B. Anodization Control for Barrier-Oxide Thinning and 3D Interconnected Pores and Direct Electrodeposition of Nanowire Networks on Native Aluminium Substrates. *Phys. Chem. Chem. Phys.* **2015**, *17* (5), 3873–3879.
- (78) Kovtyukhova, N. I.; Mallouk, T. E.; Mayer, T. S. Templated Surface Sol-Gel Synthesis of SiO₂ Nanotubes and SiO₂-Insulated Metal Nanowires. *Adv. Mater.* **2003**, *15* (10), 780–785.
- (79) Li, N.; Patrissi, C. J.; Che, G.; Martin, C. R. Rate Capabilities of Nanostructured LiMn₂O₄ Electrodes in Aqueous Electrolyte. *J. Electrochem. Soc.* **2000**, *147* (6), 2044–2049.
- (80) Menon, V. P.; Martin, C. R. Fabrication and Evaluation of Nanoelectrode Ensembles. *Anal. Chem.* **1995**, *67* (13), 1920–1928.
- (81) Brumlik, C. J.; Martin, C. R. Template Synthesis of Metal Microtubules. *J. Am. Chem. Soc.* **1991**, *113* (8), 3174–3175.
- (82) Che, G.; Miller, S. A.; Fisher, E. R.; Martin, C. R. An Electrochemically Driven Actuator Based on a Nanostructured Carbon Material. *Anal. Chem.* **1999**, *71* (15), 3187–3191.
- (83) Bachmann, J.; Jing, J.; Knez, M.; Barth, S.; Shen, H.; Mathur, S.; Gösele, U.; Nielsch, K. Ordered Iron Oxide Nanotube Arrays of Controlled Geometry and Tunable Magnetism by Atomic Layer Deposition. *J. Am. Chem. Soc.* **2007**, *129* (31), 9554–9555.
- (84) Yang, G.; Li, L.; Jiang, J.; Yang, Y. Direct Electrodeposition of Gold Nanotube Arrays of Rough and Porous Wall by Cyclic Voltammetry and Its Applications of Simultaneous Determination of Ascorbic Acid and Uric Acid. *Mater. Sci. Eng. C. Mater. Biol. Appl.* **2012**, *32* (6), 1323–1330.
- (85) Liu, H.; Lu, B.; Wei, S.; Bao, M.; Wen, Y.; Wang, F. Electrodeposited Highly-Ordered Manganese Oxide Nanowire Arrays for Supercapacitors. *Solid State Sci.* **2012**, *14* (7), 789–793.
- (86) Duay, J.; Sherrill, S. a; Gui, Z.; Gillette, E.; Lee, S. B. Self-Limiting Electrodeposition of Hierarchical MnO₂ and M(OH)₂ /MnO₂ Nanofibril/nanowires: Mechanism and Supercapacitor Properties. *ACS Nano* **2013**, *7* (2), 1200–1214.

- (87) Leskelä, M.; Ritala, M. Atomic Layer Deposition Chemistry: Recent Developments and Future Challenges. *Angew. Chem. Int. Ed. Engl.* **2003**, *42* (45), 5548–5554.
- (88) Pomerantseva, E.; Gerasopoulos, K.; Chen, X.; Rubloff, G.; Ghodssi, R. Electrochemical Performance of the Nanostructured Biotemplated V₂O₅ Cathode for Lithium-Ion Batteries. *J. Power Sources* **2012**, *206*, 282–287.
- (89) Sherrill, S. A.; Duay, J.; Gui, Z.; Banerjee, P.; Rubloff, G. W.; Lee, S. B. MnO₂/TiN Heterogeneous Nanostructure Design for Electrochemical Energy Storage. *Phys. Chem. Chem. Phys.* **2011**, *13* (33), 15221–15226.
- (90) Cleveland, E. R.; Banerjee, P.; Perez, I.; Lee, S. B.; Rubloff, G. W. Profile Evolution for Conformal Atomic Layer Deposition over Nanotopography. *ACS Nano* **2010**, *4* (8), 4637–4644.
- (91) Marichy, C.; Pinna, N. Carbon-Nanostructures Coated/decorated by Atomic Layer Deposition: Growth and Applications. *Coord. Chem. Rev.* **2013**, *257* (23-24), 3232–3253.
- (92) Elam, J. W.; Routkevitch, D.; Mardilovich, P. P.; George, S. M. Conformal Coating on Ultrahigh-Aspect-Ratio Nanopores of Anodic Alumina by Atomic Layer Deposition. *Chem. Mater.* **2003**, *15* (18), 3507–3517.
- (93) Egerton, R. F. *Physical Principles of Electron Microscopy*; Springer US: Boston, MA, 2005.
- (94) Williams, D. B.; Carter, C. B. *Transmission Electron Microscopy: A Textbook for Materials Science*; 2009; Vol. V1-V4.
- (95) Cao, G. *Nanostructures & Nanomaterials: Synthesis Properties and Applications*; Imperial College Press: London, 2004.
- (96) Simon, P.; Gogotsi, Y. Materials for Electrochemical Capacitors. *Nat. Mater.* **2008**, *7* (11), 845–854.
- (97) Chmiola, J.; Yushin, G.; Gogotsi, Y.; Portet, C.; Simon, P.; Taberna, P. L. Anomalous Increase in Carbon Capacitance at Pore Sizes Less than 1 Nanometer. *Science* **2006**, *313* (5794), 1760–1763.
- (98) Chmiola, J.; Largeot, C.; Taberna, P.-L.; Simon, P.; Gogotsi, Y. Monolithic Carbide-Derived Carbon Films for Micro-Supercapacitors. *Science* **2010**, *328* (5977), 480–483.

- (99) Pech, D.; Brunet, M.; Durou, H.; Huang, P.; Mochalin, V.; Gogotsi, Y.; Taberna, P.-L.; Simon, P. Ultrahigh-Power Micrometre-Sized Supercapacitors Based on Onion-like Carbon. *Nat. Nanotechnol.* **2010**, *5* (9), 651–654.
- (100) Simon, P.; Gogotsi, Y. Charge Storage Mechanism in Nanoporous Carbons and Its Consequence for Electrical Double Layer Capacitors. *Philos. Trans. A. Math. Phys. Eng. Sci.* **2010**, *368* (1923), 3457–3467.
- (101) Merlet, C.; Rotenberg, B.; Madden, P. a; Taberna, P.-L.; Simon, P.; Gogotsi, Y.; Salanne, M. On the Molecular Origin of Supercapacitance in Nanoporous Carbon Electrodes. *Nat. Mater.* **2012**, *11* (4), 306–310.
- (102) Portet, C.; Yushin, G.; Gogotsi, Y. Electrochemical Performance of Carbon Onions, Nanodiamonds, Carbon Black and Multiwalled Nanotubes in Electrical Double Layer Capacitors. *Carbon N. Y.* **2007**, *45* (13), 2511–2518.
- (103) Ardizzone, S.; Fregonara, G.; Trasatti, S. “Inner” and “outer” Active Surface of RuO₂ Electrodes. *Electrochim. Acta* **1990**, *35* (1), 263–267.
- (104) Wang, J.; Polleux, J.; Lim, J.; Dunn, B. Pseudocapacitive Contributions to Electrochemical Energy Storage in TiO₂ (anatase) Nanoparticles. *J. Phys. Chem. C* **2007**, *111* (40), 14925–14931.
- (105) Graham, L. M.; Cho, S.; Kim, S. K.; Noked, M.; Lee, S. B. Role of Boric Acid in Nickel Nanotube Electrodeposition: A Surface-Directed Growth Mechanism. *Chem. Commun.* **2014**, *50* (5), 527–529.
- (106) Liu, L.; Pippel, E.; Scholz, R.; Gösele, U. Nanoporous Pt-Co Alloy Nanowires: Fabrication, Characterization, and Electrocatalytic Properties. *Nano Lett.* **2009**, *9* (12), 4352–4358.
- (107) Duay, J.; Gillette, E.; Hu, J.; Lee, S. B. Controlled Electrochemical Deposition and Transformation of Hetero-Nanoarchitected Electrodes for Energy Storage. *Phys. Chem. Chem. Phys.* **2013**, *15* (21), 7976–7993.
- (108) Liu, R.; Cho, S. II; Lee, S. B. Poly(3,4-Ethylenedioxythiophene) Nanotubes as Electrode Materials for a High-Powered Supercapacitor. *Nanotechnology* **2008**, *19* (21), 215710.
- (109) Cepak, V. M.; Martin, C. R. Preparation of Polymeric Micro- and Nanostructures Using a Template-Based Deposition Method. *Chem. Mater.* **1999**, *11* (5), 1363–1367.
- (110) Olson, T. S.; Atanassov, P.; Brevnov, D. a. Electrodeposition of Gold Particles on Aluminum Substrates Containing Copper. *J. Phys. Chem. B* **2005**, *109* (3), 1243–1250.

- (111) Vorobyova, A. I.; Outkina, E. A.; Komar, O. M. Study of Metal Pillar Nanostructure Formation with Thin Porous Alumina Template. *Thin Solid Films* **2013**, *548*, 109–117.
- (112) Lei, W.; Henn-Lecordier, L.; Anderle, M.; Rubloff, G. W.; Barozzi, M.; Bersani, M. Real-Time Observation and Optimization of Tungsten Atomic Layer Deposition Process Cycle. *J. Vac. Sci. Technol. B Microelectron. Nanom. Struct.* **2006**, *24* (2), 780–789.
- (113) Henn-Lecordier, L.; Lei, W.; Anderle, M.; Rubloff, G. W. Real-Time Sensing and Metrology for Atomic Layer Deposition Processes and Manufacturing. *J. Vac. Sci. Technol. B Microelectron. Nanom. Struct.* **2007**, *25* (1), 130–139.
- (114) Gregorczyk, K.; Henn-Lecordier, L.; Gatineau, J.; Dussarrat, C.; Rubloff, G. Atomic Layer Deposition of Ruthenium Using the Novel Precursor bis(2,6,6-Trimethyl-Cyclohexadienyl)ruthenium. *Chem. Mater.* **2011**, *23* (10), 2650–2656.
- (115) Chen, X.; Pomerantseva, E.; Banerjee, P.; Gregorczyk, K.; Ghodssi, R.; Rubloff, G. Ozone-Based Atomic Layer Deposition of Crystalline V₂O₅ Films for High Performance Electrochemical Energy Storage. *Chem. Mater.* **2012**, *24*, 1255–1261.
- (116) Chen, X.; Pomerantseva, E.; Banerjee, P.; Gregorczyk, K.; Ghodssi, R.; Rubloff, G. Ozone-Based Atomic Layer Deposition of Crystalline V₂O₅ Films for High Performance Electrochemical Energy Storage. *Chem. Mater.* **2012**, *24* (7), 1255–1261.
- (117) Liu, C.; Gillette, E. I.; Chen, X.; Pearse, A. J.; Kozen, A. C.; Schroeder, M. A.; Gregorczyk, K. E.; Lee, S. B.; Rubloff, G. W. An All-in-One Nanopore Battery Array. *Nat. Nanotechnol.* **2014**, *9* (12), 1031–1039.
- (118) Landstorfer, M.; Jacob, T. Mathematical Modeling of Intercalation Batteries at the Cell Level and beyond. *Chem. Soc. Rev.* **2013**, *42* (8), 3234–3252.
- (119) Hörmann, N. G.; Jäckle, M.; Gossenberger, F.; Roman, T.; Forster-Tonigold, K.; Naderian, M.; Sakong, S.; Groß, A. Some Challenges in the First-Principles Modeling of Structures and Processes in Electrochemical Energy Storage and Transfer. *J. Power Sources* **2015**, *275*, 531–538.
- (120) Haspert, L. C.; Gillette, E.; Lee, S. B.; Rubloff, G. W. Perspective: Hybrid Systems Combining Electrostatic and Electrochemical Nanostructures for Ultrahigh Power Energy Storage. *Energy Environ. Sci.* **2013**, *6* (9), 2578–2590.
- (121) Barsoukov, E.; Macdonald, J. R. *Impedance Spectroscopy: Theory, Experiment, and Applications*; Barsoukov, E., Macdonald, J. R., Eds.; John Wiley & Sons, Inc.: Hoboken, NJ, USA, 2005.

- (122) Zhang, B.; Zhang, Y.; White, H. S. The Nanopore Electrode. *Anal. Chem.* **2004**, *76* (21), 6229–6238.
- (123) Fan, L.; Liu, Y.; Xiong, J.; White, H. S.; Chen, S. Electron-Transfer Kinetics and Electric Double Layer Effects in Nanometer-Wide Thin-Layer Cells. *ACS Nano* **2014**, *8* (10), 10426–10436.
- (124) Doyle, M.; Fuller, T. F.; Newman, J. Modeling of Galvanostatic Charge and Discharge of the Lithium/Polymer/Insertion Cell. *J. Electrochem. Soc.* **1993**, *140* (6), 1526–1533.
- (125) Albertus, P.; Christensen, J.; Newman, J. Experiments on and Modeling of Positive Electrodes with Multiple Active Materials for Lithium-Ion Batteries. *J. Electrochem. Soc.* **2009**, *156* (7), A606–A618.
- (126) Hart, R. W.; White, H. S.; Dunn, B.; Rolison, D. R. 3-D Microbatteries. *Electrochem. commun.* **2003**, *5* (2), 120–123.
- (127) Rubloff, G. W.; Kozen, A. C.; Bok Lee, S. From Nanoscience to Solutions in Electrochemical Energy Storage. *J. Vac. Sci. Technol. A Vacuum, Surfaces, Film.* **2013**, *31* (5), 0585031–58503120.
- (128) Sherrill, S.; Duay, J.; Gui, Z.; Banerjee, P.; Rubloff, G.; Lee, S. MnO₂/TiN Heterogeneous Nanostructure Design for Electrochemical Energy Storage. *Phys. Chem. Chem. Phys.* **2011**, *13* (33), 15221–15226.
- (129) Pell, W. G.; Conway, B. E. Quantitative Modeling of Factors Determining Ragone Plots for Batteries and Electrochemical Capacitors. *J. Power Sources* **1996**, *63* (2), 255–266.
- (130) Bard, A. J.; Faulkner, L. R. *Electrochemical Methods: Fundamental and Applications*, 2nd ed.; Wiley: New York.
- (131) Tang, Y.; Zhang, Y.; Deng, J.; Qi, D.; Leow, W. R.; Wei, J.; Yin, S.; Dong, Z.; Yazami, R.; Chen, Z.; et al. Unravelling the Correlation between the Aspect Ratio of Nanotubular Structures and Their Electrochemical Performance To Achieve High-Rate and Long-Life Lithium-Ion Batteries. *Angew. Chemie Int. Ed.* **2014**, *53* (49), 13488–13492.
- (132) Wang, J.; Polleux, J.; Lim, J.; Dunn, B. Pseudocapacitive Contributions to Electrochemical Energy Storage in TiO₂ (Anatase) Nanoparticles. *J. Phys. Chem. C* **2007**, *111*, 14925–14931.
- (133) Liu, R.; Duay, J.; Lane, T.; Lee, S. B. Synthesis and Characterization of RuO₂/poly(3,4-Ethylenedioxythiophene) Composite Nanotubes for Supercapacitors. *Phys. Chem. Chem. Phys.* **2010**, *12* (17), 4309–4316.

- (134) Chen, X.; Zhu, H.; Chen, Y. C.; Shang, Y.; Cao, A.; Hu, L.; Rubloff, G. W. MWCNT/V₂O₅ Core/shell Sponge for High Areal Capacity and Power Density Li-Ion Cathodes. *ACS Nano* **2012**, *6* (9), 7948–7955.
- (135) Ono, S. Lattice Images of Crystalline Anodic Alumina Formed on a Ridged Aluminum Substrate. *J. Electrochem. Soc.* **1992**, *139* (9), L80–L81.